

From Dutch Short-Lived to Antarctic Long-Lived Stable Boundary Layers

van der Linden, Steven

DOI

[10.4233/uuid:02eef221-2d22-4492-babd-8f8d3f782f8b](https://doi.org/10.4233/uuid:02eef221-2d22-4492-babd-8f8d3f782f8b)

Publication date

2020

Document Version

Final published version

Citation (APA)

van der Linden, S. (2020). *From Dutch Short-Lived to Antarctic Long-Lived Stable Boundary Layers*. [Dissertation (TU Delft), Delft University of Technology]. <https://doi.org/10.4233/uuid:02eef221-2d22-4492-babd-8f8d3f782f8b>

Important note

To cite this publication, please use the final published version (if applicable). Please check the document version above.

Copyright

Other than for strictly personal use, it is not permitted to download, forward or distribute the text or part of it, without the consent of the author(s) and/or copyright holder(s), unless the work is under an open content license such as Creative Commons.

Takedown policy

Please contact us and provide details if you believe this document breaches copyrights. We will remove access to the work immediately and investigate your claim.

From Dutch Short-Lived to Antarctic Long-Lived Stable Boundary Layers

Steven van der Linden

From Dutch Short-Lived to Antarctic Long-Lived Stable Boundary Layers

PROEFSCHRIFT

ter verkrijging van de graad van doctor
aan de Technische Universiteit Delft,
op gezag van de Rector Magnificus prof. dr. ir. T.H.J.J. van der Hagen,
voorzitter van het College voor Promoties,
in het openbaar te verdedigen op
donderdag 5 maart 2020 om 15:00 uur

door

Steven Johannes Antonius VAN DER LINDEN

natuurkundig ingenieur,
Technische Universiteit Eindhoven, Nederland
geboren te Waalwijk, Nederland

Dit proefschrift is goedgekeurd door de promotoren en de copromotor.

Samenstelling promotiecommissie:

Rector Magnificus	voorzitter
prof. dr. ir. B.J.H. van de Wiel	Technische Universiteit Delft, promotor
prof. dr. ir. H.W.J. Russchenberg	Technische Universiteit Delft, promotor
dr. ir. P. Baas	Technische Universiteit Delft, copromotor

onafhankelijke leden:

prof. dr. A.P. Siebesma	Technische Universiteit Delft
prof. dr. A.A.M. Holtslag	Wageningen University and Research
prof. dr. Dipl.-Geoökol. C.K. Thomas	Universiteit van Bayreuth, Duitsland
dr. ir. J.A.E. ten Veldhuis	Technische Universiteit Delft
prof. dr. H.J.J. Jonker	Technische Universiteit Delft, reservelid

Dit onderzoek is financieel mogelijk gemaakt door de European Research Council (ERC) door middel van een *Consolidator Grant* (nummer 648666). Dit werk is mede mogelijk gemaakt door subsidie van de Nederlandse Organisatie voor Wetenschappelijk Onderzoek Exacte en Natuurwetenschappen (NWO-ENW) voor het gebruik van de nationale computersystemen bij SURF (project 16703).

Trefwoorden / *keywords*: Antarctica, Cabauw, intermittency, large-eddy simulations, large-scale pressure gradient, stable boundary layers

Op de omslag / *on the cover*: Visualisatie van een Kelvin-Helmholtz instabiliteit (hoofdstuk 4) door middel van de gesimuleerde temperatuur. De kleurschaal is zodanig gekozen om de overgang tussen de turbulente laag en de niet-turbulente laag erboven te accentueren. / *Visualization of a Kelvin-Helmholtz instability (chapter 4) by means of the simulated temperature. The color scale is chosen such that the interface between the turbulent layer and non-turbulent layer above is accentuated.*

Gedrukt door / *printed by*: Gildeprint - www.gildeprint.nl

ISBN 978-94-6366-251-2

Dit werk is auteursrechtelijk beschermd © 2020 Steven J.A. van der Linden
Alle rechten voorbehouden. / *All rights reserved.*

Een elektronische versie van dit proefschrift is beschikbaar via / *An electronic version of this dissertation is available at:*
<https://repository.tudelft.nl>

Contents

Summary	v
Samenvatting	ix
1 Introduction	1
1.1 Weather: the universal conversation starter	1
1.2 The stable boundary layer	2
1.3 Objectives and research questions	5
1.4 Outline	7
2 Observed Dutch short-lived stable boundary layers	9
2.1 Introduction	10
2.2 Observations	12
2.2.1 In situ Cabauw	12
2.2.2 Near-surface pressure gradient	12
2.3 Observational analysis	13
2.3.1 Selection and classification procedure	13
2.3.2 Ensemble geostrophic wind forcing	13
2.4 Results	15
2.4.1 Radiation	15
2.4.2 Turbulent fluxes	17
2.4.3 Thermal gradient	18
2.4.4 Wind and temperature profiles	19
2.4.5 Steady-state fluxes	20
2.5 Discussion	24
2.5.1 A critical wind speed?	24
2.5.2 Model implications	26
2.6 Conclusions	27
2.A Seasonal distribution	28
3 Modeling the Antarctic long-lived stable boundary layer at Dome C	29
3.1 Introduction	30
3.2 Observational results	32
3.2.1 In situ observations	32
3.2.2 Mechanical cycle and regime transition	32

3.2.3	Contrast between weakly stable and very stable conditions . . .	36
3.3	Numerical simulations	38
3.3.1	Formulation and model description	38
3.3.2	Physical model	40
3.3.3	Numerical set-up	41
3.4	Numerical results	44
3.4.1	General characteristics	44
3.4.2	Turbulent fluxes	47
3.4.3	Steady versus quasi-steady?	49
3.4.4	Sensitivity to resolution	51
3.5	Outlook	52
3.6	Summary and conclusions	54
3.A	Calculating the subsidence heating	56
4	Understanding intermittent bursting at Dome C	57
4.1	Introduction	58
4.2	The steady Antarctic boundary layer?	60
4.3	Wave analysis	62
4.3.1	Spectral analysis	62
4.3.2	Linear stability analysis	66
4.4	Mechanism behind the full cycle	69
4.4.1	Flow evolution during the burst	70
4.4.2	Flow evolution after the burst	71
4.5	Discussion	73
4.5.1	Comparison with suggested mechanisms	73
4.5.2	A systematic climatology of bursts?	75
4.6	Conclusions	76
4.A	Description of the LES case	77
4.B	Derivation of the LSA	78
5	Conclusions and perspectives	81
5.1	Conclusions	81
5.2	Perspectives	83
	Bibliography	87
	Dankwoord	95
	Curriculum Vitae	97
	List of Publications	99
	List of Presentations	101

Summary

Stable boundary layers (SBLs) are a common aspect of the earth's atmosphere and are characterized by a stable density stratification in which the temperature increases with height. This typically occurs during the night, resulting in a *short-lived* stable boundary layer, or persistently throughout the polar winter, resulting in a *long-lived* stable boundary layer. Due to their associated cold surface temperatures, stable boundary layers can stimulate the formation of radiation fog or frost near the surface, which may negatively impact human activities and result in large economic losses. However, despite their omnipresence, a comprehensive understanding of their dynamical behavior is still lacking.

The aforementioned stable stratifications are typically formed when the heating of the earth's surface by solar irradiation is absent. Here, 'stable' refers to the fact that the air will resist vertical displacements and turbulent mixing is suppressed. As a result, an active forcing by the wind is needed to maintain turbulent mixing in the stable boundary layer. This is in contrast to the (daytime) convective boundary layer in which the near-surface air is heated and buoyant mixing occurs by thermals. However, the local wind and stratification are nonlinearly coupled to each other which makes it difficult to predict the eventual state of the stable boundary layer. This eventual state is typically divided in a weakly stable regime with relatively strong turbulent mixing and a very stable regime with weak turbulent mixing.

The behavior of the clear-sky stable boundary layer in response to the large-scale horizontal pressure gradient (geostrophic wind speed) is investigated as the overarching theme in this dissertation. This pressure gradient is expected to be one of the dominant external parameters governing this behavior. An *external* parameter is one that does not (directly) depend on the boundary layer itself. In contrast, *internal* parameters exist, such as the locally observed wind speed or temperature, that vary over time in response to changing external conditions on a scale of seconds to a few hours. A number of specific research questions are formulated and are addressed throughout chapters 2–4 to improve the understanding of the behavior of stable boundary layers. To answer these, a combination of observational analysis of the 'Dutch' short-lived and the 'Antarctic' long-lived stable boundary layer, and high-resolution large-eddy simulations of the long-lived stable boundary layer are used. The specific research questions addressed in chapters 2 and 3 are: "What is the response of the short-lived stable boundary layer as a function of the pressure gradient?"; "Does this pressure gradient separate the different stable boundary-layer regimes?" (both chapter 2) and "Can the steady states of the long-lived stable boundary layer arising from this

pressure gradient be accurately modeled using large-eddy simulations?” (chapter 3). Finally, a characteristic feature of the long-lived stable boundary layer in which turbulence may be discontinuous or “intermittent” in intensity, is investigated in chapter 4. Here, the question is: “Which mechanism triggers intermittency and why is it periodic?”

In chapter 2, geostrophic wind speed data, derived from pressure observations, are used in combination with tower measurements to investigate the nocturnal stable boundary layer at Cabauw, the Netherlands. Since the geostrophic wind speed is not directly influenced by local nocturnal stability, it may be regarded as an external forcing parameter of the nocturnal stable boundary layer. This is in contrast to local parameters such as in situ wind speed, the Monin–Obukhov stability parameter (z/L), or the local Richardson number. To characterize the stable boundary layer, ensemble averages of clear-sky nights with similar geostrophic wind speeds are formed. In this manner, the mean dynamical behavior of near-surface turbulent characteristics and composite profiles of wind and temperature are systematically investigated. The classification is found to result in a gradual ordering of the diagnosed variables in terms of the geostrophic wind speed. In an ensemble sense the transition from the weakly stable to very stable boundary layer is more gradual than expected. Interestingly, for very weak geostrophic winds, turbulent activity is found to be negligibly small while the resulting boundary cooling stays finite.

Observations of two typical contrasting weakly stable and very stable boundary layers from the winter at Dome C station, Antarctica, are used as a benchmark for two centimetre-scale-resolution large-eddy simulations in chapter 3. By taking the Antarctic winter, the effects of the diurnal cycle are eliminated, enabling the study of the long-lived steady stable boundary layer. With its homogeneous, flat snow surface, and extreme stabilities, the location is a natural laboratory for studies on the long-lived stable boundary layer. The two simulations differ only in the imposed geostrophic wind speed, which is identified as the main deciding factor for the resulting regime. In general, a good correspondence is found between the observed and simulated profiles of mean wind speed and temperature. Discrepancies in the temperature profiles are likely due to the exclusion of radiative transfer in the current simulations. The extreme stabilities result in a considerable contrast between the stable boundary layer at the Dome C site and that found at typical mid-latitudes. The boundary-layer height is found to range from approximately 50 m to just 5 m in the most extreme case. Remarkably, heating of the boundary layer by subsidence may result in thermal equilibrium of the boundary layer in which the associated heating is balanced by the turbulent cooling towards the surface. Using centimetre-scale resolutions, accurate large-eddy simulations of the extreme stabilities encountered in Antarctica appear to be possible.

Finally, the high-resolution large-eddy simulations of this Antarctic very stable boundary layer reveal a mechanism for systematic and periodic intermittent bursting in chapter 4. Here, a non-bursting state with a boundary-layer height of just 3 m is alternated by a bursting state with a height of approximately 5 m. The bursts result from unstable wave growth triggered by a shear-generated Kelvin–Helmholtz insta-

bility, as confirmed by linear stability analysis. The shear at the top of the boundary layer is built up by two processes. The upper, quasi-laminar layer accelerates due to the combined effect of the pressure force and rotation by the Coriolis force, while the lower layer decelerates by turbulent friction. During the burst, this shear is eroded and the initial cause of the instability is removed. Subsequently, the interfacial shear builds up again, causing the entire sequence to repeat itself with a timescale of approximately 10 min. Despite the clear intermittent bursting, the overall change of the mean wind profile is remarkably small during the cycle. This enables such a fast erosion and recovery of the shear.

The observational analyses and high-resolution simulations described in this dissertation show that the large-scale pressure gradient is a dominant external parameter for both the ‘Dutch’ short-lived and the ‘Antarctic’ long-lived stable boundary layer under clear skies determining its overall structure. However, the results also indicate that other (thermodynamic) processes, such as radiative heat transfer and soil heat transport, become increasingly important for strong stratifications. Future, realistic numerical simulations should therefore aim to include these processes. Additionally, the results of the short-lived stable boundary layer would benefit from the inclusion or detailed study of surface heterogeneity on a local scale (< 1 km). For example, even the relatively flat Cabauw site has small changes in surface cover and elevation that may affect the near-surface structure of the stable boundary layer and result in horizontal variation of the turbulent fluxes. As such, understanding of microscale surface heterogeneity is highly relevant for weather and climate forecasting, and turbulence-resolving simulations. With respect to the long-lived, *intermittent* stable boundary layer, it is both extremely interesting and relevant to construct a climatology of intermittency in a manner similar to the one described in chapter 2 in which nights with comparable external conditions were grouped together. Using such an approach, a comprehensive picture is obtained on the frequency of occurrence of intermittent bursts as a function of external parameters, and on the contribution to the vertical mixing of wind, heat and scalars in the stable boundary layer. This will aid to better understand the near-surface structure of the stable boundary layer in polar climates.

Samenvatting

Stabiele grenslagen zijn gemeengoed in de aardatmosfeer en worden gekenmerkt door een stabiele dichtheidsstratificatie waarbij de temperatuur toeneemt met de hoogte boven het aardoppervlak. Zulke stratificaties vormen zich voornamelijk 's nachts, wanneer opwarming door de zon afwezig is, maar kunnen ook langdurig optreden tijdens de polaire winter. Door de relatief koude omstandigheden, kan stralingsmist ontstaan of kan vorst aan de grond optreden. Beide kunnen van invloed zijn op onze activiteiten als bijvoorbeeld gladheid optreedt of het zicht beperkt wordt. Ook kan nachtvorst leiden tot aanzienlijke vorstschade aan gewassen waarbij de verliezen kunnen oplopen tot in de miljoenen. Hoewel stabiele grenslagen overal om ons heen aanwezig zijn, wordt hun dynamisch gedrag desalniettemin verre van begrepen.

De term 'stabiel' betekent hier dat de lucht zich verzet tegen verticale verplaatsing en turbulente menging wordt onderdrukt. Als gevolg hiervan is een actieve voortstuwing door de wind nodig om deze menging aan de gang te houden. Dit is in tegenstelling tot overdag waarin spontane menging door thermiek plaatsvindt. De lokale wind en stratificatie zijn echter op een niet-lineaire wijze aan elkaar gekoppeld. Dit maakt de voorspelling van de uiteindelijke toestand van de stabiele grenslaag moeilijk. Deze uiteindelijke toestand wordt vaak onderverdeeld in een zwak stabiel type met relatief sterke turbulente menging en een zeer stabiel type met zwakke turbulente menging.

Het overkoepelende thema van dit proefschrift is het gedrag van de onbewolkte stabiele grenslaag als functie van de grootschalige horizontale drukgradiënt, die vaak als geostrofe wind wordt uitgedrukt. Deze drukgradiënt wordt verondersteld een van de dominante externe parameters van de grenslaag te zijn. *Externe* parameters worden niet direct beïnvloed door de grenslaag zelf. Daarentegen bestaan er ook *interne* parameters, zoals de lokaal geobserveerde windsnelheid of temperatuur. Deze veranderen op tijdsschalen van seconden tot enkele uren als gevolg van veranderende externe condities. In de hoofdstukken 2–4 worden een aantal specifieke onderzoeksvragen behandeld om het begrip van het gedrag van de stabiele grenslaag te verbeteren. Deze vragen worden beantwoord door middel van een combinatie van observatieanalyse en zogenoemde 'large-eddy' simulaties. De gebruikte observaties komen van zowel de nachtelijke stabiele grenslaag in Nederland als de langdurige stabiele grenslaag in Antarctica. Deze Antarctische stabiele grenslaag wordt vervolgens gesimuleerd. De bijbehorende onderzoeksvragen die behandeld worden in hoofdstukken 2–3, zijn: "Hoe hangt het karakter van de nachtelijke grenslaag af van

de grootte van de drukgradiënt?"; "Is er sprake van twee duidelijk verschillende types grenslagen voor verschillende groottes van de drukgradiënt?" (beide hoofdstuk 2) en "Kunnen de evenwichtstoestanden van de Antarctische stabiele grenslaag als gevolg van deze drukgradiënt nauwkeurig worden gemodelleerd door large-eddy simulaties?" (hoofdstuk 3). Ten slotte wordt in hoofdstuk 4 een fascinerende eigenschap van deze Antarctische grenslaag behandeld. Het blijkt dat turbulentie in deze grenslaag haar continue karakter verliest en 'intermitterend' wordt. Dat wil zeggen dat periodes van zeer zwakke turbulentie worden afgewisseld met periodes van hevige turbulentie. Hier is de bijbehorende onderzoeksvraag: "Welk mechanisme veroorzaakt dit periodieke fenomeen?"

In hoofdstuk 2 worden waarden van de geostrofe wind, die zijn afgeleid uit drukobservaties, gebruikt in combinatie met lokale observaties om de nachtelijke grenslaag te Cabauw, Nederland, te onderzoeken. Omdat deze geostrofe wind niet direct wordt beïnvloed door de lokale stabiliteit, kan zij worden beschouwd als een externe parameter van de nachtelijke grenslaag. Dit geldt niet voor lokaal gemeten parameters, zoals de plaatselijke windsnelheid, de Monin-Obukhov stabiliteitsparameter (z/L) of het getal van Richardson. Heldere nachten met vergelijkbare geostrofe wind worden samengenomen tot ensemblegemiddeldes om een algemeen beeld te krijgen. Deze methode stelt ons in staat om het gemiddelde dynamische gedrag van de turbulente eigenschappen nabij de grond en de gemiddelde wind- en temperatuurprofielen systematisch te onderzoeken. De gediagnosticeerde variabelen variëren geleidelijk in grootte als functie van de geostrofe wind. Als gevolg is de transitie van het zwak stabiele naar het zeer stabiele type meer geleidelijk dan verwacht. De turbulente activiteit bij zeer lage geostrofe wind blijkt verwaarloosbaar te zijn, terwijl de afkoeling van de grenslaag eindig blijft.

De observaties van de opvallend verschillende zwak stabiele en zeer stabiele grenslaag in Dome C, Antarctica, worden gebruikt als referentie voor twee centimeterschaalresolutie large-eddy simulaties in hoofdstuk 3. De effecten van de dagelijkse gang worden geëlimineerd door het selecteren op basis van de Antarctische winterperiode en maakt het bestuderen van de langdurige stationaire stabiele grenslaag mogelijk. De gekozen meetlocatie vormt een natuurlijk laboratorium voor de studie van dit gedrag mede door haar homogeen en vlak sneeuwoppervlak en haar extreme stabiliteit. De twee opgezette simulaties verschillen slechts in de opgelegde geostrofe wind, die de meest bepalende factor voor het uiteindelijke type grenslaag blijkt te zijn. In het algemeen wordt een goede overeenkomst gevonden tussen de geobserveerde en gemodelleerde wind- en temperatuurprofielen. De afwijkingen in de temperatuurprofielen zijn waarschijnlijk het resultaat van het gebrek aan een atmosferisch stralingsmodel. De extreme stabiliteit leidt tot een significant contrast tussen de stabiele grenslaag in Dome C en die in gematigde breedtegraden. De hoogte van de grenslaag varieert van grofweg 50 m tot slechts 5 m in het meeste extreme geval. De opwarming van de grenslaag door subsidentie leidt opmerkelijk tot een thermisch evenwicht waarin deze opwarming wordt gebalanceerd door turbulente koeling aan het oppervlak. De huidige centimeterschaalresoluties tonen aan dat accurate large-eddy simulaties van deze extreem stabiele Antarctische grenslagen mogelijk zijn.

Ten slotte onthullen de hoge resolutie large-eddy simulaties van deze zeer stabiele grenslaag een mechanisme voor systematische en periodieke uitbarstingen van hevige turbulentie in hoofdstuk 4. In deze simulaties wordt een toestand zonder uitbarsting waarin de grenslaaghoogte slechts 3 m is, afgewisseld door een toestand met uitbarsting waarin de grenslaaghoogte grofweg 5 m is. Deze uitbarstingen van hevige turbulentie zijn het resultaat van de groei van onstabiele golven die worden veroorzaakt door een Kelvin-Helmholtz instabiliteit. Dit wordt bevestigd door toepassing van een lineaire stabiliteitsanalyse. De benodigde windschering aan de top van de grenslaag wordt opgebouwd door twee processen. De bovenste, quasi-laminaire luchtlaag versnelt door een combinatie van de drukgradiënt en de windrotatie ('het Corioliseffect'), terwijl de onderste luchtlaag afremt door de turbulente wrijving. Tijdens een uitbarsting wordt deze windschering op haar beurt weer geërodeerd waarmee de oorspronkelijke oorzaak van de instabiliteit wordt verwijderd. Vervolgens bouwt deze windschering zich weer op door de eerder genoemde processen. Hierdoor herhaalt de gehele cyclus zich met een tijdschaal van ongeveer 10 minuten. De veranderingen in de gemiddelde wind zijn verrassend genoeg vrij klein gedurende deze cyclus ondanks de duidelijk zichtbare uitbarstingen. Dit maakt het juist mogelijk dat de erosie en herstel van de windschering snel plaatsvindt.

Zowel de observatieanalyse als de hoge resolutie simulaties bevestigen dat de grootschalige drukgradiënt een dominante externe parameter is voor het gedrag en de structuur van de onbewolkte, stabiele grenslagen in Nederland en in Antarctica. De resultaten laten echter ook zien dat andere (voornamelijk) thermodynamische processen, zoals de atmosferische straling en warmtetransport door de bodem, belangrijker worden met toenemende stratificatie. Toekomstige, realistische simulaties zouden daarom als doel moeten hebben deze toe te voegen. Het inzicht van de nachtelijke grenslaag zou verder baat hebben bij een uitgebreide studie naar de effecten van oppervlakteheterogeniteit op een lokale schaal (< 1 km). Zelfs de relatief vlakke omgeving rondom Cabauw bijvoorbeeld kent kleine veranderingen in oppervlaktebedekking en topografie die de grenslaagstructuur nabij de grond kunnen beïnvloeden en kunnen leiden tot horizontale variaties in de turbulente flux. Het begrijpen van deze microschaal oppervlakteheterogeniteit is daarom van belang voor weers- en klimaatvoorspellingen en simulaties die turbulentie (deels) expliciet berekenen. Betreffende de Antarctische grenslaag is het zeer interessant en relevant om een klimatologie van turbulente uitbarstingen te maken zoals in hoofdstuk 2 waarin nachten met vergelijkbare externe condities zijn samengenomen. Zodoende kan een allesomvattende beschrijving van zowel de mate van voorkomen van dit fenomeen als zijn aandeel in de verticale menging van wind, warmte en scalaire grootheden gevonden worden. Dit zal bijdragen aan het begrip van de structuur van de stabiele grenslaag nabij het aardoppervlak in het polaire klimaat.

1

Introduction

1.1 Weather: the universal conversation starter

As a Dutch person, it is safe to say that the Dutch like to complain about the weather, and just as often about its forecast: “it’s too cold”, “it’s too warm”, “they predicted rain, but it’s sunny *beach weather*”¹, etc. Usually, it’s best not to take such ‘complaints’ too seriously and to regard it as small talk at the coffee corner. Apart from showing that (discussing) the weather has a social function, it also indicates our fascination with it, which is something we likely share with all cultures. These conversations about the weather are mainly focussed on the daytime, which is unsurprising as most social interactions, economic activities, travels, and leisure activities take place during this period. One may look up towards the sky, observe the cloud patterns and wonder if it will rain (or snow) in the coming hours. *Is it safe to leave home now? Will the trains keep operating according to schedule?*²

However, it would be naive to assume that nighttime weather phenomena are dull, ordinary or otherwise uninteresting just because many of us are sleeping when it is occurring. These phenomena can even impact human activity during the day, in particular during the morning. Under the right conditions, radiation fog or frost form near the surface. Although these offer good opportunities for nice (landscape) photographs (see Fig. 1.1), they can also have severe negative effects. Both can disrupt all modes of transport as a result of reduced visibility, localized ice formation (e.g., slippery roads) or a combination of these. For example, (dense) fog significantly reduces airport runway capacity leading to flight delays or cancellations as a result of safety regulations (Fabbian et al. 2007; Stolaki et al. 2012; Huang and Chen 2016). Furthermore, frost can be detrimental for agriculture resulting in enormous

¹Mind that, they can even ‘see’ something positive (i.e., sunny weather), as being negative (i.e., the prediction was wrong). The underlying feeling here is that you would have planned a trip to the beach or would have dressed in summer clothes, if you would have known.

²This is probably the second favorite subject to complain about in the Netherlands.



Figure 1.1: Shallow fog layer over pastures next to the A2 motorway during the early morning of 1 September 2017 en route to Schiphol airport for the European Meteorological Society Annual Meeting 2017 in Dublin.

economic losses, especially when occurring in spring (Snyder and Paulo de Melo-Abreu 2005; Kistner et al. 2018). Particularly severe frost events during late April 2017 resulted in estimated losses exceeding 80 million EUR in Switzerland alone (Vitasse and Rebetez 2018), with total estimates of losses throughout Europe ranging up to 3.3 billion EUR³.

These weather phenomena are related to the formation of a stably-stratified boundary layer (or simply stable boundary layer; SBL). When formed during the night, such stably-stratified boundary layer is typically called a nocturnal boundary layer (NBL). More precisely, these phenomena become more likely to occur when the stability of the boundary layer (i.e., temperatures increasing with height above the surface) is particularly strong. However, accurately predicting the strength of this stability as a function of external forcings is still challenging, and, therefore, necessitates the study of the SBL among other reasons.

1.2 The stable boundary layer

To understand what the SBL is, it is important to clarify what is meant by the atmospheric boundary layer (ABL) in general. A clear, unambiguous definition of the ABL does not seem to exist, in the sense that no clear demarcation of its spatial and temporal extent, or structure can be given. Monin (1970) defines the ABL as being the result of “the combined action of turbulent friction and Coriolis force” and characterized by “the density stratification of air”, whereas Moene and van Dam (2014) define it as “the layer where the *diurnal* cycle of surface heating affects the flow”. Although the latter definition is quite applicable at, for example, the mid-latitudes, it does not apply to situations in which a diurnal cycle of surface heating is absent; that is, during the Arctic or Antarctic winter months. A simple working definition

³<https://www.munichre.com/topics-online/en/climate-change-and-natural-disasters/climate-change/spring-frost-losses-climate-change-2018.html>. Accessed online: 14 July 2019

of the ABL is the (turbulent) layer that is in contact with the earth's surface and exchanges momentum, heat, water vapor, etc. with that surface through (turbulent) fluxes. This surface-to-air exchange of heat may help to understand why the SBL is different with respect to the ABL, we typically experience during the daytime.

In the presence of a diurnal cycle in solar irradiation⁴, the earth's surface heats up during the daytime and becomes warmer than the near-surface air. This results in a positive flux of heat (i.e., rate of flow of heat per unit area) from the surface to the air, which causes a warming (and associated reduction of density) of the near-surface air. The near-surface air will become lighter than the air aloft (i.e., unstable) and convection will occur (i.e., spontaneous, unstable motion). Even under relatively weak-wind conditions, turbulent mixing is generally expected to be present as the buoyancy force adds turbulent kinetic energy (TKE) to the flow. As a result, momentum, temperature, water vapor and other scalars become well-mixed.

The situation is reversed during the nighttime: solar irradiation is absent and the surface emits more longwave radiation than it receives. In other words, the sum of incoming and outgoing shortwave and longwave radiation (the net radiation) is negative at night. A net radiative cooling of the surface now results causing a change in sign of the heat flux: the turbulent heat flux at the surface becomes negative (i.e., directed to the surface). This may start a few hours before sunset as the solar irradiation already becomes smaller than the net longwave radiative loss at the surface (Mahrt 2014). Additionally, the reversal of the heat flux from positive to negative *on average* even precedes the change of sign of the net radiation in the Netherlands (see chapter 2). The near-surface air cools and its density increases with respect to the density of the air higher up, and a stable density stratification sets in. Here, 'stable' refers to the fact that the relatively 'heavy' air will resist upward displacements and the relatively 'light' air above will resist downward displacements, which is nicely illustrated by the fog 'sticking' to the surface (see Fig. 1.1). In fact, air parcels that are displaced in the vertical (both upward and downward), will experience a net restoring force to their original position. As the stability of the boundary layer now opposes vertical mixing, an active, mechanical driver is needed to maintain mixing: the wind. In fact, it is the gradient in the wind that causes the turbulent mixing.

However, the stratification and *local* wind shear are coupled to each other making the process nonlinear. Through the inhibition of vertical mixing by the stratification, the wind shear is modified. At the same time, the wind shear is one of the key factors that modifies the stratification of the flow through driving turbulent mixing of heat. This coupling extends to the surface itself, where the cooling by the net radiation causes the air to become stratified (at least for the typical mid-latitude SBLs). Depending on the outcome of the competing effects of stratification and wind shear, the SBL is generally subdivided in two regimes: the weakly stable boundary layer (WSBL) and the very stable boundary layer (VSBL) (see Mahrt 2014; and the references therein). The weakly stable regime is characterized by relatively strong turbulent mixing and relatively weak stratification, whereas the very stable regime

⁴Although a diurnal cycle in solar irradiation is not necessary for the formation of the SBL, it simplifies the explanation.

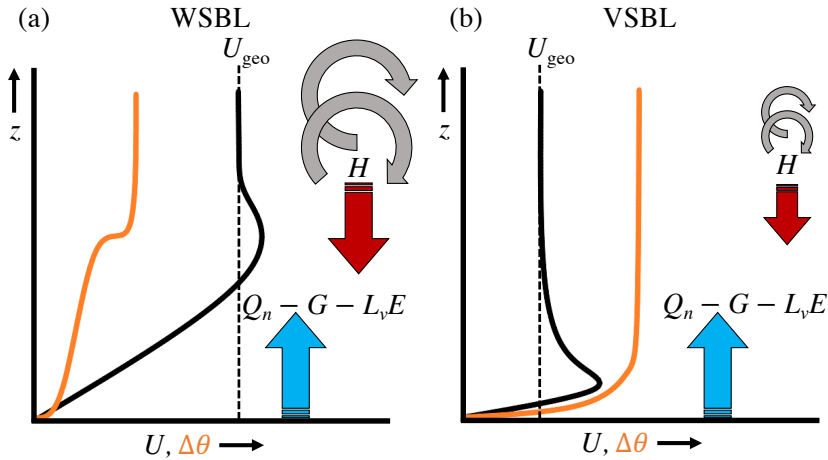


Figure 1.2: Sketch of the typical structure of the wind speed (U , black) and temperature difference ($\Delta\theta$, orange) in (a) the weakly stable boundary layer, and (b) the very stable boundary layer. The geostrophic wind speed is indicated by U_{geo} . In addition, the dominant components of the energy budget at the surface are shown: the net radiative loss Q_n , the soil heat flux G , the latent heat flux $L_v E$ and the turbulent heat flux H .

is characterized by weak turbulent mixing and a relatively strong stratification. The latter regime is sometimes subdivided in a regime of discontinuous, intermittent turbulence and a regime driven mainly by radiative processes and negligible turbulence (van de Wiel et al. 2003). It is precisely in this VSBL that the relative (nocturnal) surface temperatures can become lowest, and the aforementioned formation of radiation fog or frost more likely (see, e.g., Duynkerke 1999). These two prototypical regimes are schematically shown in Fig. 1.2.

Although the basic principles of the SBL are well-understood and can be found in standard textbooks (see, e.g., Stull (1988); Moene and van Dam (2014)), a comprehensive understanding (or ‘unifying’ theory) of the SBL is still lacking (see Fernando and Weil 2010; Mahrt 2014). With increasingly stable stratifications, other processes such as radiative energy transfer (Steenefeld et al. 2010; Edwards et al. 2014; Gentine et al. 2018) and atmosphere-surface coupling (Steenefeld et al. 2006) become (equally) important besides turbulence. For example, the differences in soil conduction and storage of heat may have a profound effect on the near-surface characteristics (cf. Fig. 1.1 in which fog has formed over grass, but not over the relatively warmer road surface). Cloudy conditions may also crucially affect the SBL by enhanced radiative forcing resulting in a WSBL even in weak-wind conditions (Monahan et al. 2015). Other complicating factors that may profoundly affect the boundary-layer behavior are, for example, surface heterogeneity (McCabe and Brown 2007) or wave drag by topography-generated gravity waves (Chimonas and Nappo 1989). Within the weakly-turbulent VSBL, a longstanding challenge is the

understanding of “global intermittency” during which periods of relatively ‘quiescent’, weakly turbulent flow are disturbed by sudden bursts of enhanced turbulence (Mahrt 1999; van de Wiel et al. 2002b). Although multiple causes have been identified, a uniform framework has not been found (Mahrt 1999).

Apart from these fundamental challenges, accurate representation of (very) stable conditions remains challenging in both operational weather models (see, e.g., Viterbo et al. 1999; Sandu et al. 2013; Holtslag et al. 2013) and turbulence-resolving models such as large-eddy simulations (LESs)⁵. Very stable conditions and its associated decrease in the turbulent length scales are challenging for current LES models as the results may become overly reliant on the choice of the subfilter-scale model (Beare et al. 2006; Basu and Porté-Agel 2006) or even lead to laminarization of the flow (Jiménez and Cuxart 2005), especially when using relatively coarse mesh sizes (Zhou and Chow 2011). Direct numerical simulations (DNSs), on the other hand, do not require any parameterization of subfilter motions since they resolve all turbulent motions up to the smallest scales. However, their computational costs currently prevent their widescale use for more realistic boundary-layer flows.

Finally, the existence of a diurnal cycle in the solar irradiation is a favorable but not necessary condition for the formation of the SBL. The main characterizing feature of the SBL is the stable density stratification which corresponds to an increasing temperature with height. Such temperature differences may form when differential cooling exists (viz., the air at the surface is cooled faster than at the top of the boundary layer or the air is warmed at the top). As a result, SBLs can form during the daytime as well, for example, when warm air is advected over a cold water surface (see, e.g., Smedman et al. 1997). This type of SBL is not considered in this dissertation. Another (distinctly) different type of SBL is found in the polar regions during the polar winters. This one is considered in this dissertation. Whereas mid-latitude SBLs are effectively ‘reset’ by convective activity during the day and are, therefore, *short-lived*, the polar atmospheric boundary layer can remain stably stratified throughout the polar winter months as any convective activity is absent. Although these *long-lived* SBLs are persistently stably stratified for months and, therefore, form interesting ‘steady-state’ cases for in-depth study, rapid changes on the timescale of a few hours can nevertheless occur as a result of sudden changes in the large-scale synoptic conditions (see, e.g., Vignon et al. 2017b; Baas et al. 2019). Those aspects are discussed later in this dissertation (see chapter 3).

1.3 Objectives and research questions

The aim of this dissertation is to investigate the behavior of both the short-lived and long-lived SBL in response to the large-scale horizontal pressure gradient, which is expected to be a dominant *external* parameter. This dissertation is restricted to the study of the SBL in clear-sky conditions with little or no cloud cover. Of particular

⁵The large-eddy simulation technique aims to resolve the large turbulent structures (‘eddies’) that contain the majority of the energy, whereas the smallest turbulent structures are parameterized. Therefore, the numerical grid has to be chosen such that these large eddies can be accurately calculated on that grid.

interest are the structure of the SBL resulting from a constant (in time) pressure gradient, the nature of the (quasi-)steady state, and the conditions in which such steady state may be perturbed by intermittency. Insight in these may be gained by progressively ‘zooming in’ on well-defined SBLs. Central in the current approach is the combination of observational analysis and high-resolution large-eddy simulations. Furthermore, implications for future high-resolution turbulence-modelling studies are investigated. Specifically, the following research questions are formulated:

What is the mean dynamical response of the stable boundary layer as a function of the large-scale horizontal pressure gradient? To what extent does this pressure gradient separate the VSBL and the WSBL?

The separation of the SBL in, for example, a very stable and a weakly stable regime, implies the existence of a parameter that unambiguously separates such regimes. However, commonly used parameters, for example, variants of the Richardson number Ri , are not predictors, but merely *internal* parameters as they are the result of the flow dynamics itself. From both a practical and fundamental point of view, *external* parameters are preferred that are not influenced by SBL dynamics itself. Additionally, such external parameters could ideally be an accurate predictor of the regime itself. Although conceptually appealing, identification and application of external parameters is difficult. It is expected that the large-scale horizontal pressure gradient (geostrophic wind speed) is one of such external parameters as it is not directly influenced by the processes in the SBL itself.

Can the observed contrasting states of the long-lived steady SBL encountered, for example, on the Antarctic Plateau, be accurately modelled using a large-eddy simulation approach and does the emergence of those states indeed result from different pressure-gradient forcings?

During the polar winters in the absence of the diurnal cycle, periods in which the SBL is rather constant (‘steady state’) in time (viz., the profiles of mean wind and temperature do not change significantly in time) are alternated by periods in which the SBL changes from weakly to very stable within a few hours. Parts of these rapid regime shifts are governed by variations in the large-scale weather patterns (e.g., pressure gradients). These features make the polar regions ideal ‘natural laboratories’ for the fundamental study of SBL behavior. Since long-term observations are limited in extent, large-eddy simulations (LESs) may offer an attractive alternative method to study the polar SBL. However, the stratification in the polar SBL can become much stronger than typically observed at the mid-latitudes. Here, it is investigated if the observed contrasting WSBL and VSBL (with extreme stability) can be modelled using a carefully designed LES model. Keeping all other parameters constant, it can be investigated if this contrast is predominantly the result of the difference in geostrophic wind speed.

Which mechanism triggers intermittency, and why is it a systematic feature of the long-lived SBL? How does it relate to the steadiness?

Although the long-lived SBL can reach an overall ‘steady state’ lasting multiple days as a result of constant external forcing conditions, a surprising phenomenon may occur on the subhourly timescale. Observations show that successive, near-periodic wave disturbances are frequent in the Antarctic SBL during stationary conditions (Petenko et al. 2019). In turn, these excite so-called ‘intermittent turbulence’, which means that the relatively ‘quiescent’ SBL is disturbed by bursts of enhanced turbulence. By employing one constant geostrophic wind speed, such long-lived steady SBLs can be mimicked with a high-resolution LES approach. Such a numerical representation of the intermittent SBL makes it possible to identify the cause of the flow instability. Furthermore, the process of wave formation and breaking can be studied in detail, which finally allows to explain the full cycle of intermittent turbulence occurring in the overall steady-state polar SBL.

1.4 Outline

The contents presented in this dissertation are based on three journal articles. These form chapters 2–4 of this dissertation. Each of these chapters is self-contained and has a separate introduction section that places its content within the (broader) scope of SBL research. As such, some overlap between these introductions may be present.

Chapter 2 presents an 11-yr climatology of the clear-sky SBL at the Cabauw site in the Netherlands in terms of the large-scale horizontal pressure gradient (geostrophic wind speed). It is investigated how local characteristics, for example, the turbulent heat flux, respond to different values of this specific forcing. In chapter 3, a change of focus is made from the mid-latitude, short-lived SBL to the long-lived steady Antarctic SBL. Two contrasting observed steady states are used to set-up two large-eddy simulations. Here, the structure of the Antarctic SBL is examined and it is explained why a ‘true’ steady state is likely to occur in the polar regions as a result of the overall forcings of the system. One of these simulations is analyzed in further detail in chapter 4, because this case reveals an interesting phenomenon known as intermittency. The responsible mechanism behind this intriguing phenomenon is explained by a combination of linear stability analysis and simulation analysis. Finally, overall conclusions and recommendations for future research are given in chapter 5.

2

Observed Dutch short-lived stable boundary layers

Geostrophic wind speed data, derived from pressure observations, are used in combination with tower measurements to investigate the nocturnal stable boundary layer at Cabauw, the Netherlands. Since the geostrophic wind speed is not directly influenced by local nocturnal stability, it may be regarded as an external forcing parameter of the nocturnal stable boundary layer. This is in contrast to local parameters such as in situ wind speed, the Monin–Obukhov stability parameter (z/L), or the local Richardson number. To characterize the stable boundary layer, ensemble averages of clear-sky nights with similar geostrophic wind speeds are formed. In this manner, the mean dynamical behavior of near-surface turbulent characteristics and composite profiles of wind and temperature are systematically investigated. The classification is found to result in a gradual ordering of the diagnosed variables in terms of the geostrophic wind speed. In an ensemble sense the transition from the weakly stable to very stable boundary layer is more gradual than expected. Interestingly, for very weak geostrophic winds, turbulent activity is found to be negligibly small while the resulting boundary cooling stays finite. Realistic numerical simulations for those cases should therefore have a comprehensive description of other thermodynamic processes such as soil heat conduction and radiative transfer.

This chapter has been published as: **van der Linden, S. J. A**, P. Baas, J. A. van Hooft, I. G. S van Hooijdonk, F. C. Bosveld, and B. J. H van de Wiel, 2017: Local Characteristics of the Nocturnal Boundary Layer in Response to External Pressure Forcing. *Journal of Applied Meteorology and Climatology*, **56** (11), 3035–3047, doi:10.1175/JAMC-D-17-0011.1.

2.1 Introduction

In this paper, a climatology of 11 yr of observations of the nocturnal boundary layer (NBL) is presented in terms of geostrophic wind speed. As we will focus on clear-sky cases only, mechanical forcing is expected to be the major factor determining the evolution of the NBL. For offline numerical studies of the NBL, for example, using single-column models or large-eddy simulations (LESs), the geostrophic wind is often taken as an a priori known *external* parameter that is either available from large-scale numerical weather prediction (NWP) output or specifically chosen.

By contrast, from an observational perspective the NBL is often characterized by relations among *local, internal parameters* such as the local gradient Richardson number Ri or the ratio of observation height to the Obukhov length z/L . By internal, we mean that these parameters are not known a priori but rather are the result of the boundary layer's response to external forcing and local surface characteristics. As probing of the NBL is generally done by measuring vertical profiles of, for example, wind speed and air temperature along a single tower, it is natural to investigate turbulent characteristics in relation to these parameters. These approaches have led to many valuable insights into the structure of the stable boundary layer in response to increasing stability (see, e.g., Mahrt 1998; Grachev et al. 2005; Mauritsen and Svensson 2007; Zilitinkevich et al. 2008; Sorbjan 2010). Recently, attempts have been made to relate boundary layer characteristics directly to the wind speed within the boundary layer (in a dimensional or dimensionless form) (see, e.g., Sun et al. 2012, 2016; Acevedo et al. 2016; van de Wiel et al. 2012a,b; van Hooijdonk et al. 2015; Vignon et al. 2017b). However, such a measured wind speed also has the disadvantage that it is a result of the boundary layer dynamics itself.

The current study aims to merge the internal and external perspectives by connecting the observed local characteristics to the ambient horizontal pressure gradient (expressed as geostrophic wind speed). Because the latter is derived from the synoptic pressure field, it is not directly influenced by the stability and can be considered to be an external parameter. We construct a climatology in order to document the boundary layer response (fluxes and profiles) over a wide range of geostrophic wind speeds for Cabauw, the Netherlands. Using 11 yr of observations (2005–2015), nights are grouped according to their average geostrophic wind speed. Ensemble averages are constructed of these groups. Using such an approach, the mean dynamical response to varying geostrophic wind speed is obtained, while nonsystematic variability is averaged out. To the best of our knowledge, this is the first time that such a classification of boundary layer dynamics in terms of the geostrophic wind speed is presented. Note that our philosophy is inspired by a preliminary study of Bosveld and Beyrich (2004), who classified the NBL at Cabauw with the 200-m wind speed as a proxy for the geostrophic wind speed. Recently, geostrophic wind data from Cabauw were used by Donda et al. (2013) in order to relate near-surface stability to external forcing using a simple Ekman model. Our study differs from Donda et al. (2013) by its focus on climatological interpretation rather than on conceptual modeling.

A detailed climatology will be of special interest to the atmospheric modeling

community, enabling a comparison of different models to the ensemble behavior of the stable boundary layer at Cabauw under realistic conditions. This allows researchers to assess the overall quality of the model representation (parameterizations) for a large stability range. Over the past 10 yr, considerable progress has been reported by the GEWEX Atmospheric Boundary Layer Study (GABLS) consortium (see Holtslag et al. 2013). This international collaboration aims to improve parameterizations of the NBL in weather and climate models (see, e.g., Sandu et al. 2013). Efforts have been effective in pinpointing model capabilities and deficiencies in predicting NBL characteristics such as the near-surface temperature profile, the boundary layer height, and the magnitude of the low-level jet. The intercomparison cases GABLS1 and GABLS2 have been limited to prescribing one constant geostrophic wind speed of 8 m s^{-1} (Cuxart et al. 2006) and 9.5 m s^{-1} (Svensson et al. 2011), respectively. Likewise, GABLS3 and GABLS4 prescribe time-dependent geostrophic winds of approximately 8 m s^{-1} (Bosveld et al. 2014) and $5\text{--}6 \text{ m s}^{-1}$ in magnitude near the surface (E. Bazile 2016, personal communication), respectively. However, to our knowledge a systematic evaluation of model performance for a broad range of geostrophic wind speeds with respect to the observed NBL has yet to be addressed in the literature.

Apart from parameterization issues related to NWP, this climatology could be of interest to idealized model studies using, for example, LESs. Turbulence is largely resolved and different LES model studies show consistent results on average for weakly stable conditions with strong geostrophic winds (see, e.g., Derbyshire 1999; Beare et al. 2006). However, for increasing stability, LESs remain a challenge because of the decrease in the turbulent length scale, and the results become dominated by the sub-grid scheme (Beare et al. 2006; Basu and Porté-Agel 2006). In these conditions, flow laminarization may occur as shown, for example, by Jiménez and Cuxart (2005).

It is well known that cases with very weak turbulence commonly occur in reality under strongly stratified conditions (Poulos et al. 2002; Mahrt and Vickers 2006; Mahrt 2011). Here, we will show that those conditions prevail when the geostrophic wind speeds/pressure gradients are small (as expected). With weak winds, the turbulent heat fluxes may become negligibly small. At the same time, the near-surface thermal gradient remains finite and excessive cooling does not seem to occur. This implies that other thermodynamic processes like radiative and soil heat transport become dominant. Hence, we will argue that for realistic modeling of observed climatologies these processes are equally important as turbulent heat transport.

In section 2.2, a short description of the measurements at Cabauw and the determination of the near-surface pressure gradient (geostrophic wind speed) is given. The observational analysis procedure is described in section 2.3, followed by the main results in section 2.4 and discussion in section 2.5. Section 2.6 describes our conclusions.

2.2 Observations

2.2.1 In situ Cabauw

The observations used in this study were obtained at Cabauw, the Netherlands (51.971°N, 4.927° E). The surrounding terrain has relatively flat topography with surface elevations of less than 1 m, and the area is mainly covered by grassland. A detailed description of the site may be found in van Ulden and Wieringa (1996). Main tower measurements of the wind speed (cup anemometers) and the temperature (KNMI Pt500-elements) are obtained at 40, 80, 140 and 200 m, and stored at 10-min intervals. Wind speed is measured at two booms for each level at approximately 10 m from the center of the tower. The temperature and wind speed measurements at 10 and 20 m are measured at an auxiliary mast. To minimize the effects of flow obstruction, instruments from the undisturbed wind sections are selected per 10-min interval. Additionally, the temperature is measured at 1.5 m. The near-surface fluxes are calculated by applying the eddy-covariance technique to measurements from a 5-m flux tower. All components of the net radiation are determined individually at a height of 1.5 m above the surface. Detailed information on the tower measurements, tower positions and instrumentation may be found in Bosveld (2016).

2.2.2 Near-surface pressure gradient

The near-surface pressure gradient at Cabauw is derived from pressure observations of the national meteorological network in the Netherlands at 10-min intervals up to a distance of 200 km from Cabauw. This pressure gradient can be calculated with high accuracy as a result of the high-quality pressure observations over the Netherlands and the North Sea, and the relatively flat topography of the Netherlands. First, the pressure observations are corrected for height differences; that is, they are transformed to mean sea level values. Second, a two-dimensional quadratic polynomial is fitted to the observations to obtain the pressure field over the Netherlands. From the curved pressure field the near-surface pressure gradient is calculated by taking the gradient at Cabauw. For interpretation purposes, the magnitude of the near-surface pressure gradient is written as the geostrophic wind speed,

$$U_{\text{geo}} = \frac{1}{\rho_0 f} |\nabla P|, \quad (2.1)$$

in which ρ_0 is a reference air density, and $f = 2\Omega \sin \phi$ is the Coriolis frequency calculated, with Ω being the angular velocity of the earth and ϕ the latitude of Cabauw. An accuracy of 0.1 hPa in the pressure observations is assumed, resulting in standard deviations of 0.28 and 0.26 m s^{-1} in the latitudinal and longitudinal components of the geostrophic wind, respectively. Note that this does not imply that the actual wind above the boundary layer is in geostrophic balance. A more detailed description may be found in Bosveld et al. (2014).

2.3 Observational analysis

Following Baas et al. (2012) and van Hooijdonk et al. (2015), we calculate averaged quantities from multinight ensembles. It is expected that by such a procedure the general dynamical behavior of the stable boundary layer will be clarified because variability of individual nights is largely averaged out. This averaged-out variability may include, for example, wave activity, meandering of the flow, and local circulation patterns.

2.3.1 Selection and classification procedure

The observations are partitioned in 24 h starting at 0900 UTC, such that each period contains one full night. Periods during which one or more gaps exceeding 50 min are present are removed from the dataset. Using a similar approach to van Hooijdonk et al. (2015), the time is subsequently shifted to set $t = 0$ h when the net radiation Q_n becomes negative for more than 1 h. The scope of this study is limited to studying the dynamics as a function of varying geostrophic wind speed. Since it is known that clouds may crucially affect the boundary layer dynamics, only clear-sky nights are considered (see, e.g., Bosveld and Beyrich 2004; Donda et al. 2013). A clear-sky filter selects nights based on an averaged net radiation $\overline{Q_n} \leq -30 \text{ W m}^{-2}$ and standard deviation $\sigma(Q_n) \leq 0.5 |\overline{Q_n}|$ between $t = 0$ and 8 h. The aforementioned selection results in a subset of 1969 nights ($\sim 50\%$ of the total of 4016). A more stringent criterion of the standard deviation $\sigma(Q_n) = 15 \text{ W m}^{-2}$ was also tested and resulted in a smaller number of selected nights (1303). This did not significantly affect the results, however; variability was slightly increased for geostrophic wind speeds $U_{\text{geo}} \geq 12 \text{ m s}^{-1}$.

Nights are classified into 1 m s^{-1} geostrophic wind speed bins according to the mean geostrophic wind speed between times $t = -4$ and 8 h. Our analysis is limited to $t < 8$ h to avoid effects of the morning transition for short nights during the summer. Additionally, only nights during which the standard deviation of U_{geo} is $\leq 1.5 \text{ m s}^{-1}$ are considered. Nights with geostrophic wind speeds $> 16 \text{ m s}^{-1}$ are removed because of the small number of nights within these classes ($N < 20$). The resulting total number of nights after these additional steps is 1165. Table 2.1 gives an overview of the selection procedure, and Table 2.2 lists the different classes and the number of nights N within each class. More information about the seasonal distribution of the selected nights may be found in appendix 2.A.

2.3.2 Ensemble geostrophic wind forcing

As mentioned in the previous section, nights are discarded if the standard deviation of the geostrophic wind speed is larger than 1.5 m s^{-1} . This criterion is used to limit the variability in the ensemble-averaged geostrophic wind speed. The value of this criterion results from a trade-off between variability in the ensemble-averaged value of the geostrophic wind speed and the number of nights. Applying a more strict

Table 2.1: Overview of the selection procedure and criteria for the nights.

Selection step	Criterion	No. of nights
1 Jan 2005 – 31 Dec 2015	—	4016
Missing-data filter	Gaps ≥ 50 min in U_{geo} , U , θ , or Q_n	4002
Clear-sky filter	$\overline{Q_n} \leq -30 \text{ W m}^{-2}$ and $\sigma(Q_n) \leq 0.5 \overline{Q_n} $ between $t = 0$ and 8 h	1969
Filter excluding nights with large variability in the geostrophic wind speed	$\sigma(U_{\text{geo}}) \leq 1.5 \text{ m s}^{-1}$	1228
Filter removing bins with too few nights	Bin count ≥ 20	1165

Table 2.2: Overview of the classes and number of nights within each class.

Class [m s^{-1}]	N	Class [m s^{-1}]	N
[1; 2)	40	[9; 10)	103
[2; 3)	67	[10; 11)	83
[3; 4)	83	[11; 12)	56
[4; 5)	112	[12; 13)	54
[5; 6)	109	[13; 14)	50
[6; 7)	115	[14; 15)	33
[7; 8)	117	[15; 16)	28
[8; 9)	115		

criterion (e.g., 1 m s^{-1}) leads to a reduction of data by approximately 25%, which in turn leads to a reduction in the statistics and more scatter in the turbulent fluxes.

The temporal evolution of the ensemble-averaged geostrophic wind speed is shown in Fig. 2.1. The ensemble-averaged value for each class shows variation around the bin center values on the order of 0.5 m s^{-1} . The two lowest classes of geostrophic wind speed show a systematic temporal variation in which a minimum value is reached around $t = 2$ h. This diurnal cycle in the pressure gradient likely occurs because of the land-sea temperature contrast in the Netherlands (Tijm et al. 1999; He et al. 2013). This is most apparent under conditions of weak large-scale pressure gradients. However, under these conditions the dependence of the NBL on the geostrophic wind speed is weakest and the effect on our classification is probably small (cf. Fig. 2.7a).

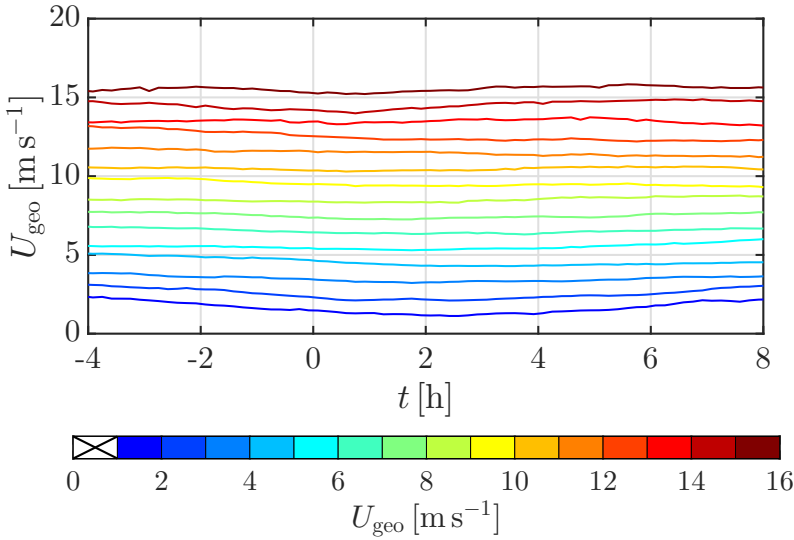


Figure 2.1: Temporal evolution of the ensemble-averaged geostrophic wind speed. The color coding indicates the classes of the geostrophic wind speed and is kept the same in all subsequent figures concerning the different classes.

2.4 Results

In this section, ensemble-averaged quantities such as radiative and turbulent fluxes, along with vertical profiles, are analyzed. The results show that the ensemble averages are remarkably well organised in terms of their corresponding geostrophic forcing. For all classes an approximately stationary state of most quantities is reached at $t = 2$ h.

2.4.1 Radiation

Figures 2.2a,b show the temporal evolution of the net shortwave radiation S_n (downminus upwelling shortwave radiation) and the total net radiation Q_n for the different geostrophic wind speed classes. For all classes, it is observed that on average the total net radiation becomes negative approximately 1.5 h before the incoming shortwave radiation becomes zero, indicating that radiative cooling of the surface starts before sunset. Furthermore, the net shortwave radiation before sunset appears to be inversely correlated with the geostrophic wind speed, which is probably caused by the relatively small number of winter cases having low geostrophic wind speeds (cf. Fig. 2.10).

Prior to $t = 0$ h there appears to be no systematic trend between the net radiation (see Fig. 2.2b) and the magnitude of the geostrophic wind. However, after approximately $t = 2$ h a systematic trend is observed in which the absolute value of the net radiation decreases for decreasing geostrophic wind speed. The

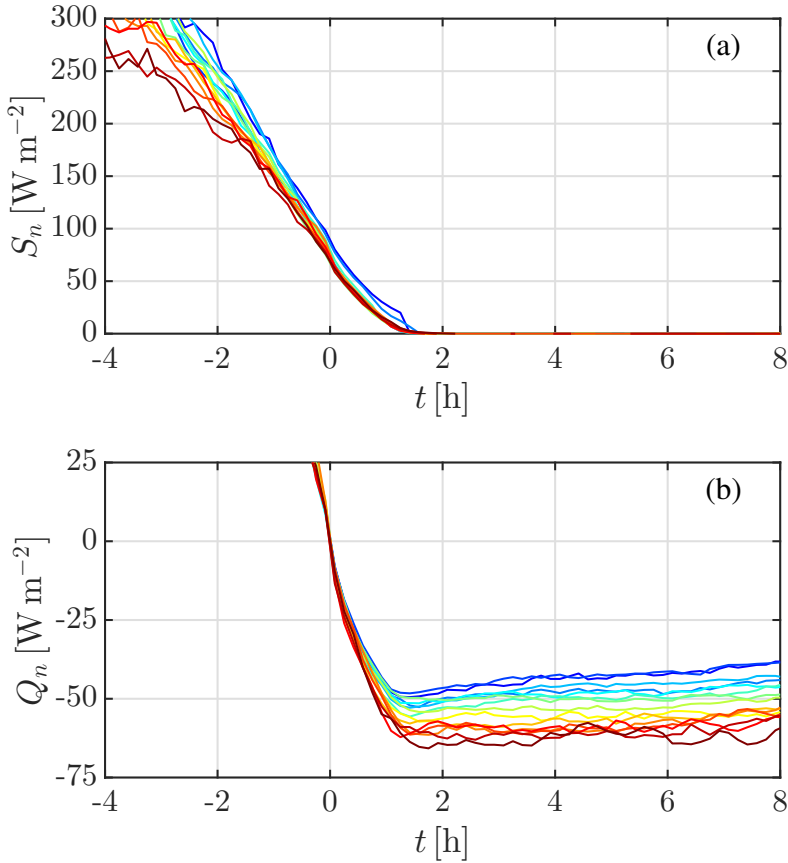


Figure 2.2: Temporal evolution of (a) the net shortwave radiation and (b) the net radiation for all geostrophic wind speed classes. The color coding is given in Fig. 2.1.

net radiation levels off to a value of approximately -60 W m^{-2} for the highest wind class, $U_{\text{geo}} \in [15; 16) \text{ m s}^{-1}$, while the value for the lowest class reaches approximately -50 W m^{-2} between 1 and 2 h, and afterward increases to -40 W m^{-2} at 8 h. These observations are consistent with the expected trend in surface temperature. The stronger thermal gradient in weak wind conditions helps explain the lower net radiative cooling under those conditions; the relatively low surface temperature and outgoing longwave radiation result in a smaller magnitude of net radiative cooling relative to the stronger wind case with relatively high surface temperatures. It is not, however, excluded that the differences among different classes of geostrophic wind speed are influenced by the seasonal distribution of the selected nights (see Fig. 2.10). For example, net radiative loss will be lower in summer as a result of higher moisture content of the lower atmosphere. Further analysis reveals that the difference between summer and winter may amount up to 15 W m^{-2} (not shown).

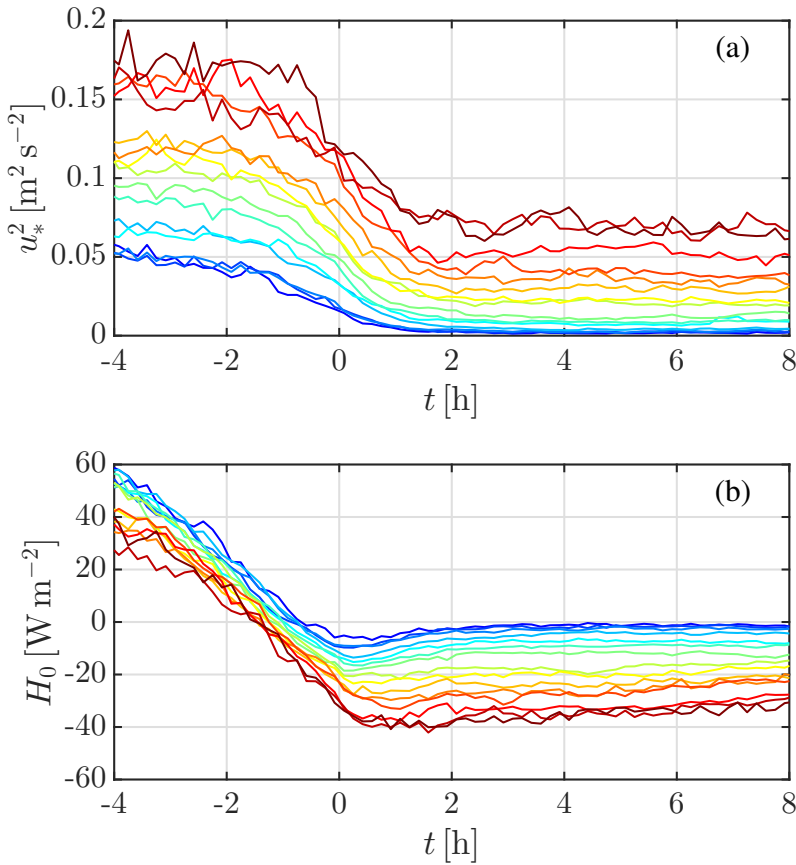


Figure 2.3: As in Fig. 2.2, but for (a) the turbulent stress and (b) the turbulent heat flux.

2.4.2 Turbulent fluxes

The turbulent stress and the turbulent sensible heat flux are shown in Figs. 2.3a and 2.3b, respectively. Both figures show a clear organisation of the data according to classes of constant geostrophic wind speed after $t = 0$ h. For geostrophic wind speeds $U_{\text{geo}} \leq 4 \text{ m s}^{-1}$, both the average turbulent stress and the average turbulent sensible heat flux tend to become negligibly small, suggesting that cases in which turbulent mixing is virtually absent are quite common at Cabauw. This has important implications for numerical modeling of the stable boundary layer. In particular LESs might have difficulties in resolving those small flux cases (see Beare et al. 2006; Holtslag et al. 2013).

The turbulent stress decreases in the late afternoon as a result of the transition toward the stable boundary layer, and tends to level off for $t \geq 2$ h. For the highest wind classes, the stress is reduced to approximately 40% of its pretransition value, while for the lowest wind speed classes it is reduced to approximately 2–3% of its initial value. Contrary to the findings of van Hooijdonk et al. (2015) and Donda et al. (2015), no

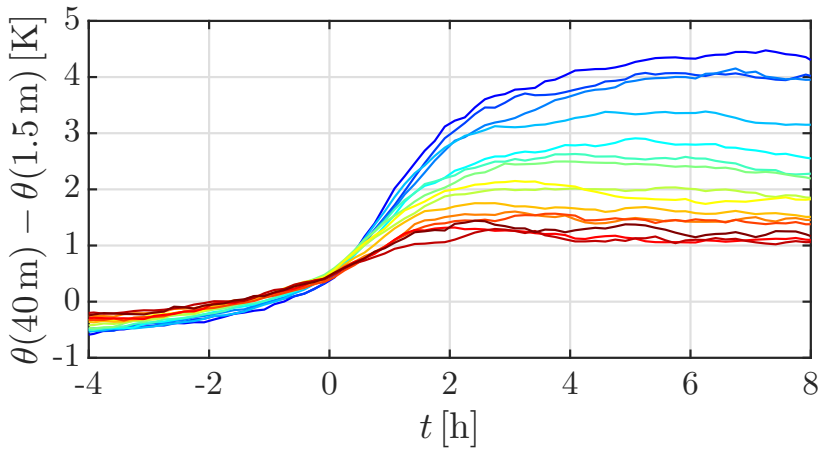


Figure 2.4: Temporal evolution of the thermal gradient between 40 and 1.5 m. The color coding is given in Fig. 2.1.

increase in turbulent stress during the night is found (for the very stable cases). They attributed this increase to a force imbalance between horizontal pressure force and frictional forces after an initial decrease of turbulent friction (see, e.g., Donda et al. 2015).

A similar pattern is observed for the turbulent heat flux (Fig. 2.3b). During the afternoon the heat flux decreases from positive values (i.e., directed from the surface to the atmosphere) and becomes negative between $t = -1.5$ and -0.5 h. This indicates that cooling of the surface layer occurs *before* the change of sign of the net radiation (see section 2.4.3 and the references therein). A slight minimum in the heat flux is present between $t = 0$ and 1 h as the NBL passes a stage of intermediate stability from neutral to more stable later in the night. For $t \geq 2$ h, the turbulent heat flux also tends to an approximately constant value. This quasi-steady value is dependent on the magnitude of the geostrophic wind and is robust when conditioned on different seasons.

2.4.3 Thermal gradient

In Fig. 2.4 the time-dependent gradient of the potential temperature is shown for the different classes. This thermal gradient is defined as the difference in potential temperature between 40 m and 1.5 m. The 1.5-m level is the lowest level present in the 11-yr dataset considered. A temperature probe at 10 cm above surface has been in operation since August 2013, but its dataset is too limited to be used for the current ensemble analysis. Recent results by van de Wiel et al. (2017) employing the limited dataset with the 10-cm probe indicate that the additional difference between 1.5 and 0.1 m may be up to 5 K for low wind speeds.

The thermal gradient prior to the onset of the NBL, $t \leq -1$ h, shows weak dependence on the geostrophic wind, although a tendency toward more neutral strat-

ification is observed for high wind conditions, as expected. Note that, during the daytime, turbulent transport by convection causes the gradient magnitude to remain small ($< 0.7\text{K}$). Similar to the turbulent heat flux, the gradient becomes positive approximately 1 h before the net radiation is zero (cf. Figs. 2.2 and 2.3). This change of sign is followed by a rapid increase of the gradient up to approximately $t = 2$ h.

As shown in Figs. 2.2–2.4, the onset of the stable boundary layer (time at which the turbulent heat flux becomes negative) is not synchronous with either zero short-wave radiation or zero net radiation. This moment is likely dictated by the latent heat flux associated with evapotranspiration. In the afternoon, as the air flows over a relatively wet surface, the continuous demand for energy for evaporation may result in negative sensible heat fluxes in otherwise convective conditions (Moene and van Dam 2014, chapter 7). Unfortunately, no systematic analysis on this interesting aspect could be performed because of observational limitations. For example, the eddy-covariance measurements tend to underestimate the latent heat flux, especially for increasing stability. Furthermore, at low wind speeds dew formation on the instruments results in a large amount of missing values. For a detailed analysis of the latent heat flux in relation to the closure of the surface energy balance, we refer to de Roode et al. (2010).

2.4.4 Wind and temperature profiles

Figures 2.5a–f show the ensemble profiles of the measured wind speed and the relative potential temperature θ_{relative} for three classes of geostrophic wind speeds at times $t = -3, 0, 3$ and 6 h. The latter is defined by subtracting the 200-m potential temperature at $t = 0$ h from all observations, i.e., $\theta_{\text{relative}} = \theta(z) - \theta_0(200\text{ m})$. For all three classes, the wind profiles at 3 and 6 h are nearly identical which indicates that these have reached a quasi-stationary state. This is most prominently observed for the highest geostrophic wind speed class.

In correspondence with van de Wiel et al. (2012a), a “crossing level” (i.e., the height at which the wind speed stays relatively constant) can be identified for the intermediate and highest class. However, this level is not equal for both cases; it is between 40 and 50 m for the $[6; 7)$ class and between 70 and 80 m for the $[14; 15)\text{ m s}^{-1}$ class. Between $t = 0$ h and 3 h the wind accelerates above the crossing level, while it decreases below the crossing level as a result of the increased stress divergence with height resulting from stability (Baas et al. 2012). No crossing level is observed for the lowest geostrophic wind speed class $[1; 2)\text{ m s}^{-1}$. During the afternoon ($t = -3$ h) the magnitude of the wind speed along the entire tower height is approximately twice the value of the geostrophic wind speed during the night. This is probably caused by the geostrophic wind speed being higher in the preceding day (cf. between -4 and -2 hours in Fig. 2.1).

The profiles of potential temperature do not exhibit a stationary state between 3 and 6 h, with cooling along the tower height still occurring, whereas the thermal gradient reaches a roughly stationary value after approximately $t = 3$ h (see Fig. 2.4). The total surface cooling during the night is significant for all classes and may

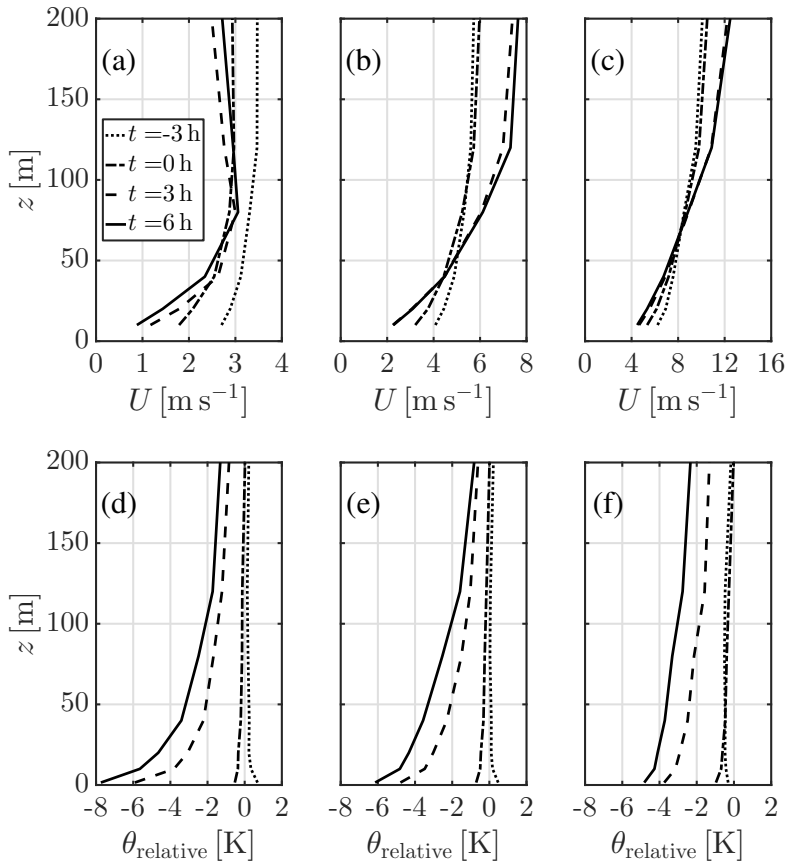


Figure 2.5: Vertical profiles of (top) the wind speed and (bottom) the potential temperature for three geostrophic wind speed classes at four different times: (a,d) [1; 2), (b,e) [6; 7), and (c,f) [14; 15) m s^{-1} . The horizontal scale in the wind speed profiles is not equal for each class.

even reach up to 5 K for the highest geostrophic wind speed shown. By contrast, the relative differences between heights remains small for this geostrophic wind speed. For the lowest geostrophic wind speed class shown, the resulting profile of potential temperature is strongly convex, exhibiting an exponential profile. Such a profile is an indication that the surface layer is decoupled from higher levels (André and Mahrt 1982; Estournel and Guedalia 1985).

2.4.5 Steady-state fluxes

After the initial transition period, the averaged turbulent fluxes do not significantly vary relative to those during the time $t \leq 2$ h (see Fig. 2.3). Therefore we will refer to the period between $t = 3$ and 6 h as the “quasi-steady state” of the stable boundary layer. Note that apart from the turbulent fluxes, Fig. 2.2 indicates that the magnitude of the net radiation itself is decreasing during the night in response to the changing

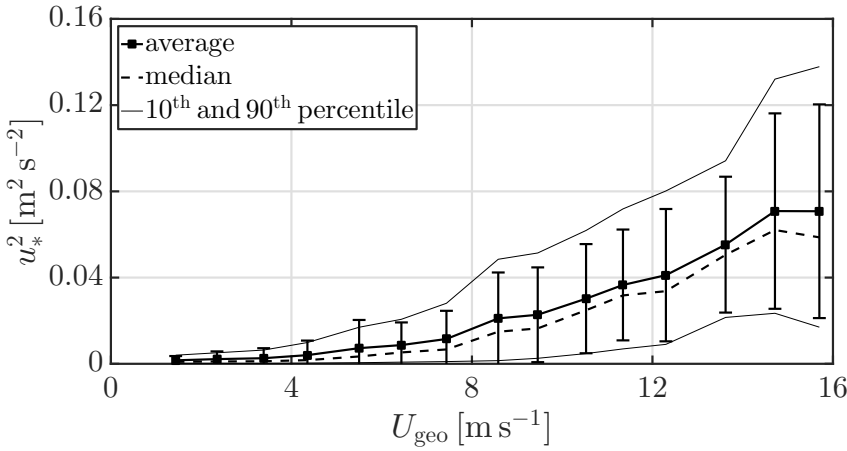


Figure 2.6: Turbulent stress vs geostrophic wind forcing in quasi-steady state. The error bars denote 1 standard deviation from the average value, and the thin lines denote the 10th and 90th percentiles of the data.

vertical profiles of temperature (see Figs. 2.5d–f) and moisture (not shown). The quasi-steady fluxes and their features reported in this section are found to be robust when limiting the data to single seasons. However, a detailed analysis of seasonal effects is beyond the scope of this work.

Figure 2.6 shows the quasi-steady values of the turbulent stress per geostrophic wind speed class. The average and median are calculated from the set of all 10-min interval observations in quasi-steady state per class. For increasing geostrophic wind speed, the average and median values of the turbulent stress increase, as expected. In addition, both the standard deviation and the range of values covered (as depicted through the percentile lines) increase with increasing forcing.

For geostrophic wind speeds $< 4 \text{ m s}^{-1}$, the turbulent stress is on the order of $10^{-3} \text{ m}^2 \text{ s}^{-2}$, and turbulent activity is negligibly small. Such values may typically be found under extremely weak wind conditions (Mahrt and Vickers 2006; Mahrt 2011). The turbulent stress gradually increases for geostrophic wind speeds larger than 4 m s^{-1} . In this ensemble analysis no specific threshold value of the geostrophic wind speed is discerned. By contrast, previous studies report threshold values of wind speeds measured along the tower beyond which the turbulent stress sharply increases in magnitude (see, e.g., van Hooijdonk et al. 2015; Sun et al. 2016). The latter would indicate a clear “on–off” mechanism behind the transition between the very stable (VSBL) and weakly stable boundary layer (WSBL). On the other hand, the “quasi-laminar” VSBL itself can be populated by sudden interruptions of turbulent bursts. This aspect, known as global intermittency, is in fact expected to occur for intermediate ranges of geostrophic wind speed (van de Wiel et al. 2002a; Poulos et al. 2002; Sun et al. 2004; Steeneveld et al. 2006). Recently, Sun et al. (2012) suggested that an intermediate transitional regime exists in which turbulence is intermittent. They hypothesize that this intermittent turbulence is caused by top-down

bursting of turbulent flow from above the boundary layer height. Recently, Anson and Mellado (2014) demonstrated with direct numerical simulation (DNS) that turbulent patches in an otherwise laminar flow may form in a stably stratified Ekman type flow without external triggers. The horizontal extent of these patches were found to be dependent on the stratification. Related results were obtained in DNSs of stably stratified open-channel flow by He and Basu (2015). Interestingly, intermittency has also been simulated over realistic terrain using LESs (Zhou and Chow 2014). Alternating periods of turbulent and laminar parts of the flow may explain this gradual transition from VSBL to WSBL in our averaged quantities.

In Fig. 2.7 the turbulent friction velocity is given as a function of geostrophic wind speed along with the probability density function (PDF) for the classes $U_{\text{geo}} \in [1; 2)$, $[6; 7)$, $[8; 9)$, and $[14; 15) \text{ m s}^{-1}$. The probability density function is determined using an automated kernel density estimation (see Botev et al. 2010). The scatter in observed friction velocities is found to increase for increasing geostrophic wind. Both the average and median values follow a systematic trend. The PDFs show that observed friction velocities within classes overlap with those of other classes. For the highest geostrophic wind speed class (in red) the tails extend as far as $u_* \approx 0.05$ and 0.5 m s^{-1} . The width of the PDF is mainly influenced by the averaging time of the flux sensor of 10 min and by the integral time scale of turbulence (Wyngaard 1973). It is expected that the current averaging time is sufficient to capture most of the significant frequencies in stable conditions (Onley et al. 1996; Babić et al. 2012). However, it is not excluded that low-frequency contributions to the signal are present, and that an increase in averaging time may reduce the observed spread in friction velocities. Note that this aspect is, however, not trivial. Apart from statistical convergence, the variability in u_* may potentially also increase as a result of the inclusion of additional low-frequency motions. Another possible cause could be short disturbances on the 10-min time scale, such as short changes in local cloud cover.

Additionally, the distribution itself is found to change from nearly Gaussian for the highest geostrophic wind speeds to a strongly skewed distribution approaching a lognormal distribution for the lowest class $U_{\text{geo}} \in [1; 2) \text{ m s}^{-1}$. This change in distribution is expected as the friction velocity is nonnegative. For these low geostrophic wind speeds, the width of the distribution is smaller compared to the higher geostrophic wind speeds; that is, the distribution covers only a small range of u_* values. Within this context, Van de Wiel et al. (2017) hypothesized that around critical values of the wind speed the “recovery time” of the NBL to perturbations is large, and as such the (normalized) observational scatter peaks at such wind speeds. Although the spread normalized by the average friction velocity shows a clear decreasing trend for $U_{\text{geo}} \geq 8 \text{ m s}^{-1}$, for low geostrophic wind speeds the spread is rather constant (with a small maximum around 4.5 m s^{-1}). Therefore, at this stage no conclusions on this interesting aspect can be made.

Interestingly, for intermediate geostrophic wind speeds the distributions appear to be bimodal (green and light blue PDFs). The first mode (lowest value of u_*) coincides with the peak of the lowest class (dark blue), whereas the second mode resembles the higher geostrophic wind speed classes. Therefore, for the intermediate

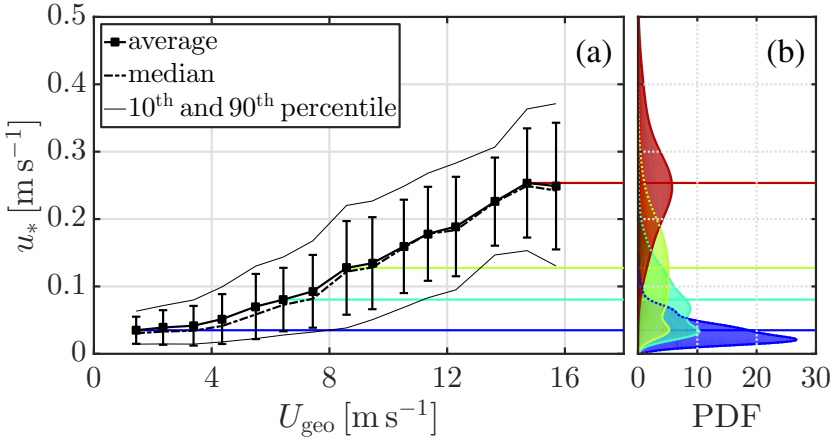


Figure 2.7: (a) Turbulent friction velocity vs geostrophic wind forcing in quasi-steady state. The error bars denote 1 standard deviation from the average value, and the thin lines denote the 10th and 90th percentiles of the data. (b) PDF of the observed friction velocities within the timeframe 3–6 h for four classes. The colored horizontal lines indicate the position of the average values in the PDF. The color coding is given in Fig 2.1.

range of geostrophic wind speeds the boundary layer exhibits characteristics of both the traditional very stable and weakly stable boundary layer. A similar result was recently obtained by Monahan et al. (2015), who found that two separate underlying distributions can be identified in the intermediate local stability range using a hidden-Markov-model analysis. These were found to correlate with geostrophic wind speed and cloud cover (viz., one distribution is more common at low geostrophic wind speed and clear-sky conditions). Likewise, Acevedo et al. (2016) and Dias-Júnior et al. (2017) showed that observations over a wide range of stability fall into two separate distributions associated with the two regimes. As a result, the total distribution is bimodal.

Apart from other physical reasons, a potential explanation for the occurrence of multimodal distributions in the friction velocity is the aforementioned process of global intermittency. During such an intermittent night, the boundary layer would be subject to periods of turbulent bursts in an otherwise quasi-laminar flow. A second explanation is the possibility of local disturbances such as sudden changes in cloud cover, local momentum advection, or small synoptic disturbances. A sensitivity analysis was performed to assess the impact of the net radiation (possible short episodes with clouds) on the observed distribution of friction velocity, but no relation could be detected in the current results (not shown).

The quasi-steady values of the turbulent heat flux are shown in Fig. 2.8. In agreement with the turbulent stress the turbulent heat flux shows a gradual transition in magnitude from low to high geostrophic wind speeds. As compared with the heat loss due to net radiation (see Fig. 2.2b), the supply of heat by turbulent motions is negligible for geostrophic wind speeds of $U_{\text{geo}} \leq 4 \text{ m s}^{-1}$ (viz., $|H_0| \approx 1\text{--}4 \text{ W m}^{-2}$ vs

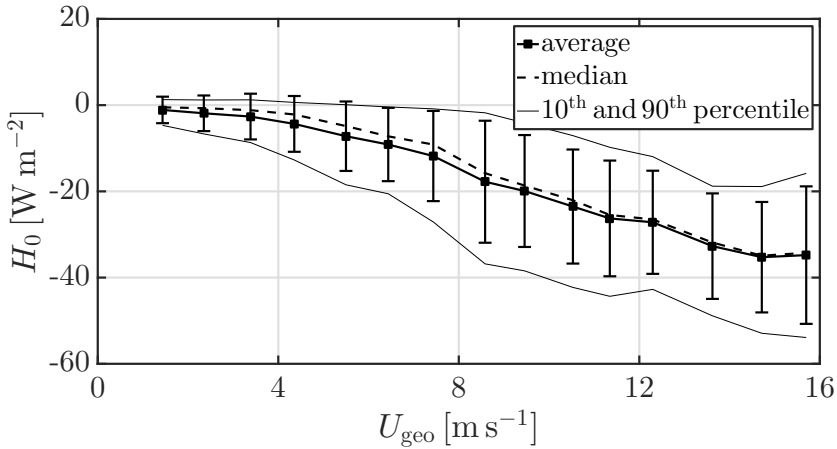


Figure 2.8: As in Fig. 2.6, but for turbulent heat flux.

$|Q_n| = 40 \text{ W m}^{-2}$). For these cases, the evolution of the surface temperature is not dramatically different (in order of magnitude) than that of, for example, cases with medium geostrophic wind (cf. Fig. 2.5d–f). This implies that all thermodynamic transport has to be supplied by the longwave radiation and the surface heat conduction. By contrast, for the highest geostrophic wind speeds the magnitude of the turbulent heat flux is significant at approximately 30 W m^{-2} .

In Fig. 2.9 the (quasi-steady) thermal gradient between 40 and 1.5 m above the surface is plotted as a function of the geostrophic wind speed. It is noted that this gradient does not reach a quasi-steady state for most classes within the timeframe of 3–6 h (also see Fig. 2.4). However, the change within this period is relatively small ($< 0.5 \text{ K}$) with the largest change occurring for the lowest four geostrophic wind speed classes. The difference in gradient strength between the lowest and highest geostrophic wind speeds is found to be a factor of 4 (i.e., approximately 1 vs 4 K for both average and median values). In addition, the spread in observed gradients (see percentile lines) is largest for lower geostrophic wind speeds (i.e., 4 K vs 2 K).

2.5 Discussion

2.5.1 A critical wind speed?

Previous studies using observations from Cabauw (van Hooijdonk et al. 2015; van de Wiel et al. 2017) indicate the existence of a critical in situ wind speed at which the boundary layer as a whole changes from one regime to the other (in an ensemble sense). Similar studies performed at different measurement sites also predict the existence of a threshold wind speed, for example, Dome C, Antarctica (Vignon et al. 2017b); CASES-99 campaign, Kansas (Sun et al. 2012), and Fluxes over Snow Surfaces II (FLOSS II) field campaign, northwest Colorado (Acevedo et al. 2016).

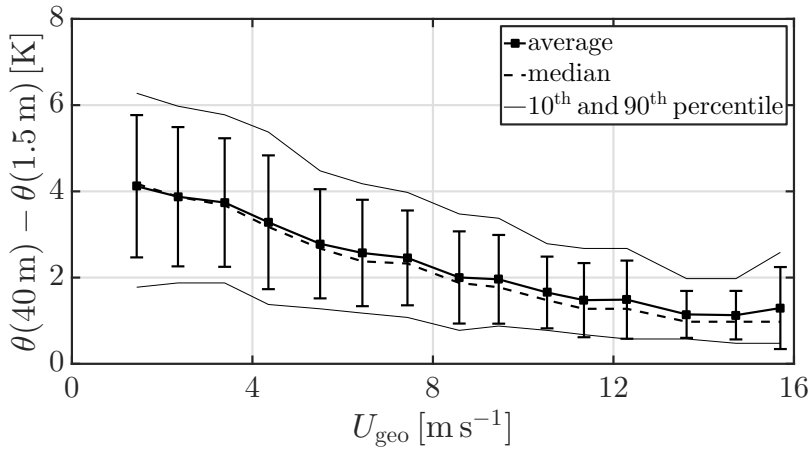


Figure 2.9: As in Fig. 2.6, but for the thermal gradient between 40 and 1.5 m.

In the current results, however, the change in turbulent fluxes and thermal gradient for different geostrophic wind speeds is found to be gradual. No critical geostrophic wind speed or narrow range of geostrophic wind speeds can be identified at which a clear, sudden, or sharp transition occurs between two distinctive regimes of the nocturnal boundary layer.

A similar result was obtained by Monahan et al. (2015), who found two regimes corresponding to a weak turbulence and high turbulence state. The weak turbulence regime was found to correlate with clear skies and low geostrophic wind speeds, while the other regime correlated with cloudy conditions and large geostrophic wind speeds. However, they did not find a clear transition between regimes, and both regimes were found to overlap for a range of geostrophic wind speeds and cloud cover, in agreement with the present study.

In practice, the geostrophic wind speed is not the only external forcing of the system. Atmospheric influences of the NBL include atmospheric moisture, advection of momentum and temperature (which may depend on season or wind direction), and variable cloud cover. External parameters linked to the surface are, for example, local topography and directional dependence of the roughness or the availability of soil moisture, which changes both the heat conductance and the heat capacity of the soil. These parameters can crucially influence the dynamics and regime of the NBL through the production of turbulent mixing, as well as the surface energy budget. Furthermore, a (small) seasonal dependence on the longwave radiative loss directly affects the energy demand.

The influence of these other external parameters on the regime transition are not represented in the geostrophic wind speed. However, they are implicitly observed in the near-surface wind speed, which, as an internal parameter, depends on them via the internal dynamical behavior of the NBL.

If the geostrophic wind speed is the only independent variable (all other parameters are kept fixed), a unique “sharp” transition is expected to occur at a critical value of this wind speed (disregarding aspects of global intermittency). Indeed, such behavior has been shown by both simplified models (McNider et al. 1995; van de Wiel et al. 2002b; Shi et al. 2005; Costa et al. 2011) and well-controlled numerical studies (Nieuwstadt 2005; Donda et al. 2015). On the contrary, if (natural) variability of the other external parameters is included (via Monte Carlo analysis) in the simulations, a smoother pattern would have also occurred. Also, simulations using a more realistic model configuration, for example, with the clear-air radiative transport, presented in McNider et al. (2012), support a more gradual response of the NBL to changing geostrophic wind as in conceptual models.

Furthermore, identification of a critical transition geostrophic wind speed is possibly partly obscured by an intermediate state in which the boundary layer is intermittent. Both fluxes and the local wind speed will vary on a much shorter time scale (i.e., temporarily occupying turbulent and non-turbulent states) than the variation in the forcings such that short-term correspondence is lost (A.H. Monahan 2017, personal communication). Likewise, during intermittent events, wind speeds near the surface (e.g., the 40-m wind speed) will likely react in coherence with turbulence characteristics such as the friction velocity, thereby keeping the relation among these attributes unique.

In summary, whereas internal parameters such as the 40-m wind speed effectively probe the internal state of the system, the geostrophic wind speed does not have knowledge of the realistic variability of other forcings and changing local parameters.

2.5.2 Model implications

The current results show that for low geostrophic wind speeds ($U_{\text{geo}} \leq 4 \text{ m s}^{-1}$) the ensemble-averaged turbulent mixing of both momentum and heat is negligibly small after transition to a quasi-steady stable boundary layer (see Figs. 2.6 and 2.8). For these geostrophic wind speeds, the observed sensible heat fluxes are found to be on the order of $H_0 = 1\text{--}4 \text{ W m}^{-2}$. However, the radiative loss of energy at the surface remains substantial at approximately $|Q_n| = 40 \text{ W m}^{-2}$ (see Fig. 2.2b). At the same time this does not lead to excessive cooling, which implies that other processes, such as radiative heat transfer and heat conduction through soil and vegetation, take over the thermodynamic transport. Large, rapid surface cooling may occur, when the soil heat conduction is inhibited by, for example, snow cover, until natural radiative limits are reached (see Whiteman et al. 2004). This is an important insight with significant implications for advanced models that resolve turbulence such as LESs and DNSs. To accurately represent boundary layers, models need to take into account the heat exchange with an underlying surface (soil and/or vegetation), radiative transfer, and heat transport associated with evapotranspiration. In fact, this requires that a similar degree of complexity be included in the implementation of different processes; for example, soil interaction cannot just be modelled as simple temperature or flux boundary conditions (Steenefeld et al. 2006).

2.6 Conclusions

In the current work, the clear-sky nocturnal boundary layer at Cabauw is investigated using the geostrophic wind speed as a classification parameter. Eleven years' worth of observational data are selected on clear nights and grouped according to the average geostrophic wind speed within a night. Subsequently, ensemble-average time series of, for example, turbulent fluxes and profiles are calculated. This procedure reduces observational variability often found within single nights, and emphasizes the underlying generic dynamics. As such, a benchmark set for numerical models is obtained.

We found that for the geostrophic wind is an important parameter describing the evolution of the nocturnal boundary layer and results in a gradual ordering of the diagnosed variables. For Cabauw, the transition from the weakly stable to the very stable boundary layer is not abrupt for decreasing geostrophic forcing, but gradual in nature for ensemble-averaged diagnostic variables. This is in contrast to the sharp transition found when turbulent fluxes are related to (instantaneous) tower wind speed, and as predicted in conceptual models. For intermediate geostrophic wind speeds, the observed distributions of the turbulent friction velocity appear to be bimodal, whereas in both the weakly and very stable limit the distributions are unimodal.

As the geostrophic wind speed is not the only external parameter, the regime separation is obscured by, for example, soil and atmospheric moisture, advection, and variable cloud cover. Apart from these parameters, we suggest that this behavior can also potentially be explained by the occurrence of globally intermittent turbulence in which sudden moments of turbulent bursts appear in a quasi-laminar boundary layer. Further research is needed to investigate this hypothesis. High-resolution, turbulence-resolving simulations, such as LESs and DNSs, are expected to provide valuable insights with respect to the regime transition and global intermittency. However, any realistic simulation under weak turbulent conditions for the boundary layer evolution at Cabauw would have to include realistic heat transport by radiation, soil, and evapotranspiration.

Finally, more research is needed into the applicability of the current results to other climates. Van de Wiel et al. (2017) showed that the near-surface thermal gradient under weak-wind conditions critically depends on the coupling strength of the land to the atmosphere. The current results also indicate that the onset of the NBL depends on evapotranspiration in the afternoon. It would therefore be interesting to apply the current analysis to other regions provided that both long-term local measurements and an accurate estimate of the geostrophic wind (either from pressure observations or model reanalysis) are available.

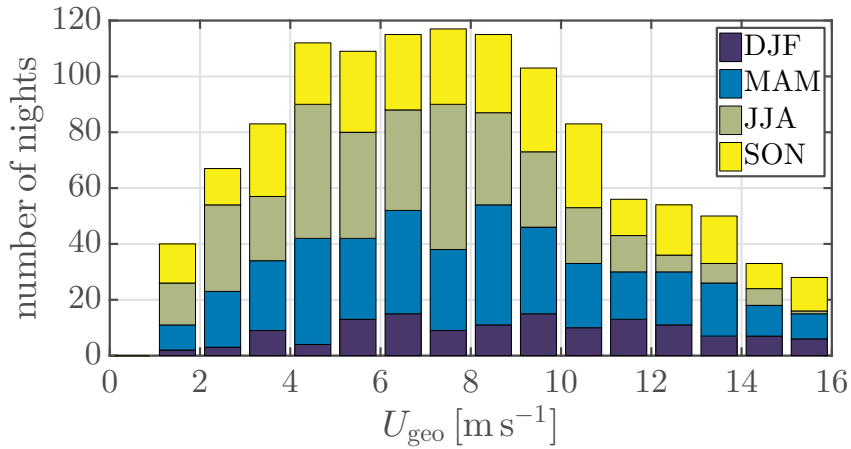


Figure 2.10: Seasonal distribution of all selected nights per geostrophic wind speed class.

2.A Seasonal distribution

In section 2.3.1, the selection and classification procedure is outlined along with the total number of selected nights per class. Here, an overview of the seasonal distribution of these selected nights are given in Fig. 2.10. The relative contribution of the (more cloudy) winter season (December–February) is smallest for all classes as a result of the clear-sky and geostrophic wind speed filters.

3

Modeling the Antarctic long-lived stable boundary layer at Dome C

Observations of two typical contrasting weakly stable and very stable boundary layers from the winter at Dome C station, Antarctica, are used as a benchmark for two centimetre-scale-resolution large-eddy simulations. By taking the Antarctic winter, the effects of the diurnal cycle are eliminated, enabling the study of the long-lived steady stable boundary layer. With its homogeneous, flat snow surface, and extreme stabilities, the location is a natural laboratory for studies on the long-lived stable boundary layer. The two simulations differ only in the imposed geostrophic wind speed, which is identified as the main deciding factor for the resulting regime. In general, a good correspondence is found between the observed and simulated profiles of mean wind speed and temperature. Discrepancies in the temperature profiles are likely due to the exclusion of radiative transfer in the current simulations. The extreme stabilities result in a considerable contrast between the stable boundary layer at the Dome C site and that found at typical mid-latitudes. The boundary-layer height is found to range from approximately 50 m to just 5 m in the most extreme case. Remarkably, heating of the boundary layer by subsidence may result in thermal equilibrium of the boundary layer in which the associated heating is balanced by the turbulent cooling towards the surface. Using centimetre-scale resolutions, accurate large-eddy simulations of the extreme stabilities encountered in Antarctica appear to be possible. However, future simulations should aim to include radiative transfer and sub-surface heat transport to increase the degree of realism of these types of simulations.

This chapter has been published as: **van der Linden, S. J. A.**, J. M. Edwards, C. C. van Heerwaarden, E. Vignon, C. Genthon, I. Petenko, P. Baas, H. J. J. Jonker, and B. J. H van de Wiel, 2019: Large-Eddy Simulations of the Steady Wintertime Antarctic Boundary Layer. *Boundary-Layer Meteorology*, **173** (2), 165–192, doi:10.1007/s10546-019-00461-4.

3.1 Introduction

Two high-resolution large-eddy simulations (LES) are performed of a typical weakly stable boundary layer (WSBL) and a very stable boundary layer (VSBL) as observed at the Dome C station on the Antarctic Plateau in wintertime during a continuous 41-h period in 2015. We assess whether a state-of-the-art LES model is capable of modelling the extreme stability encountered in Antarctica, and investigate both similarities and differences with respect to the common stable boundary layer (SBL) encountered at mid-latitudes. We show that the wintertime Antarctic SBL is an attractive alternative case for idealized theoretical modelling studies aiming to simulate the steady, homogeneous SBL under well-controlled conditions.

Most LES investigations of the SBL rarely attempt a direct comparison with observations, with recent exceptions including the comparisons of LES results with observations of the SBL over the Arctic Ocean (Mirocha and Kosović 2010) and with observations made during intermittently turbulent conditions in the CASES-99 campaign (Zhou and Chow 2014). Another notable exception is the ongoing fourth Global Energy and Water Exchange (GEWEX) Atmospheric Boundary Layer Study (GABLS) based on the Antarctic summertime SBL (Bazile et al. 2014). Such direct comparisons are typically hindered by the fact that most high-resolution LES models are strongly idealized compared with the realistic environmental complexity. In reality, non-stationarity and heterogeneity in the advection forcing, for example, are required to be extensively prescribed in both time and space, such as in the GABLS3 study (Bosveld et al. 2014), making the translation into an idealized LES investigation non-trivial. Additionally, the diurnal cycle itself imposes a challenge on LES models, as day and night intrinsically differ in their characteristic length scales, and thus have largely different resolution requirements. Furthermore, the diurnal cycle prevents the study of long-lived stable boundary-layer behaviour.

Interestingly, alternative simulation cases may be found on the Antarctic continent. First, the diurnal cycle and its associated convective boundary layer are removed by selecting wintertime observations (polar night), which effectively removes the varying resolution requirement between the SBL and convective boundary layer, enabling the comparison of a steady-state flow with a LES model subject to constant forcing. In particular, regional warming by subsidence allows a truly steady state to emerge in contrast to the mid-latitude SBL where only quasi-steady states are found (see section 3.4.3). Second, an especially interesting location is the flat Dome C site in the interior of the Antarctic Plateau with an ‘undisturbed’ fetch of several hundreds of kilometres in all directions. The location is characterized by long periods of cloud-free sky and low total water content (Ricaud et al. 2015). The local snow surface is quite homogeneous and very smooth, often leading to small effective roughness lengths $z_0 \ll 0.01$ m (Vignon et al. 2017a). Furthermore, this location experiences a full range of stabilities ranging from unstable (in summer) to extremely stable during winter with vertical temperature gradients $> 2.5 \text{ K m}^{-1}$ (Genthon et al. 2013).

In recent years, the focus of SBL research has indeed been extended to the Antarctic. Apart from its own relevance in a changing global climate and the difficulty of

accurately predicting the Antarctic weather (King and Connolley 1997; King et al. 2001; Smith and Polvani 2017), the extreme stabilities encountered make it an attractive region for in-depth SBL research (see, e.g., Connolley 1996; Hudson and Brandt 2005; Pietroni et al. 2014; Vignon et al. 2017b).

From the modelling perspective, LES models have become an indispensable simulation tool to study the atmospheric boundary layer, and have been applied with moderate success to the WSBL with large geostrophic wind speeds (Derbyshire 1999; Beare et al. 2006). However, (very) strong stratifications, such as those found in Antarctica, arguably still pose a challenge for the LES technique. Under such conditions, the combination of a decrease in turbulent length scale and relatively coarse mesh sizes may make the results overly reliant on the particular choice of subfilter-scale (SFS) model (Beare et al. 2006; Basu and Porté-Agel 2006) or even lead to flow laminarization (see, e.g., Jiménez and Cuxart 2005).

It is expected that these issues can be partly tackled by increasing the resolution of the numerical grid, apart from using or developing new SFS schemes (see Huang and Bou-Zeid 2013; Matheou and Chung 2014). In recent work, Sullivan et al. (2016) extended the original GABLS1 case (Beare et al. 2006) using a finest mesh resolution of 0.39 m in combination with surface cooling rates of 1 K h^{-1} to increase overall stratification. Although they did not yet reach full convergence, for example, in the height of the low-level jet, these high-resolution cases enabled Sullivan et al. (2016) to identify and analyze coherent structures that lead to characteristic temperature ramps similar to those encountered in outdoor observations (see, e.g., Balsley et al. 2003). These studies, however, still used the (relatively high) original geostrophic wind speed of 8 m s^{-1} of GABLS1, so that the SBL remained in a weakly stable state. In contrast, Zhou and Chow (2011) used larger cooling rates resulting in a temperature contrast of approximately 25 K over 150 m albeit at a higher geostrophic wind speed of 10 m s^{-1} . The aforementioned GABLS4 intercomparison study aims to simulate the VSBL by a combination of high cooling rates and relatively low geostrophic wind speeds of 1.5 K h^{-1} and $5\text{--}6 \text{ m s}^{-1}$, respectively (Bazile et al. 2014).

Here, apart from simulating the observed WSBL, we simulate the VSBL using a geostrophic wind speed of just 3.5 m s^{-1} in combination with a total inversion (vertical temperature difference) of 25 K. In particular, for the selected VSBL, it appears that the boundary-layer height is well below 40 m and, thus, the dominant features of the boundary layer are entirely encompassed by the 45-m meteorological tower of Dome C, enabling the use of a fine-scale resolution ($< 1 \text{ m}$). The ability of our model to simulate the extreme stability encountered in the VSBL is discussed, and discrepancies between simulations and observations identified.

In section 3.2, after a short description of the Dome C site and the measurements, the observed case is described and placed within the framework of the regime transitions. The computational model, the physical model derived from observations, and the numerical set-up are presented in section 3.3. The results are presented and analyzed in section 3.4, followed by an outlook in section 3.5, with summary and conclusions given in section 3.6.

3.2 Observational results

3.2.1 In situ observations

The boundary-layer observations used are obtained at the French–Italian polar station Concordia at Dome C, Antarctica ($75^{\circ}06'S$, $123^{\circ}20'E$, 3233 m above sea level), which is located within a homogeneous snow desert at a distance of approximately 1000 km from the coast. The local topography is flat with a slope $< 0.1\%$ (Genthon et al. 2016), which prevents the local generation of katabatic flows (Aristidi et al. 2005). Furthermore, Vignon et al. (2017a) have shown that the surface is characterized by a typical roughness length $z_0 \ll 0.01$ m for both momentum and heat, although the roughness lengths have a clear dependence on wind direction due to the preferential orientation of sastrugi (small snow ridges).

Wind speed and temperature have been measured at six vertical levels on a 45-m tower situated approximately 1 km west of the main buildings since 2009. Measurements are performed by aerovanes for wind speed, and thermohygrometers for temperature and humidity. The instruments are positioned to face the dominant south-west wind direction (Genthon et al. 2010, 2013). An additional mast of 2.5-m height has been in operation since 2013 to provide more detailed measurements in the lowest few metres above the surface. Note that, due to the harsh conditions in the Antarctic winter, it is impossible to obtain reliable sonic-anemometer measurements of the turbulence. A detailed description of the measurement site, measurements and instrumentation can be found in Genthon et al. (2010, 2013) and Vignon et al. (2017a).

3.2.2 Mechanical cycle and regime transition

The observed ‘steady-state’ WSBL and VSBL are modelled with the LES approach. However, first we discuss why, in the absence of a diurnal cycle, a transition between those states may be due to changing external conditions. As those mechanical cycles are the rule rather than the exception in the Antarctic winter, an in-depth analysis of the climatology is presented, and a canonical case of such a cycle is presented. The ‘steady states’ of this cycle are simulated with the LES technique. Though interesting, the transition itself is not simulated, as it primarily results from changes in the external forcing (see Baas et al. 2019). Here we focus on the boundary layer itself in its steady state.

During the Antarctic winter months (June to August), the boundary layer at the Dome C station is almost continuously stratified and can reach its most stable conditions. Due to the absence of convective activity, the boundary layer may reach moments of ‘steady state’ in which the wind speed and temperature profiles do not significantly change over periods sometimes exceeding a few days. Vignon et al. (2017b) noted that such a steady state can be disturbed by two different processes. The first involves sudden warming events related to a warm and/or moist cloudy airmass advected from the coastal regions into the interior of the Antarctic continent

(see, e.g., Genthon et al. 2010; Vignon et al. 2017b). This process may lead to significant warming of the air near the surface by several 10K within several hours (see, e.g., Argentini et al. 2001; Gallée and Gorodetskaya 2010) and can effectively ‘reset’ the stratification as a whole. Second, regime transitions under clear-sky conditions may be caused by strongly changing boundary-layer flow due to a varying horizontal pressure gradient (Vignon et al. 2017b; Baas et al. 2019). It is this case from which two representative boundary-layer regimes will be considered in more detail.

From the climatology of the site, Baas et al. (2019) identified transitions during the extended Antarctic winters (April to September) of 2011 to 2016 in which the near-surface temperature inversion increased or decreased by more than 15 K, with the near-surface temperature inversion defined as the temperature difference between approximately a height of 10 m and the surface. They applied a threshold on the incoming longwave radiative flux ($LW_{down} < 100 \text{ W m}^{-2}$) to eliminate transitions due to overcast conditions and sudden warming events, yielding a total of 138 transitions due to changes in the mechanical forcing of the boundary-layer flow.

We focus on one of these mechanical transitions starting at 2030 LT (local time = UTC +8 h) on 21 July, and ending at 1330 LT on 23 July 2015. Figure 3.1 shows the temporal evolution of the observed wind speed and air temperature during the selected period. For all measurement heights, the wind speeds decrease during an initial 24-h period. Between $t \approx 24$ h and $t \approx 27$ h, the wind-speed measurements are absent at all levels. Although the aerovanes have a ‘start-up’ threshold of 1 m s^{-1} and an accuracy of 0.3 m s^{-1} (Vignon et al., 2017a), this indicates that flow of any significance is absent in this 3-h time interval. After $t \approx 27$ h, the observed wind speeds at all measurement heights increase.

The observed tendency of the wind speeds is consistent with a decrease and subsequent increase of the near-surface pressure gradient with quiescent periods during which the pressure gradient is nearly absent. During these ‘mechanical cycles’ at the Dome C site, it is expected that the boundary layer adapts to the variation in the near-surface pressure gradient. Indeed, Baas et al. (2019) show, using a single-column model, that during these events the decrease (increase) of local wind speed, for example at 10 m, is correlated with changes in the geostrophic wind speed (a proxy of the pressure gradient). Furthermore, although subject to a diurnal cycle, observations from Cabauw in the Netherlands, show that the strength of the turbulent mixing and the thermal inversion are dependent on this pressure gradient, which acts as an external forcing of the boundary layer as a whole (van der Linden et al. 2017).

During the decrease in wind speed, high-level temperatures increase by more than 10 K, but at lower levels, this increase occurs later: around $t = 17$ h the 2.9-m temperature increases by 9 K over the course of approximately 4 h (cf. Fig. 3.1b). Just prior to the time when all wind speeds are below the measurement threshold, the two lowest levels also experience an increase in temperature. In contrast, the surface cools a total of 8.8 K. The increase in the strength of the inversion is, therefore, caused by two effects: a cooling at the surface, and a larger warming at, for example, the 10-m level. Note that such behaviour differs from typical mid-latitude

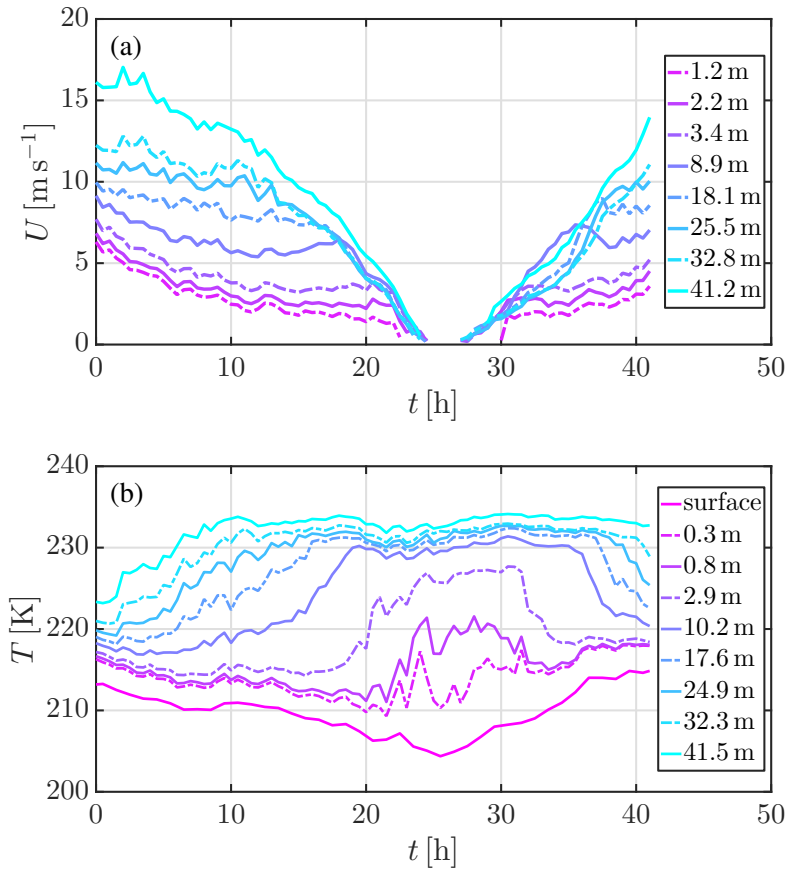


Figure 3.1: Temporal evolution of (a) the wind speeds and (b) temperatures measured at the tower and surface during the selected 41-h period starting 2030 LT on 21 July 2015.

climatologies where the nocturnal inversion primarily develops from below due to surface cooling (van der Linden et al. 2017).

When the wind speeds increase after $t > 27$ h, the general tendencies in temperature are reversed: the surface temperature increases, and the air temperatures decrease. In addition, the timing of the decrease is reversed, with the lowest levels decreasing first and the highest level the latest. No discernible decrease is observed for the 41.5-m level within the plotted time frame.

The temporal relationship between the local wind speed and thermal gradient for the selected period is shown in Fig. 3.2 (phase space-diagram). To demonstrate the representativity of our specific case, the temperature–wind speed relation is embedded in the overall climatology obtained from the Antarctic winter months of 2011–2015. Figure 3.2 shows that the selected mechanical cycle produces a regime transition between the WSBL and VSBL, and vice versa, and indicates a non-monotonic relation between wind speed and thermal gradient. Vignon et al. (2017a) first iden-

tified this dependence, highlighting the appearance of a ‘back-folding’, and stating it resembles a reversed ‘S’ shape. Indeed, the trajectory of the selected period shows this non-monotonicity. Interestingly, Van de Wiel et al. (2017) show, using a conceptual model, that the equilibrium value of the thermal inversion strength can be predicted as a function of the wind speed at a crossing level where the wind speed is relatively constant with time and thereby serves as a proxy for the external geostrophic wind speed. This crossing-level height at the Dome C station was identified to be at approximately 10 m above the surface in summer (Vignon et al. 2017a; van de Wiel et al. 2017).

The trajectory starts (in red) at a high local wind speed ($\approx 10 \text{ m s}^{-1}$) and a relatively low thermal inversion strength ($\approx 5 \text{ K}$), before the 9-m wind speed starts decreasing. At approximately 6 m s^{-1} , the thermal inversion strength rapidly increases after which it levels off. This corresponds to the time frame 10–20 h in Fig. 3.1b during which the temperatures at 10 m and the surface change by approximately +12 K and -4 K , respectively. In addition, whereas the overall tendency of all wind speeds is a decrease prior to $t = 24 \text{ h}$, during this time frame, a small local increase of the wind speed at 9 m is observed, which causes the trajectory to incline ‘backwards’ and exhibit the reversed ‘S’ shape. After the sharp increase, the inversion strength levels off while the wind speed is still decreasing. The slight increase of thermal inversion strengths for $U(9 \text{ m}) < 2 \text{ m s}^{-1}$ is caused by a continuing decrease of the surface temperature.

The characteristic (sharp) increase in the 10-m temperature in this wind-speed interval can be understood as follows: at the boundary-layer top, a continuous competition is present between turbulence acting to elevate (or at least maintain) the height of the thermal inversion, and subsidence pushing it down. For a small decrease of the large-scale pressure gradient, turbulent mixing weakens and the inversion sinks below the 10-m level. As a result, the air temperature at this height increases until a new balance is reached. As a second-order effect, Baas et al. (2019) show, using their single-column model, that at the same time stress divergence at this height is inhibited, i.e., the effective drag exerted by the surface is reduced, resulting in a local acceleration of the flow.

For $t > 27 \text{ h}$, the wind speed increases and the trajectory (in blue) reverses. The overall shape of the blue trajectory is similar to the shape of the red trajectory, i.e., when the wind speed reaches a threshold value, the thermal inversion strength rapidly decreases. By a similar argument, turbulent mixing now strengthens, resulting in an increase in the height of the thermal inversion and effective cooling at 10 m.

It is observed that, for both low and high wind speeds, viz., $U(9 \text{ m}) < 3.5 \text{ m s}^{-1}$ and $U(9 \text{ m}) > 6 \text{ m s}^{-1}$, the two trajectories appear to overlap, suggesting that, in this example, well-defined, robust ‘steady states’ exist that represent the final state of a mechanical cycle. Therefore, our modelling efforts are directed towards the simulation of the ‘end points’. For intermediate wind speeds, the trajectories do not completely overlap. While the observed asymmetry in this region may be a systematic feature of these mechanical cycles (Baas et al. 2019, see their Fig. 4a), no conclusive cause or explanation has been identified to date. Detailed simulations under a wide

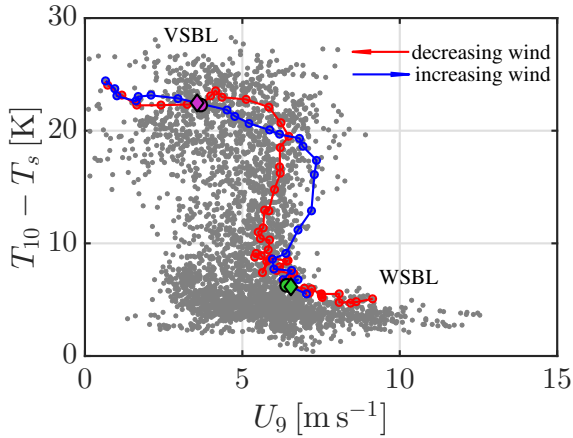


Figure 3.2: Scatter plot of the thermal inversion strength between the height of 10 m and the surface versus the wind speed at 9 m as found in the winter climatology of the Dome C station. The trajectories belonging to our selected cycle (cf. Fig. 3.1) are depicted by the red and blue lines. Each step along the trajectory corresponds to 30 min. The green (purple) circles and diamonds indicate the reference points that are studied in detail through numerical simulations. Circles indicate the WSBL and VSBL from the initial phase of the large-scale wind-speed decrease, and diamonds indicate those taken from the phase of the large-scale wind-speed increase.

range of conditions, for example, the rate of change of geostrophic wind speed or the strength of subsidence, are expected to help clarify these issues in future.

3.2.3 Contrast between weakly stable and very stable conditions

Figure 3.3 shows the representative vertical profiles of wind speed and relative temperature of the WSBL at $t = 5.5$ h and $t = 31.5$ h, and the VSBL at $t = 21.5$ h and $t = 41$ h, with the relative temperature defined as the air temperature minus the surface temperature. These times roughly correspond to those points at which the trajectories of both transitions start (finish) overlapping, and mark the region of rapid regime shift (see the circles and diamonds in Fig. 3.2). Interestingly, the wind-speed and temperature profiles from both the increasing and decreasing large-scale wind-speed phases are remarkably similar in both shape and magnitude (see Fig. 3.3).

The profiles of wind speed indicate a large difference in scale between the VSBL and WSBL at the Dome C station. For the WSBL, the wind speed consistently increases with height, and reaches approximately 14 m s^{-1} at $z \approx 41$ m—it is possible a local wind-speed maximum is present above the observation tower. During summer, low-level jets typically form in the Antarctic SBL between 15 m and 60 m (Gallée et al. 2015) due to the diurnal cycle, but it is unclear if a similar mechanism is present during the long-lived wintertime SBL. As the observation tower is not sufficiently high to capture the entire boundary layer, it is unknown at which height this maximum is present. In addition, it is unknown if the wind speed at the top of the boundary layer

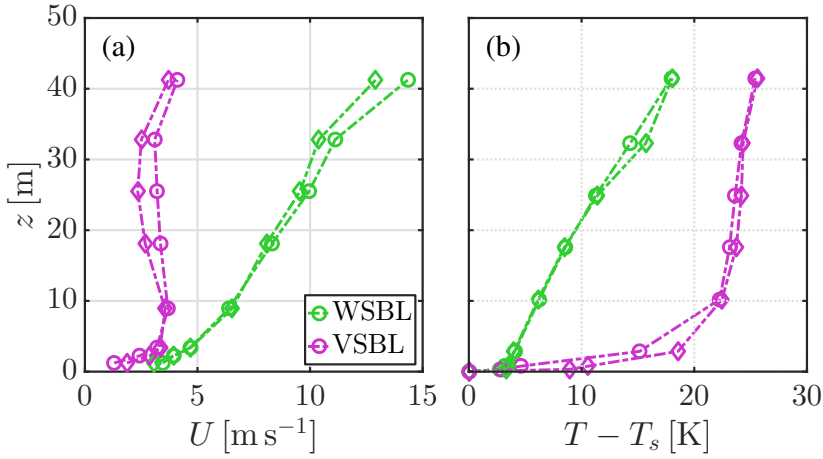


Figure 3.3: Profiles of measured (a) wind speeds and (b) air temperature minus the surface temperature corresponding to the reference points in Fig. 3.2. The very stable and weakly stable regimes are coloured in purple and green, respectively. Circles indicate the WSBL and VSBL from the initial phase of large-scale wind-speed decrease, and diamonds indicate those taken from the phase of large-scale wind-speed increase.

converges to a fixed value, and if so, to which value. In contrast, the height of the observation tower appears to be sufficient to capture the main features of the VSBL, such as the jet-like structure with a local maximum at $z \approx 9$ m. At greater heights (≥ 18 m), the variation in wind speed with height is relatively small and measured wind speeds are $\approx 3.5 \text{ m s}^{-1}$.

The vertical profiles of the relative temperature also indicate a large contrast between the WSBL and VSBL measured during the transition. In the weakly stable regime, the temperature profile is mostly linear with height apart from very close to the surface ($z < 1$ m) where it attains a more convex shape; the change in temperature over the height of the tower is about 18 K. In contrast, the temperature profile in the very stable regime is exponential in shape in which the largest change in temperature occurs in a thin layer close to the surface, i.e., a change of 22 K within 10 m. Moving from 10 m to the top of the tower, the remaining increase of temperature is 3 K. This marked difference in the shape of the temperature profile with a more ‘convex–concave–convex’ profile for the weakly stable regime and exponential (convex) profile for the very stable regime has been reported by van Ulden and Holtslag (1985) for Cabauw, and Vignon et al. (2017a) for the Dome C station, respectively. Note that, in the selected weakly stable regime, the maximum measurement height is probably not sufficient to observe the full ‘convex–concave–convex’ structure. A convex (exponential) temperature profile is indicative of the SBL dominated by radiative transport (Brunt 1934; Cerni and Parish 1984), whereas concave profiles indicate non-linear diffusion by turbulent mixing of heat is dominant (Garratt and Brost 1981; André and Mahrt 1982; Estourel and Guedalia 1985; Derbyshire 1990).

3.3 Numerical simulations

3.3.1 Formulation and model description

The set of equations describing the evolution of the LES model are the filtered equation for conservation of mass, the filtered Navier–Stokes equations under the Boussinesq approximation for the filtered velocity vector \tilde{u}_i , and the filtered equation for energy written in terms of the filtered potential temperature $\tilde{\theta}$

$$\frac{\partial \tilde{u}_j}{\partial x_j} = 0, \quad (3.1a)$$

$$\frac{\partial \tilde{u}_i}{\partial t} + \frac{\partial \tilde{u}_j \tilde{u}_i}{\partial x_j} = -\frac{\partial \tilde{\pi}}{\partial x_i} - \frac{\partial \tau_{ij}}{\partial x_j} + \frac{g}{\theta_0} (\tilde{\theta} - \theta_0) \delta_{i3} + f_C \epsilon_{ij3} (\tilde{u}_j - G \delta_{j1}), \quad (3.1b)$$

$$\frac{\partial \tilde{\theta}}{\partial t} + \frac{\partial \tilde{u}_j \tilde{\theta}}{\partial x_j} = -\frac{\partial R_{\theta,j}}{\partial x_j} - w_s(x_3) \frac{\partial \langle \tilde{\theta} \rangle}{\partial x_3}, \quad (3.1c)$$

where the tensors τ_{ij} and $R_{\theta,j}$ represent the SFS fluxes of momentum and temperature, $\tilde{\pi}$ is the modified pressure, and $w_s(x_3)$ the vertical profile of the subsidence velocity, with x_3 representing the vertical coordinate. The angled brackets indicate domain averaging in the horizontal directions. Furthermore, the Coriolis parameter is denoted by f_C and the geostrophic wind speed by G . The velocity boundary conditions are no-slip ($\tilde{u} = \tilde{v} = 0$) and no-penetration $\tilde{w} = 0$ at the bottom, and stress-free $\partial \tilde{u} / \partial z = \partial \tilde{v} / \partial z = 0$ and no-penetration $\tilde{w} = 0$ at the top. A fixed temperature is prescribed both at the bottom and top (Dirichlet condition). In the lateral directions, periodic boundary conditions are employed for both the velocity and temperature. For simplicity, the tilde indicating the filtering is dropped in the remainder of the text.

The SFS flux tensors, which are the result of spatial filtering of the conservation equations for momentum and temperature, account for the unresolved momentum and temperature fluxes. As both tensors contain the filtered product of the unfiltered quantities, a closure relation (or parametrization) is required to relate the SFS fluxes to the resolved quantities. The numerous closures reported in the literature vary greatly in formulation and complexity (see, e.g., Deardorff 1980; Sullivan et al. 1994; Bou-Zeid et al. 2005; Basu and Porté-Agel 2006; Zhou and Chow 2011; Chung and Matheou 2014; Abkar and Moin 2017). Here, we use a simple Smagorinsky–Lilly-type eddy-viscosity model (Lilly 1962; Smagorinsky 1963), which includes stratification effects by retaining the buoyancy flux in the SFS turbulent-kinetic-energy equation (Lilly 1962; Mason 1989) assuming local equilibrium, and thereby neglecting the tendency, advection and turbulent transport terms. In this model, which is adopted due to its ease of implementation and low computational costs, the eddy viscosity is given by

$$K_m = \lambda^2 S \left(1 - \frac{g}{\theta_0} \frac{\partial \theta}{\partial z} \right)^{\frac{1}{2}}, \quad (3.2)$$

where λ is a mixing length, $S = (2S_{ij}S_{ij})^{\frac{1}{2}}$ is the magnitude of the strain tensor, g is the acceleration due to gravity, θ_0 is a reference temperature, and Pr_t is the turbulent Prandtl number. For the mixing length, we use the wall-correction formulation of Mason and Thomson (1992) to match the local wall scale $\kappa(z+z_{0,m})$ and the subfilter length scale $\Delta \equiv (\Delta x \Delta y \Delta z)^{1/3}$ according to

$$\frac{1}{\lambda^n} = \frac{1}{(c_s \Delta)^n} + \frac{1}{(\kappa(z+z_{0,m}))^n}, \quad (3.3)$$

where c_s is the Smagorinsky constant and $n = 2$.

Apart from the von Kármán constant κ , the adoption of this scheme requires specification of two parameters: the turbulent Prandtl number Pr_t and the Smagorinsky constant c_s . Field observations suggest that $\text{Pr}_t \gtrsim 1$ for stable stratification (Ohya 2001; Zilitinkevich et al. 2007, 2008), whereas the Smagorinsky constant c_s is smaller than (or at least equal to) its isotropic turbulence value (Kleissl et al. 2003; Bou-Zeid et al. 2010). Also, too high a value of the Smagorinsky constant may lead to excessive mixing compared with empirical data (de Roode et al. 2017). Therefore, these parameters are set to $\text{Pr}_t = 1$ and $c_s = 0.12$, where the latter is based on the expected range of stability (from our observations). Additionally, De Roode et al. (2017) show that the use of anisotropic grids may lead to excessive diffusion for very stable stratification. Furthermore, to limit over-reliance on the particular choice of SFS scheme and possible excessive diffusion, we employ isotropic grids of very high resolution ($\Delta = 0.08, 0.125$ and 0.7 m).

At the bottom boundary, rough-wall boundary conditions are used to calculate the surface fluxes using Monin–Obukhov similarity theory (MOST). In stable conditions, the similarity functions of Högström (1988) are used.

Heating of the air due to subsidence is implemented by the last term in the filtered equation for conservation of energy in which the largest gradients are expected (see Eq. 3.1c). Subsidence of momentum is not included in the current LES cases. For simplicity, and to limit computational expense, the local vertical gradient (x_3 being the vertical coordinate) of the (filtered) potential temperature is replaced by the vertical gradient of its horizontally-averaged value indicated by $\langle \cdot \rangle$. In future work, the impact of these simplifications will be assessed in more detail. In addition, the term is calculated within the model using a first-order upwind scheme. A short note on the implementation of subsidence can be found in appendix 3.A.

We use the open-source code MicroHH (<http://microhh.org>), which is a combined finite-difference LES/direct numerical simulation code supporting two-dimensional parallelization using the Message Passing Interface standard. For the advection of momentum and scalars, a second-order finite-difference scheme is used. Integration in time is performed with a low-storage third-order Runge–Kutta algorithm, and pressure is evaluated each timestep by solving a Poisson equation. A damping layer is applied at the top of the domain to prevent the reflection of gravity waves downwards. A full description of the MicroHH code can be found in van Heerwaarden et al. (2017).

3.3.2 Physical model

The simulations are based on the two selected steady-state cases (see Fig. 3.3) for which a steady-state physical model of both the WSBL and VSBL is constructed. A background large-scale temperature difference (inversion strength) $\Delta\theta$ is imposed in the vertical direction, meaning the temperature above the SBL is at maximum $\Delta\theta$ higher than the surface temperature. At the surface, the typical roughness lengths for momentum $z_{0,m}$ and heat $z_{0,h}$ are given below. A linear profile for the subsidence velocity is set to zero at the surface and to w_s at 100 m. The boundary layer is subjected to a large-scale pressure forcing given as the product of the Coriolis parameter f_C and the geostrophic wind speed G . The latter is preset to a fixed value to obtain either a steady WSBL or steady VSBL (see below).

The values of $\Delta\theta$ and G are estimated from the tower observations. Because of the unavailability of detailed high-quality observations extending above the tower height $z > 41.5$ m, uncertainties in the estimated parameter values are introduced. The maximum inversion strength is taken as $\Delta\theta = 25$ K, which is approximately the temperature between the surface and top of the tower in the very stable state (see Fig. 3.3b). Note that, due to the large inversion and limited height, the correction factor between absolute and potential temperature is neglected in our idealization. The geostrophic wind speed is estimated to be $G = 12$ m s⁻¹ in the WSBL and $G = 3.5$ m s⁻¹ in the VSBL. The former value is somewhat lower than the maximum wind speed observed in the weakly stable regime which is possibly influenced by the presence of a nocturnal jet. The value of the subsidence velocity as inferred from the ERA-Interim model reanalysis for the selected period is set to $w_s = -0.004$ m s⁻¹ at $z = 100$ m, and subsequently linearly interpolated to zero at the surface for simplicity. The simulations of Baas et al. (2019) show that this value is representative of the transition of the WSBL to the VSBL under a decreasing geostrophic wind speed (see their Fig. 12c). Furthermore, they show that the average large-scale horizontal advection of temperature is small ($< 10^{-4}$ K s⁻¹) and decreases (approximately) linearly to zero towards the surface (see their Fig. A1), and is, therefore, not included in the current model.

Determining the values of the roughness lengths for momentum and heat is complicated by the large variability of the roughness length found at the Dome C site. Vignon et al. (2017a, see their Fig. 3) show that the aerodynamic roughness length can vary over two orders of magnitude depending on the wind direction and surface temperature, which is partly due to the preferential alignment of sastrugi, i.e., small snow ridges. As during our selected case, the near-surface wind direction is from the south and surface temperatures are -70°C to -60°C , a value for the aerodynamic roughness length of $z_{0,m} = 0.001$ m is adopted. Based on Vignon et al. (2017a), the roughness length for heat is set to $z_{0,h} = z_{0,m}/10$.

An overview of the model parameters and other physical parameters set in the model is given in Table 3.1.

Table 3.1: Overview of model and physical parameters.

Name	Symbol	Value
Geostrophic wind speed (WSBL)	G [m s^{-1}]	12
Geostrophic wind speed (VSBL)	G [m s^{-1}]	3.5
Maximum inversion strength	$\Delta\theta$ [K]	25
Subsidence velocity at 100 m	w_s [m s^{-1}]	-4×10^{-3}
Roughness length for momentum	$z_{0,m}$ [m]	1×10^{-3}
Roughness length for heat	$z_{0,h}$ [m]	1×10^{-4}
Reference temperature	θ_0 [K]	235
Coriolis parameter	f_C [s^{-1}]	1.39×10^{-4}
Acceleration due to gravity	g [m s^{-2}]	9.81
von Kármán constant	κ	0.4
Smagorinsky constant	c_s	0.12
Turbulent Prandtl number	Pr_t	1

3.3.3 Numerical set-up

As the focus is on simulating the typical Antarctic WSBL and VSBL, the simulation must be designed to reach a steady state in phase space (cf. the green and purple circles in Fig. 3.2). Unless stated otherwise, we follow a procedure similar to the GABLS1 study (see, e.g., Beare et al. 2006; Sullivan et al. 2016). The simulation is initialized with constant temperature θ_0 throughout the domain and at the surface, and with the x -component of the velocity equal to the geostrophic wind speed ($\mathbf{u} = \{G, 0, 0\}$) at all levels. Random perturbations are added to the velocity components below the height of the damping layer z_{bf} to trigger turbulence (see Table 3.2). From the start of the simulation, the surface temperature is reduced at a cooling rate of $CR = \{-1; -4\} \text{K h}^{-1}$ for the weakly stable and very stable simulation, respectively, until the surface has been cooled by $\Delta\theta$ (here 25 K), after which cooling ceases (see the sketch in Fig. 3.4). Imposing the required stratification from the onset prevents the initial generation of turbulence by damping fluctuations at the resolved scale. These particular cooling rates are taken as a balance between sustaining the initial development of turbulence and limiting the computational expense. After cooling, the simulation is continued for a number of physical hours to enable the flow to reach a steady state, viz., profiles and fluxes do not vary significantly in time at the end of the simulation. Subsidence heating is switched on from the beginning.

Simulations for the WSBL and VSBL are performed on different domain sizes as the resolution requirements for the VSBL make it too computationally expensive to match the domains. In addition to the highest resolution VSBL simulation, an additional simulation (VSBLc) is performed at slightly coarser resolution to test the convergence of first- and second-order statistics. All runs use an isotropic grid spacing to minimize excessive diffusion in the very stable limit (see section 3.3.1). An overview of the simulations is presented in Table 3.2.

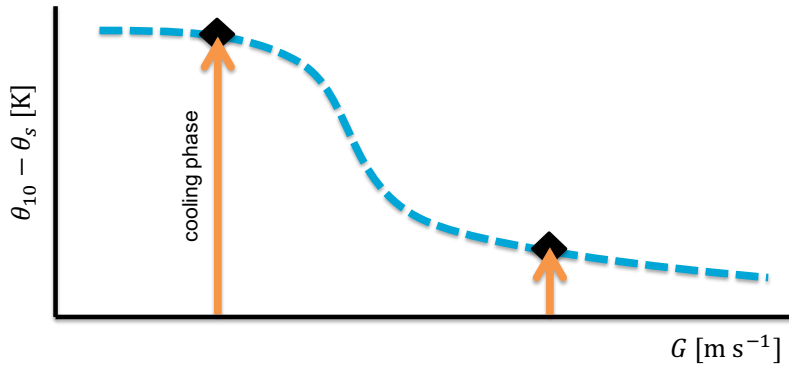


Figure 3.4: Sketch of the initial simulation procedure. The blue curve indicates the steady state of the 10-m to surface inversion strength as a function of the geostrophic wind speed. The orange arrows show the evolution to steady state (black diamonds) from neutral initial conditions by cooling the surface by 25 K and simulating an additional period.

Table 3.2: List of the simulations cases, their geostrophic wind speed G , number of cells N_l , isotropic grid spacing Δ , cooling time t_c , total run time t_r , start of damping layer z_{bf} , surface friction velocity u_* , surface kinematic temperature flux Q_* , surface Obukhov length L , and the height of the boundary layer h . The diagnostic variables are averaged over the final hour of simulation and in steady state.

Run	G [m s^{-1}]	$N_x \times N_y \times N_z$	Δ [m]	t_c [h]	t_r [h]	z_{bf} [m]	u_* [m s^{-1}]	Q_* [K m s^{-1}]	L [m]	h [m]
WSBL	12	$480 \times 480 \times 240$	0.70	25	30	150	0.184	-24.6×10^{-3}	15.6	47.2
VSBL	3.5	$240 \times 240 \times 240$	0.08	6.25	23	15	0.0356	-3.09×10^{-3}	0.915	5.39
VSBLc	3.5	$200 \times 200 \times 200$	0.125	12.5	27	20	0.0365	-3.17×10^{-3}	0.954	5.92

3.4 Numerical results

The steady-state profiles of wind speed and relative temperature are first presented and compared to the observations in section 3.4.1, section 3.4.2 presents the turbulent fluxes, section 3.4.3 discusses the effect of subsidence heating and its implication for a steady-state flow simulated by the LES approach, and section 3.4.4 finally gives a brief sensitivity analysis for the very stable simulation.

3.4.1 General characteristics

The results of the WSBL and VSBL simulations are averaged over the horizontal plane and over the final hour of simulation to calculate bulk quantities and vertical profiles. The simulations reach an approximate quasi-steady equilibrium during this hour, since the relevant quantities do not change significantly. An exception is the presence of an inertial oscillation in the velocity profile with a time scale $T_i \approx 12.6$ h. The time-averaged surface friction velocity u_* , surface kinematic temperature flux Q_* , surface Obukhov length L , and diagnosed boundary-layer height h are listed in Table 3.2. Here, we diagnose the boundary-layer height using the method used by Kosović and Curry (2000) and Beare et al. (2006). First, the height at which the total horizontal stress reaches 5% of its surface value is calculated, and is subsequently linearly extrapolated to the height at which the stress vanishes assuming a linear stress profile.

Figure 3.5 shows the profiles of wind speed, relative wind direction, and relative temperature for the WSBL (top row) and VSBL (bottom row) simulations compared with the observed values (red) of our selected cases. The observed wind directions are shifted to match the simulated values at $z = 1.23$ and $z = 18.11$ m for the WSBL and VSBL cases, respectively (see below).

In general, good agreement between the simulated and observed wind speeds is found for the WSBL case. With the exception of the highest observation level, discrepancies between the simulation and observations are less than 0.9 m s^{-1} . The estimate of the geostrophic wind speed for this case appears to be realistic. As noted in section 3.2.3, the observed wind speed in the WSBL case at 41.2 m is possibly influenced by the presence of a local wind-speed maximum. Correspondingly, the simulation exhibits a jet with maximum 13.1 m s^{-1} (about 9% of G) at $z \approx 43$ m.

In the WSBL case, the observation tower does not capture the full extent of the boundary layer and its associated wind turning. For this reason, the observed and simulated values of the wind direction are matched at the lowest observation height. A relatively good correspondence is found for the relative wind direction for the WSBL case, where the turning of the wind with respect to height is accurately represented by the simulation with the exception of the highest observation level, which appears to deviate from the lower observations. No explanation for this observed value is found. However, a partial blocking of the aerovanes due to riming or deposition of ice cannot be excluded. The total wind turning at the surface is approximated by local linear extrapolation (over five points) of the simulated values and is

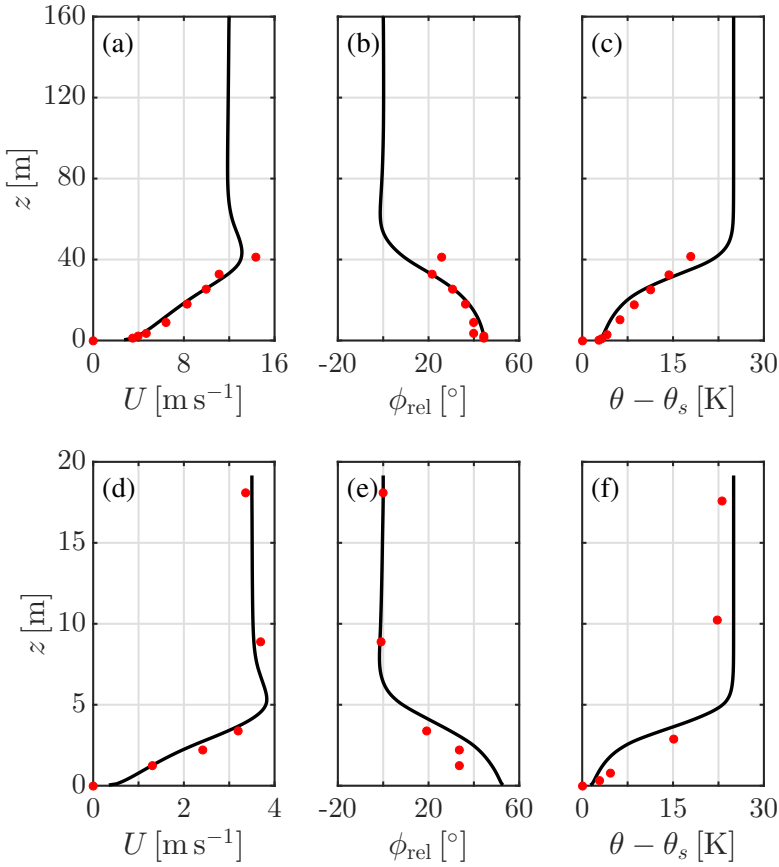


Figure 3.5: Simulated vertical profiles (black) and observed values (red bullets) of (a,d) wind speeds (b,e) relative wind direction and (c,f) air temperature minus the surface temperature for the WSBL (top row) and VSBL (bottom row) cases. The simulated profiles are averaged over the final hour of the simulation. The horizontal scale for wind speed and the vertical scales for all variables are not equal for the WSBL and VSBL cases.

approximately 45°.

As the boundary-layer depths in the simulations and observations are similar, the relative temperature profiles are comparable, but a number of differences remain. The observed temperatures increase more rapidly with height below 25 m than the simulated temperatures, but more slowly above 25 m. Except near the surface, the observed temperature profile appears to be more linearly shaped and has only a weakly pronounced inflection point. This is in contrast to the simulated temperature profile, which exhibits two pronounced inflection points at approximately 5 m and 35 m, resulting in a strongly ‘convex–concave–convex’ profile. At the second inflection point, the averaged temperature gradient in the simulation attains a local maximum of $\partial_z(\theta) = 0.85 \text{ K m}^{-1}$, which is twice as large as the observed gradient $\partial_z T_{\text{obs}} \approx 0.4 \text{ K m}^{-1}$. Mirocha and Kosović (2010) show that a relatively small

increase in the subsidence rate leads to an increased magnitude of the potential temperature gradient throughout the bulk of the boundary layer in addition to a lower boundary-layer height.

For the VSBL case, the agreement between the simulated and observed wind speed is remarkably good, with the difference $< 0.5 \text{ m s}^{-1}$ (see Fig. 3.5d), and the estimate of the geostrophic wind speed appears to be accurate. The hour-averaged simulation result indicates the occurrence of a weak low-level jet at $z \approx 5.3 \text{ m}$ with peak wind speed 3.8 m s^{-1} (10% of G). It should be noted that the full simulation of the VSBL case at steady state covered one inertial period (12.6 h) during which the strength of the jet ranges from 3.7 to 4 m s^{-1} . The inertial oscillation has a minor impact on the velocity profile below the jet ($z \leq 4 \text{ m}$) resulting in variations of 0.1 m s^{-1} (not shown).

The wind directions are compared to the observed value at 18 m as this point is situated above the bulk of the boundary layer. Close to the surface, the observed and simulated wind directions deviate by $10\text{--}15^\circ$, but, particularly under low wind speeds, the observed wind direction is not fully reliable. Local linear interpolation towards the surface results in a total wind turning of 52° in the simulation, which is slightly larger than in the WSBL case.

The simulated temperature profile in the VSBL case has the same overall shape as in the WSBL case (cf. Fig. 3.5c, f), but with the change in temperature distributed over a smaller total height. In the lowest 5 m, the horizontally-averaged temperature gradient varies between $\partial_z \langle \theta \rangle \approx 1.4 \text{ K m}^{-1}$ at the lowest inflection point ($z \approx 0.4 \text{ m}$) and $\partial_z \langle \theta \rangle \approx 7.8 \text{ K m}^{-1}$ at the second inflection point situated at 3.6 m. Here, the gradient from the surface to the first grid point above the surface is excluded as MOST is applied from the surface to this level. At the same time, the observed bulk gradient between $z = 0.7$ and 2.9 m is equal to $\Delta T_{\text{obs}} / \Delta z \approx 5 \text{ K m}^{-1}$. Although the boundary layer is under-sampled in the very stable case, since not enough measurement levels are present on the tower, the shape of the observed temperature profile is expected to be exponential (see section 3.2.3). Both Estournel and Guedalia (1985) and Edwards (2009) show that the inclusion of radiative fluxes in a one-dimensional model indeed results in a more exponentially-shaped temperature profile for low geostrophic wind speeds, and so it is expected that the inclusion of radiative transfer in future simulations will improve the agreement with the observed temperature profile.

The simulated profiles suggest that the boundary-layer heights are approximately 40 m and 5 m for the weakly stable and very stable cases, respectively, where the height of the jet is used as a proxy. An accurate prediction from the observations is impossible. Whereas in the WSBL case, the tower is not high enough to capture the full boundary layer, the region $z = 4\text{--}10 \text{ m}$ is under-sampled in the VSBL case. Nevertheless, the simulations and observations seem to be in agreement on the order of magnitude of the boundary-layer height. Note that, following Nieuwstadt (1984) and Banta et al. (2006), the profiles can be scaled using diagnosed values at the surface or jet maximum height. Such scaling of our simulated boundary layer results in a rather similar structure between the WSBL and VSBL cases (not shown), qualitatively resembling the non-dimensional profiles of Nieuwstadt (1984). In summary,

although a number of estimates and assumptions have been made, and radiative processes have been omitted, the simulations successfully mimic the selected weakly stable and very stable regimes found during the Antarctic winter.

3.4.2 Turbulent fluxes

Figures 3.6 and 3.7 show the total and resolved fluxes of momentum $F(u_i)$ ($i = x, y$) and temperature $F(\theta)$ for the WSBL and VSBL cases, respectively. Note that, for clarity, a different notation is adopted here for the vertical fluxes as compared with the tensor notation in Eq. 3.1 (e.g., $F(u_i)$ instead of τ_{i3}). In the WSBL case, the total cross-isobaric momentum flux at the surface is equal to the isobaric flux, whereas in the VSBL case, the surface cross-isobaric momentum flux is found to exceed the isobaric flux by approximately 30%. Here, isobaric and cross-isobaric are defined as being parallel and perpendicular, respectively, to the direction of the geostrophic velocity aligned along the x -coordinate. The increasing ratio of the cross-isobaric to the isobaric momentum flux for increasing stratification was also reported by Sullivan et al. (2016).

Inspection of the momentum-flux profiles reveals that, at the diagnosed boundary-layer height (see Table 3.2), the isobaric momentum flux is reduced to $< 1\%$ of its surface value. The corresponding reduction for the cross-isobaric momentum fluxes is found to be $\approx 5\%$. In both simulations, the relative contribution of the SFS fluxes to the total fluxes increases near the top of the boundary layer, and accounts for roughly half of the flux at the top of the SBL. In the lower half of the SBL, more than 80% of the momentum fluxes are resolved for both cases with the exception of the first gridpoint above the surface where MOST is applied.

The total temperature fluxes have a tendency towards a constant value with height close to the surface (see Figs. 3.6b and 3.7b), whereas more curvature is present in the SBL further from the surface, which contradicts the results for the typical SBL at mid-latitudes (see, e.g., Nieuwstadt 1984; Galmarini et al. 1998; Beare et al. 2006; Svensson et al. 2011), where quasi-steadiness implies a linearly decreasing temperature flux. This discrepancy with the traditional shape can be explained by the role of subsidence heating in our simulations, which is discussed further in section 3.4.3. The kinematic temperature fluxes at the surface correspond to surface heat fluxes of $H_0 = -24.7 \text{ W m}^{-2}$ in the WSBL case and $H_0 = -3.1 \text{ W m}^{-2}$ in the VSBL case. Although the gradient Richardson number Ri_g exceeds 0.25 at $z > 2.5 \text{ m}$ for the VSBL case, the local shear is sufficient to maintain continuous mixing throughout the bulk of the boundary layer. As for the flux of momentum at the top of the SBL, the SFS scheme accounts for roughly half of the total flux. The explanation for this reduction in the amount of resolved fluxes may be twofold. First, somewhat unsurprisingly, the mesh size is no longer sufficient to resolve the same proportion of the flux-carrying eddies as the characteristic length of the large eddies is reduced by the increased amount of stratification with respect to the shear, viz., an increase in the gradient Richardson number. As a consequence, more flux has to be accounted for by the SFS scheme. Note also that the SFS fluxes may be partly overestimated,

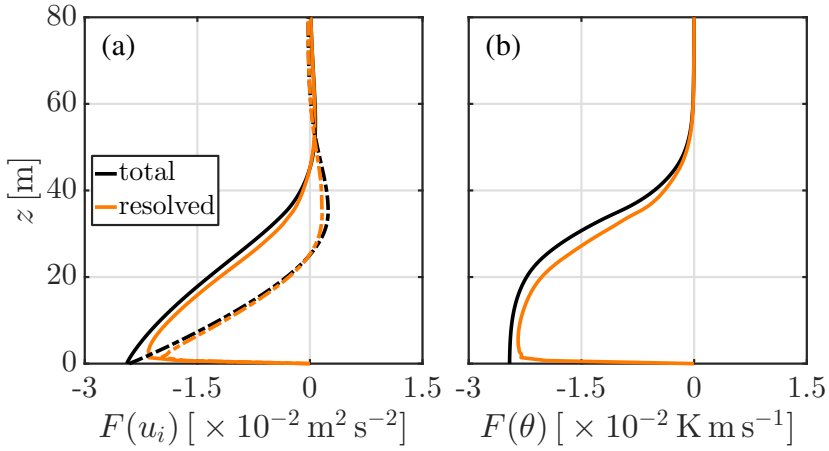


Figure 3.6: Vertical profiles of the vertical fluxes of (a) the isobaric (solid) and cross-isobaric (dashed-dotted) momentum and (b) temperature for the WSBL simulation. Total and resolved fluxes are coloured in black and orange, respectively. The simulations are averaged over the final hour of the simulation.

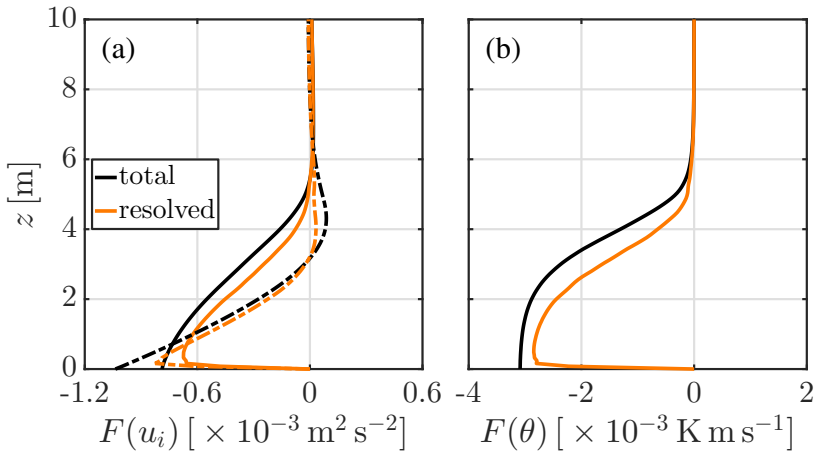


Figure 3.7: As in Fig. 3.6, but for the VSBL simulation. The scales differ with respect to the WSBL simulation.

since the eddy diffusivities $K_{m,h}$ may be too large at the top of the SBL, which is an artefact of the Smagorinsky–Lilly-type closure as it depends on the local strain (see Eq. 3.2). Therefore, there may be excessive SFS mixing in weak turbulent flow with large shear (Germano et al. 1991), but a quantification of these effects is beyond the scope of our study due to the computational requirement of higher resolutions or a change of the SFS scheme. Nevertheless, section 3.4.4 gives a brief sensitivity analysis for the VSBL case.

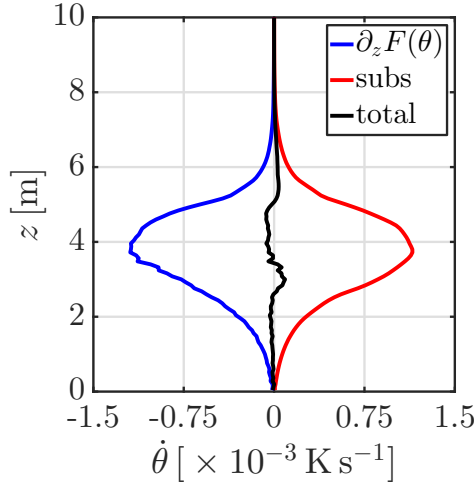


Figure 3.8: Vertical profile of the rate of change of the potential temperature for the VSBL simulation. Note that only the lower half of the computational domain is shown. The simulations are averaged over the final hour of the simulation.

3.4.3 Steady versus quasi-steady?

Figure 3.8 presents the hourly- and domain-averaged vertical profile of the rate of change of the potential temperature $\dot{\theta}$ due to subsidence heating and divergence of the kinematic temperature flux for the VSBL simulation, illustrating that the heating by subsidence has a maximum of approximately $1.14 \times 10^{-3} \text{ K s}^{-1}$ around the inflection point of the temperature profile. The heating rate decreases to zero towards the surface and above the boundary layer. This decrease is caused by a decrease in the subsidence velocity towards the surface and a decrease in the temperature gradient above the SBL, respectively. Interestingly, the cooling induced by the divergence of the total heat flux almost balances the subsidence heating (cf. the black line in Fig. 3.8). Some residual heating and cooling $< 10^{-4} \text{ K s}^{-1}$ is observed in the boundary layer. Possible causes include numerical inaccuracies, i.e., discretization errors, in evaluating the divergence of the temperature flux, and the averaging procedure. Here, the results were averaged over 1 h with statistics output every two simulation seconds. It is expected that, for simulations at higher resolutions, this residual decreases and the total rate-of-changes reach zero. Note that similar results were obtained for the WSBL case (not shown).

The turbulent temperature flux and the heating by subsidence are both internally coupled to the gradient of the temperature field as they depend on and modify the temperature. However, as the heating by subsidence is a slower process, one may suppose that the temperature flux adapts to the subsidence heating. As a result, the shape of the time- and domain-averaged temperature flux profile is such that, at each height, subsidence heating is balanced (see Fig. 3.8), which leads to a horizontally-averaged state of thermal equilibrium in which the averaged temperature does not change in time. A general, but simple, condition for this steady state is given by

integrating the evolution equation for the horizontally-averaged temperature $\langle \theta \rangle$

$$\frac{\partial \langle \theta \rangle}{\partial t} = 0 = -\frac{\partial \langle F_z(\theta) \rangle}{\partial z} - w_s(z) \frac{\partial \langle \theta \rangle}{\partial z} \quad (3.4)$$

in which the horizontal transport terms are neglected due to horizontal homogeneity. Additionally, the change of temperature due to the divergence of the subsidence velocity w_s is also neglected (see appendix 3.A). Setting the rate of change equal to zero and integrating in the vertical direction gives the condition

$$-\langle F_s(\theta; s) \rangle \Big|_{s=0}^{s=z} - \int_0^z w_s(s) \frac{\partial \langle \theta \rangle}{\partial s} ds = \text{constant}, \quad (3.5)$$

where a dummy variable s is used to represent height. The value of this constant is zero as both contributions on the left-hand side vanish at the surface. Indeed, this is consistent with the simulated temperature flux that tends towards a constant value with respect to height near the surface for both the WSBL and VSBL simulations (see Figs. 3.6b and 3.7b) since, near to the surface, the integral contribution of subsidence heating is close to zero. Furthermore, this condition implies that the integrated amount of subsidence heating is equal to the surface flux of temperature, thereby setting an integral constraint.

The steady state at the Dome C site is different from the quasi-steady conditions sometimes encountered at mid-latitudes (Nieuwstadt 1984). In the absence of subsidence, the SBL continues to cool as a whole, whereas the shape of the vertical temperature profile remains largely unchanged in time (Derbyshire 1990; van de Wiel et al. 2012a). The condition for the quasi-steady state is found by neglecting subsidence and differentiating with respect to z in Eq. 3.4, and changing the order of differentiation

$$\frac{\partial}{\partial t} \left(\frac{\partial \langle \theta \rangle}{\partial z} \right) = 0. \quad (3.6)$$

As discussed in Derbyshire (1990), true quasi-steadiness is not possible in the realistic atmospheric SBL. For a quasi-steady, continuously cooling SBL with zero heat flux at the SBL top, the temperature contrast between the bulk and the top would become unlimited (and so would the local Richardson number). In the absence of any gradient-smoothing processes, e.g., radiation or molecular diffusion, this would result in a singularity at the top of the SBL. As such, even quasi-steadiness is not achievable in the mid-latitudes, which makes the present case an attractive alternative for idealized studies of the atmospheric SBL. Indeed, such quasi-steady behaviour has been approached in LES studies of the SBL without subsidence (see, e.g., Beare et al. 2006; Zhou and Chow 2011; Sullivan et al. 2016). A disadvantage, however, is that a continuous surface cooling or surface heat flux has to be prescribed to more-or-less approach this quasi-steady state.

The results indicate that the inclusion of a source term of energy by subsidence opens the possibility of attaining a true thermal steady state for LES investigations of the SBL apart from possible inertial oscillations. It is important to note that a similar conclusion was reached by Mirocha and Kosović (2010), who show that the

inclusion of subsidence results in a “nearly steady behaviour” of the SBL in their LES case, which applied a cubic subsidence profile and the calculation of the heating rate per grid cell using the local thermal gradient. Interestingly, observations in the Arctic clear-sky SBL by Mirocha et al. (2005) provide compelling evidence that a significant part of the negative turbulent heat flux at the surface is balanced by warm air entrained into SBL by subsiding motions. Similarly, the importance of subsidence on the near-surface Antarctic heat budget was also found in model studies of regional climate and the general circulation (van de Berg et al. 2007; Vignon et al. 2018).

3.4.4 Sensitivity to resolution

A Smagorinsky–Lilly closure with stability correction is used despite its limitations and dependence on model parameters, such as the Smagorinsky constant and grid size. However, Matheou (2016) shows that the Smagorinsky–Lilly-type closure can accurately simulate the moderately stable boundary layer and give results comparable to the reference stretched-vortex SFS model (Chung and Matheou 2014; Matheou and Chung 2014), but an a priori choice of the optimal model parameters and resolution is challenging.

A first and relevant test for consistency of the LES approach is to investigate the grid convergence by investigating whether first- and second-order statistics reach a constant value for a change in resolution. Figure 3.9 shows the simulation results for the wind-speed profile and kinematic temperature flux for the VSBL and VSBLc simulations at 0.08-m and 0.125-m resolution, respectively. While the simulated wind-speed profiles are similar with differences $< 0.03 \text{ m s}^{-1}$, the highest resolution simulation has a slightly lower jet height than the case with a coarser resolution, with the difference in jet height approximately 0.25 m. Additionally, a steeper increase of the temperature is found for the VSBL simulation than for the VSBLc simulation, with the maximum difference reaching about 1.5 K at a height of 4.7 m (not shown).

Some differences are also found in the second-order statistics, such as the kinematic temperature flux (see Fig. 3.9b). For the highest resolution of 0.08 m, the total and resolved fluxes are both negligibly small above the diagnosed boundary-layer height, although the SFS contribution reaches approximately 50% near the top of the boundary layer. Physically speaking, at the top of the SBL, the vertical temperature gradient (hence local gradient Richardson number Ri_g) can become very large (cf. Fig. 3.5c, f), so that the integral length scale may locally become smaller than the grid size. As expected, the SFS contribution is enlarged in the case of a coarser grid. Here, the resolved temperature flux becomes zero at 4.5 m, whereas the SFS fluxes only become negligibly small around $z = 7$ m. First, this indicates that, in the region $z = 4.5$ to 5.5 m ($\approx h$ in the highest resolution run), the dominant turbulent length scale is reduced below the grid spacing of 0.125 m due to the increased stratification. Second, it suggests that, in the coarse-grid case, the region $z = 5.5$ –7 m is influenced by excessive diffusion of the SFS scheme. The increase in boundary-layer height for lower resolutions is consistent with Beare et al. (2006) and Sullivan et al. (2016).

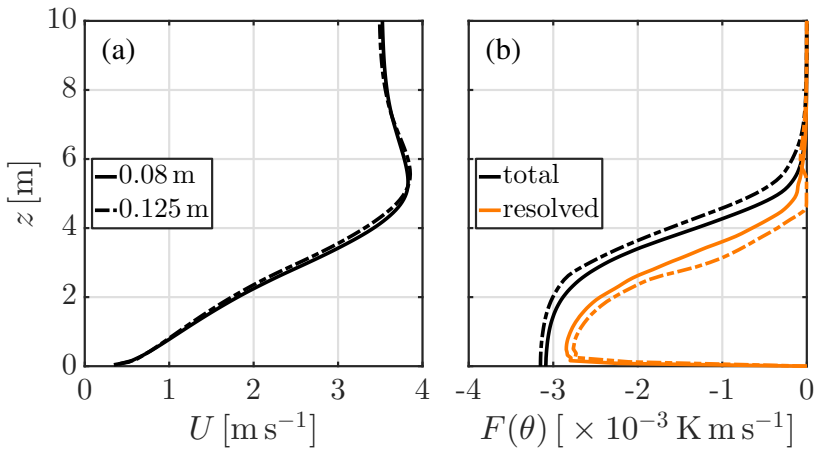


Figure 3.9: Vertical profiles of (a) the wind speed and (b) the vertical flux of temperature for the VSBL simulation [0.08-m resolution; solid line] and VSBLc simulation [0.125-m resolution; dash-dotted line]. Total and resolved fluxes are coloured in black and orange, respectively.

In contrast, the relative difference in the surface kinematic temperature flux is only 2.5%, with the corresponding differences for the surface momentum fluxes of 4.5%, which shows that, for a small change of resolution, the eventual surface fluxes are robust. Although the relative difference is small, it is not known how this difference changes under a further increase (or decrease) of resolution. Due to a combination of long integration times and the required number of grid points, an investigation of possible grid convergence for a doubling of the resolution to 0.04 m, for example, is beyond the current scope of research. However, also taking into account that both the total and the resolved flux become negligible at the same height for the 0.08-m simulation, it is expected that a further increase in resolution would not significantly change the diagnosed boundary-layer height or surface fluxes, but merely increase the contribution of the resolved fluxes to the total fluxes.

3.5 Outlook

The results indicate that the inclusion of heating by subsidence enables the simulation of the steady-state WSBL and VSBL with the LES strategy. As the Dome C site is subject to a persistent continental-scale subsidence related to the divergence of katabatic flow (James 1989), this same process is likely to contribute to the observed quasi-steady behaviour at the Dome C site, which is in contrast to mid-latitude boundary layers, such as at Cabauw. Additionally, whereas the SBL height usually ranges from 100 m to 300 m at Cabauw (Baas et al. 2009), the SBL height at the Dome C site is typically < 50 m even in the weakly stable regime (Pietroni et al. 2014). These features make the wintertime Antarctic boundary layer an ideal test case for research models aiming to study the long-lived SBL at (relatively) high res-

olution. However, a number of challenges remain both from an observational and a modelling perspective.

In section 3.4.1, a comparison of mean variables, such as the wind speed and temperature, with the observations is made. Unfortunately, during the observational period used, the harsh, cold conditions prevented accurate measurements of turbulent fluxes by standard sonic thermo-anemometers (Vignon et al. 2017a), preventing a one-to-one comparison of turbulent fluxes. Note, however, that sonic anemometers have been operated before in similarly harsh conditions (e.g., King and Anderson 1994). As an alternative to sonic anemometry, scintillometry could be used to infer turbulent fluxes over the Dome C station. For example, Hartogensis et al. (2002) show the potential of measuring turbulent fluxes in the SBL using displaced-beam small-aperture scintillometry during the CASES-99 campaign to obtain statistically-accurate fluxes for short averaging times < 1 min (cf. their Fig. 5) and close to the surface, which is not possible using traditional eddy-covariance techniques. Scintillometry has previously been applied in wintertime conditions in Scandinavia (de Bruin et al. 2002) and on sea-ice (Andreas 2012).

Apart from observing turbulent surface fluxes, information on the turbulent state of the atmosphere may also be obtained using remote-sensing techniques, such as sodar techniques. Recently, Petenko et al. (2019) demonstrate the use of high-resolution sodar at the Dome C station in similar conditions to ours to confirm the occurrence of both very shallow continuous turbulent layers of depth < 10 m and less shallow layers extending up to 60 m. An example of the sodar backscatter signals obtained during the winter of 2012 is given in Fig. 3.10, indicating boundary-layer heights of approximately 40 m and 2–5 m in the top and bottom panels, respectively, which qualitatively resemble the two selected cases used here, confirming that the SBL can be extremely shallow at the Dome C site as compared with the SBL at mid-latitudes. Although an in-depth comparison is beyond the scope here, it would be of interest to compare turbulent parameters inferred from the backscatter signal, such as the structure-function parameter for temperature C_T^2 , with those diagnosed from the LES results, which may provide a more direct comparison in the future between simulations and the observed SBL with respect to turbulent intensity.

Apart from (measuring) turbulent mixing, it is expected that radiative processes are equally important for the accurate representation of the near-surface temperature profiles. The radiative-flux divergence is, however, often not measured as a default during field campaigns (see Steeneveld et al. 2010; Gentine et al. 2018, and references therein). Likewise, radiation is generally neglected in the LES modelling of the SBL partly due to its complexity and partly due to its computational expense. In contrast, Edwards et al. (2014) show that a simplified radiation scheme in predefined cases may give improved accuracy in temperature.

In relation to this, our LES model uses a prescribed surface temperature and, as such, the feedback of heat conduction through the snow/ice surface is neglected. While the effect on the simulated steady-state SBL by the LES model subject to constant forcing is assumed to be small, temporal changes and the natural variability of the surface temperature cannot be neglected in a dynamic SBL forced by changing

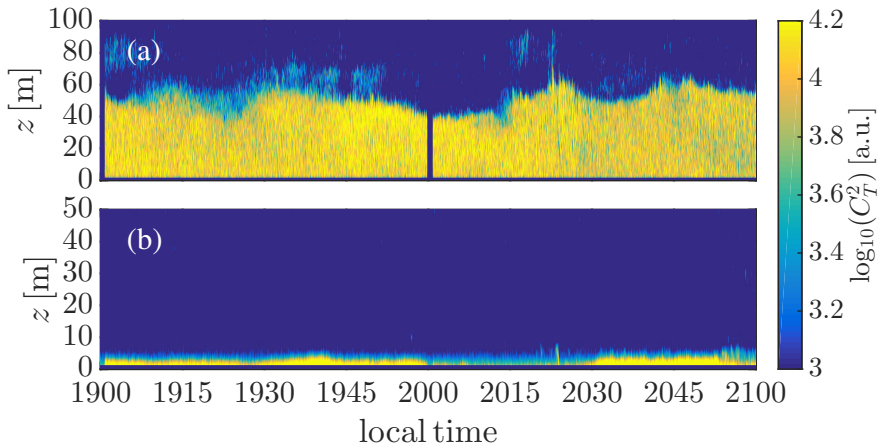


Figure 3.10: Sodar echograms during (a) 27 August 2012 starting at 1900 LT and (b) 31 August 2012 starting at 1900 LT. Adapted from Petenko et al. (2019).

large-scale conditions. During the transition, approximately 25% of the change in the inversion strength is caused by a decrease in surface temperature (see Fig. 3.1). The evolution of the SBL can be influenced by the partitioning of the components of the surface energy budget, which are all strongly interdependent (Steenefeld et al. 2006; King et al. 2006). Therefore, for a future realistic LES approach that captures the observed transition between the WSBL and VSBL cases, such LES models should ideally include both interactive radiation and realistic snow/ice schemes.

3.6 Summary and conclusions

Representative WSBL and VSBL cases observed at the Dome C station have been analyzed and used to set up two realistic LES cases. These two typical boundary layers are taken from a continuous 41-h period in the Antarctic winter of 2015.

Although the Antarctic wintertime boundary layer is undisturbed by the diurnal cycle, transitions within the boundary layer occur at longer time scales. During the selected period, it is observed that all wind speeds measured along the tower decrease, become negligibly small and increase again simultaneously, which is caused by a vanishing and reemerging large-scale pressure gradient. As a result, the boundary layer undergoes transition steadily from the weakly stable to the very stable regime, and back again. Remarkably, the boundary-layer structure appears to map back onto itself after completion of a mechanical cycle in both the weakly stable and very stable limit (cf. Baas et al. 2019).

The two simulation cases are based on these steady-state-limit cases, differing only in the imposed geostrophic wind speed. Heating by subsidence is included as it critically affects the budget of temperature at the Dome C site. The surface is progressively cooled by 25 K after which the simulation is continued to reach steady state.

Generally, a good correspondence between the simulated wind-speed profiles and the observed wind speeds is found for both cases. The simulations exhibit a minor jet with a magnitude of approximately 10% of the geostrophic wind speed. The total wind veering in the simulations amounts to 40–50°, which is in reasonable agreement with the observations. The simulated temperature profiles show a ‘convex–concave–convex’ shape, whereas this appears not to be the case in the observations, with the difference likely due to the lack of radiative transfer in our model, and the assumption of the subsidence profile and magnitude.

The turbulent fluxes highlight the contrast between both the weakly stable and very stable regime, and the extreme SBL at the Dome C site as compared with the mid-latitudes. In the weakly stable regime, the boundary layer extends up to 47 m. In contrast, in both the simulation and observations, only a continuous turbulent layer of approximately 5.5 m is found for the very stable case. Turbulent fluxes in this regime are one order of magnitude smaller than in the weakly stable regime, and this shallow and weak turbulent layer places a strain on the LES model, requiring high resolution near the surface. While a brief sensitivity analysis shows that surface fluxes appear to be robust, ranging from 0.125-m to 0.08-m resolution for the VSBL simulation, complete grid convergence at the top of the boundary layer does not occur due to the presence of the strong inversion.

Heating by subsidence is found to significantly affect the simulated boundary layer, with results suggesting that its inclusion leads to a steady boundary layer whose heating is balanced by turbulent cooling at all heights. The resulting temperature-flux profile contrasts to the usual linear flux profile produced in models without a heat source. A new condition for this thermal steady state is proposed, stating that the integral contribution of subsidence minus the heat flux is constant with height. At the same time, it remains unknown a priori how these two are internally distributed in the boundary layer. As such, the results corroborate the conclusion of Mirocha and Kosović (2010), viz., that the subsidence velocity is an important scaling parameter of the SBL, and further theoretical and simulation work is needed to fully understand the interplay between subsidence, radiation and turbulent heat transfer.

The accurate simulation of both the WSBL and VSBL observed at the Dome C station, appears to be possible given the submetre-scale resolutions of LES models (~ 0.1 m). However, it is expected that further improvements can be obtained with the inclusion of radiative transfer, especially for the very stable case. In addition, an interactive snow/ice scheme would make the study of long-term dynamic effects possible. Due to the uncertainty of the real subsidence, further insight may be gained from varying its magnitude and profile. Apart from these, it would be worthwhile to revisit these cases using a suite of different LES models with differing SFS formulations to test the robustness of the current findings. Finally, a critical test for any LES model would be to simulate the full transition from weakly stable to very stable and back again as observed at the Dome C station.

3.A Calculating the subsidence heating

The heating rate by large-scale subsidence Q_s of the air is usually calculated according to

$$Q_s = -w_s(x_3) \frac{\partial \theta}{\partial x_3}, \quad (3.7)$$

where this source term is subsequently added to the filtered equation for the potential temperature. The subsidence velocity itself $w_s(x_3)$ is not superimposed on the resolved field of the vertical velocity component. Superimposing this term on the vertical velocity component formally results in a second source (sink) term in the equation for the filtered potential temperature

$$Q_{s,2} = -\theta \frac{\partial w_s}{\partial x_3}, \quad (3.8)$$

which represents a change of internal energy due to convergence (divergence) of the flow. However, this second term is commonly not included in the incompressible Navier–Stokes flow with subsidence while, in the current simulations, for example, this term can be of the same order of magnitude. One questions the validity of such an approach.

The presence of a vertical gradient in the subsidence velocity, such as $\partial_{x_3} w_s$, implies an additional large-scale horizontal divergence

$$\frac{\partial \mathbf{u}_{H,s}}{\partial \mathbf{x}_H} = -\frac{\partial w_s}{\partial x_3}, \quad (3.9)$$

where $\mathbf{u}_{H,s} = \{u_s, v_s\}$ is the additional horizontal velocity vector resulting from subsidence. In computational domains with periodic lateral boundary conditions, this large-scale divergence cannot exist and is, therefore, commonly discarded.

However, in turn, this divergence implies the existence of (yet) another term in the budget equation for the filtered temperature

$$D = -\theta \frac{\partial \mathbf{u}_{H,s}}{\partial \mathbf{x}_H}. \quad (3.10)$$

A straightforward substitution shows that this horizontal transport of temperature (energy) at the resolved scale acts to counteract the neglected source term $Q_{s,2}$. Reversing the argument then indicates that discarding the (additional) horizontal divergence is only valid if the term $Q_{s,2}$ is also discarded at the same time.

4

Understanding intermittent bursting at Dome C

High-resolution large-eddy simulations of the Antarctic very stable boundary layer reveal a mechanism for systematic and periodic intermittent bursting. A non-bursting state with a boundary-layer height of just 3 m is alternated by a bursting state with a height of ≈ 5 m. The bursts result from unstable wave growth triggered by a shear-generated Kelvin–Helmholtz instability, as confirmed by linear stability analysis. The shear at the top of the boundary layer is built up by two processes. The upper, quasi-laminar layer accelerates due to the combined effect of the pressure force and rotation by the Coriolis force, while the lower layer decelerates by turbulent friction. During the burst, this shear is eroded and the initial cause of the instability is removed. Subsequently, the interfacial shear builds up again, causing the entire sequence to repeat itself with a timescale of ≈ 10 min. Despite the clear intermittent bursting, the overall change of the mean wind profile is remarkably small during the cycle. This enables such a fast erosion and recovery of the shear. This mechanism for cyclic bursting is remarkably similar to the mechanism hypothesized by Businger in 1973. In his proposed mechanism, the momentum in the upper layer is increased by the downward turbulent transport of high-momentum flow. From the results, it appears that such transfer is not possible as the turbulent activity above the base flow is negligible. Finally, it would be interesting to construct a climatology of shear-generated intermittency in relation to large-scale conditions to assess the generality of this Businger mechanism.

This chapter has been submitted to *Journal of the Atmospheric Sciences* (Nov 2019) as: **van der Linden, S. J. A.**, B. J. H. van de Wiel, C. C. van Heerwaarden, I. Petenko, P. Baas, and H. J. J. Jonker, 2019: A Businger Mechanism for Intermittent Bursting in the Stable Boundary Layer.

4.1 Introduction

This study presents a mechanism for shear-generated intermittent turbulence in the very stable boundary layer (VSBL) based on a high-resolution large-eddy simulation (LES) study, which is representative for conditions on the Antarctic plateau (van der Linden et al. 2019). Here, with intermittent turbulence, we refer to “global intermittency” as defined by Mahrt (1999), where periods of ‘quiescent’ flow are interrupted by sudden bursts of turbulence. It is shown that shear is built up and eroded in a natural, cyclic manner at the top of the boundary layer. The high-shear flow then generates unstable waves that lead to turbulent bursting, which in turn erode the shear itself by which they are generated. Subsequently, a relatively ‘quiescent’ period follows during which shear is built up again. In this study, we will show that this shear-generated intermittency on short timescales (≈ 10 min) is a systematic and periodic feature in our VSBL, and how it contributes to the steady-state VSBL over longer timescales (> 1 h).

Shear-generated intermittent bursting is a frequently observed phenomenon within the weak-wind, stable boundary layer (SBL) (see, e.g., Nappo 1991; Mahrt 1999). In spite of its omnipresence, the reasons behind such intermittent flow have remained unclear as no general dominating mechanism has been identified (Mahrt 1999). Analyzing intermittent flow (from observations) is difficult because the turbulent intensity within the background flow is extremely weak. As such, the effects of local heterogeneities or case-specific disturbances are amplified, and the cause or origin of the burst is easily obscured. Multiple triggers of these events have been identified in literature, for example, density currents and solitary waves (Sun et al. 2004, 2012), spatially dependent (de)coupling depending on local topography (Acevedo and Fitzjarrald 2003), or the interplay between radiative surface cooling and pressure-gradient induced mixing (van de Wiel et al. 2002b). Other frequently observed causes are unstable internal gravity waves resulting from the Kelvin–Helmholtz instability (see, e.g., Gossard et al. 1970; Finnigan et al. 1984; de Baas and Driedonks 1985; Coulter 1990; Nappo 1991; Blumen et al. 2001).

Recently, Petenko et al. (2019) showed that successive wave disturbances frequently occur over periods exceeding several hours during the polar winter of 2012 at Dome C, Antarctica. It, therefore, appears to be a systematic feature of the long-lived Antarctic SBL. Using high-resolution sodar echogram observations, they were able to observe the fine-scale structure of such wave events and estimate both their characteristic temporal and spatial scales. In particular, they show that shear-generated wave disturbances occur under stationary conditions in periodical wave trains lasting 4–6 min even at supercritical bulk Richardson numbers ($Ri_b > 0.25$).

Nearly half a century ago, Joost Businger already proposed a mechanism by which such shear-generated bursts could occur in the VSBL even at supercritical Richardson numbers (see Businger 1973). He conjectured that, if the supercritical Richardson number is reached at a particular height, vertical transfer of momentum and heat is blocked. Locally, shear at this height builds up as the wind below is decelerated (momentum divergence) and wind above is accelerated (momentum

convergence). The shear between the upper layer and lower layer increases until the flow becomes hydrodynamically unstable, and a burst of momentum and heat toward the surface can occur. The shear is rapidly reduced and the flow becomes quiescent again until the next burst. We will show that Businger's mechanism is largely applicable except for one component. Whereas the lower layer is, indeed, decelerated by momentum divergence, momentum convergence is not the major cause of flow acceleration in the upper layer (as turbulent activity is very weak). Instead, the acceleration above is caused by the combination of the pressure force and wind turning due to the Coriolis force rather than by the assumed momentum convergence.

The favorable conditions in the Antarctic winter at the Dome C site may prove to be key in identifying the mechanism for shear-generated intermittent bursts and its periodic occurrence. During these Antarctic winter months (June to August), the SBL at Dome C may reach long periods (lasting for several days) of 'steady state' during which the wind and temperature profiles do not change significantly over time (Vignon et al. 2017b; Baas et al. 2019).

By analysis of observations in combination with high-resolution LES, Van der Linden et al. (2019) show that, in the Antarctic, a thermal steady state is possible when the turbulent cooling of the SBL as a whole is balanced by heating through large-scale subsidence (see also Vignon et al. 2018; Baas et al. 2019). The close correspondence between their LES results and the observations encourages the use of LESs for in-depth process studies. In contrast to the observations, within LESs, the boundary conditions and forcings can be fully controlled. Therefore, the LES approach is an attractive complimentary tool to study the Antarctic SBL and the associated intermittency found by Petenko et al. (2019). Such simulations have also been used before to study shear-generated instabilities in realistic settings, for example, based on CASES-99 (Zhou and Chow 2014) and the Beaufort Sea Arctic Stratus Experiments (Na et al. 2014).

Ideally, a full mechanistic analysis of intermittency directly from observations would be preferred. Unfortunately, measuring such bursts is complicated by the harsh, cold conditions that make accurate measurements of turbulent fluxes by standard sonic-anemometers challenging (Vignon et al. 2017a). Also, the sodar echogram data, although measured at relatively high spatiotemporal resolution, are not easily transformed into quantitative fluxes (Petenko et al. 2019).

Somewhat surprisingly, the aforementioned LES results of van der Linden et al. (2019) indeed show the presence of periodic turbulent bursts in the VSBL similar to those reported by Petenko et al. (2019). Although the SBL is found to be in steady state with respect to its bulk quantities on an hourly base, closer inspection reveals that the SBL is found to be periodically modulated by episodes of enhanced turbulence originating at the top of the boundary layer on timescales of ≈ 10 min. These events subsequently spread both upward and downward resulting in a temporarily larger boundary-layer height and surface fluxes, respectively.

Here, we further investigate these top-down bursting events in the VSBL case of van der Linden et al. (2019) and show that they are the result of wave breaking after initial growth of a shear-generated instability. Using an extended simulation (viz.,

with a larger domain) at a high resolution ($\Delta = 0.08$ m), the dominant wavelength is identified. The instability of this wave is confirmed by applying a linear stability analysis (LSA) on the background flow. Finally, we will identify the full intermittency cycle: the mechanism of wave growth, bursting, and erosion of the shear layer as well as the restoring mechanism to restore local shear again.

4.2 The steady Antarctic boundary layer?

In this section, we further investigate the LES case of the VSBL of van der Linden et al. (2019) to show the presence of intermittent turbulence. A short overview of their VSBL simulation can be found in appendix 4.A.

Figure 4.1 shows the vertical profiles of the wind speed, potential temperature, kinematic temperature flux and the contributions to rate-of-change of potential temperature averaged over the final hour and the horizontal plane of the simulation. Van der Linden et al. (2019) show that on average (viz., averaged over simulation periods ≥ 1 h), a thermal steady state exists in which cooling of the boundary layer by divergence of the kinematic temperature flux is balanced by subsidence heating of the air. The heating rate of subsidence has a maximum at approximately 3.75 m, and decreases to zero toward the surface and top of the domain where the imposed subsidence velocity and temperature gradient are zero, respectively. Apparently, the profile of the temperature flux ‘adapts’ itself to the profile of subsidence heating, as the latter is a slower process (viz., the average temperature gradient changes over timescales longer than the typical timescale of turbulent mixing).

Although the LES case is found to reach a thermal steady state averaged over periods ≥ 1 h, closer inspection indicates a thermal steady state does not exist over averaging periods of approximately 10 minutes or shorter.

Figure 4.2a presents the horizontally-averaged kinematic temperature flux as function of time and height. The temperature flux exhibits clear periodic behavior in which events of enhanced temperature flux are superimposed on a relatively ‘quiescent’ base state (i.e., a shallow SBL of depth $z \approx 2.5$ – 2.9 m). These main bursting events appear to consistently start at the top of the boundary layer, and subsequently extend both upward and downward. After approximately 200 s, the enhancement of the temperature flux has largely disappeared, although some enhanced values are still observed near the surface < 2 m. The time between the onset of these successive events is approximately 600 s. Similar patterns are also present in, for example, the horizontally-averaged momentum fluxes and temperature variance. Conceptually, a ‘short’ timescale of ≈ 200 s (or ‘fast’ process) can be defined in which the bursts affects the mean flow, and a ‘long’ timescale of ≈ 400 s (or ‘slow’ process) in which the conditions favorable for the subsequent burst are created. As the magnitude of the bursts is relatively small (e.g., $O(10)$ W m^{-2} in the heat flux), changes in the first-order statistics such as wind speed and temperature remain modest as well during an event; the standard deviations over the entire simulation hour are $\sigma(U) < 0.04 \text{ m s}^{-1}$ and $\sigma(\theta) = 0.29 \text{ K}$ (not shown).

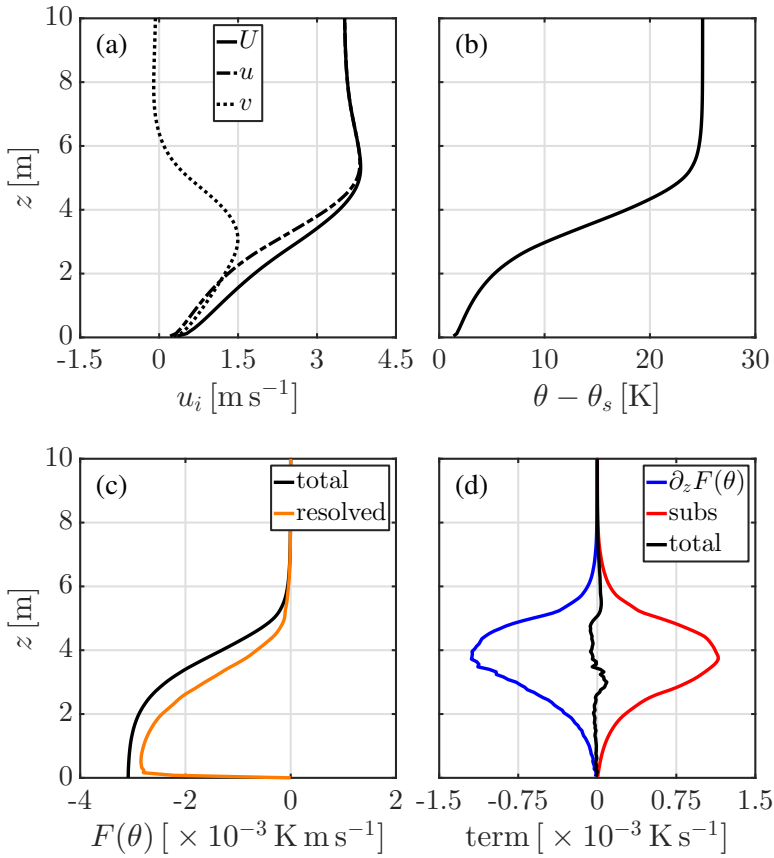


Figure 4.1: Vertical profiles of (a) the horizontal wind speed components, (b) the potential temperature, (c) the kinematic temperature flux and (d) the contributions to the rate-of-change of potential temperature of the VSBL simulations. Both are averaged over the full horizontal domain and over the final hour of the simulation. Note that, only the lower, dynamically ‘active’ half of the domain is shown. Adapted from van der Linden et al. (2019).

Figure 4.2b shows the temporal relation of the kinematic temperature flux at the surface (green) and at the top of the SBL (i.e., at a height of 2.72 m; purple). During a burst, the 2.72-m flux rapidly exceeds the magnitude of the surface flux. On the contrary, the variation in the surface temperature flux is $< 6\%$, which indicates that bursts barely reach the surface. For convenience, we will define two states according to these two fluxes. The bursting intervals are defined as the periods in which the magnitude of temperature flux at 2.72 m exceeds the value of the surface flux. These intervals are indicated by the dash-dotted lines in Fig. 4.2b.

The observed behavior of the temperature flux is consistent with the formation and breaking of travelling waves at the interface of the turbulent boundary layer and the air aloft, which is confirmed by vertical cross sections from the simulation (see section 4.3.1). During the initial stages of the bursting event, (linear) wave

perturbations form and grow in time until nonlinear effects become dominant and cause wave breaking. Subsequently, turbulent kinetic energy is generated at this interface, which causes the boundary layer to grow in height (see Fig. 4.2a). Relatively warm and fast air is entrained into the boundary layer resulting in a net transport of both energy and momentum toward the surface (cf. Fig. 4.2b). This resembles the “upside-down” boundary layer as observed during the CASES-99 experiment (Mahrt and Vickers, 2002).

In addition to these main events (at $z \approx 2.5\text{--}2.9\text{ m}$), a secondary event appears to be initiated above the turbulent SBL in response to the first events (see $z \approx 4.5\text{ m}$, $t \approx 2800\text{ s}$). This secondary event is weak compared to the main events and appears not to penetrate deep into the base state. Its peak values are about 20% of those of the main events. Such secondary events appear to occur sporadically in the simulation. It is unclear if they result from a separate instability or from residual turbulence of the main bursting events. The turbulence on average is weak or even absent at higher levels in the flow ($z > 4\text{ m}$), and the flow can be regarded as ‘quasi-laminar’ and decoupled from the surface layer. Therefore, residual turbulence ejected by the main events may take relatively long to dissipate. Due to its sporadic occurrence and weak impact, these secondary events are discarded in the main analysis.

4.3 Wave analysis

In this section, an in-depth analysis of the wave phenomenon is made. First, wave characteristics are diagnosed from the simulations. The dominant wavelength is extracted by spectral analysis of the vertical cross sections of the velocity field (see section 4.3.1). Second, a linear stability analysis is applied in section 4.3.2 to show that the background flow is indeed unstable in time with respect to this wave perturbation, and that the wave growth enables turbulent bursting.

4.3.1 Spectral analysis

To identify wave properties, such as, the wavelength or amplitude, vertical cross sections of the simulation are analyzed. Before applying the Fourier transform to find the dominant wavelength from the horizontal velocity fields, first a simple visual inspection is made. These suggest a wavelength of approximately 16–19 m in the original VSBL simulation of van der Linden et al. (2019) (not shown). Unfortunately, the full horizontal extent of the domain in their simulations amounts to only $L_x = 19.2\text{ m}$ (with an isotropic grid spacing of $\Delta = 0.08\text{ m}$). Therefore, the wavenumber bin resolution (i.e., its detectable change) Δk is equal to 0.3272 m^{-1} , and accurate determination of the expected wavelength using spectral analysis is unfeasible.

To alleviate this problem, the original simulation is extended in both the horizontal directions according to the following procedure. First, five copies of the original simulation field at $t = 23\text{ h}$ are pasted together in the x -direction. Second, this ‘new’ field is duplicated and joined in the y -direction. Gaussian noise ($\mu_G = 0$; $\sigma_G = 0.02\sigma_i$) is added as a random perturbation, where σ_i is the height-

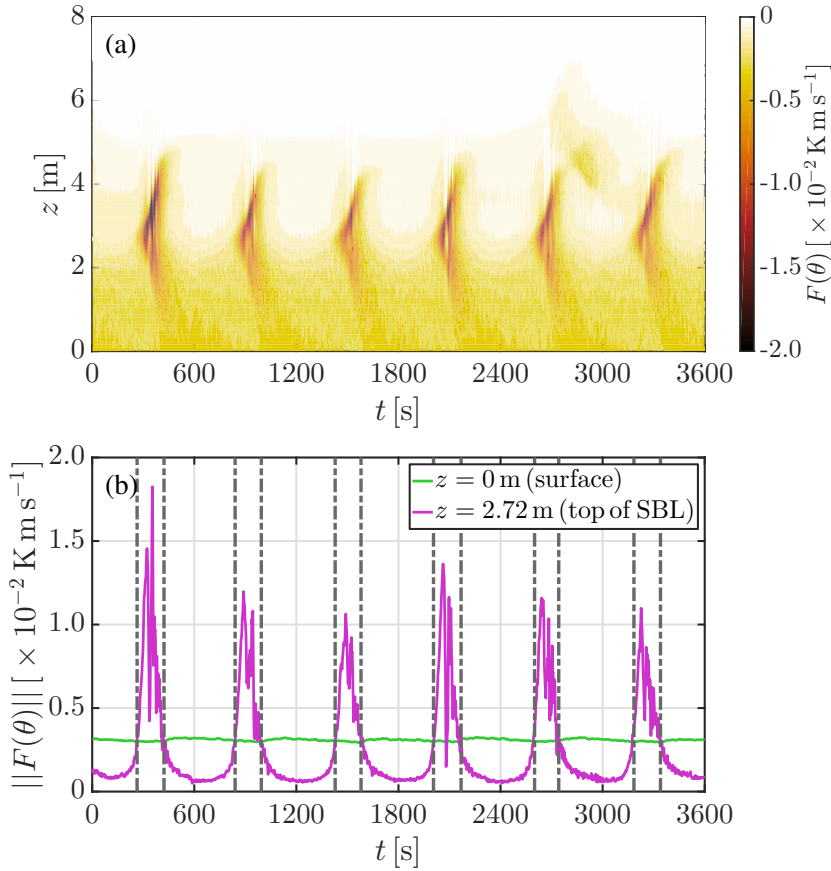


Figure 4.2: (a) Horizontally-averaged kinematic temperature flux as a function of time and height. (b) The temporal evolution of the kinematic temperature flux at 2.72 m (top of the base state; purple) and the surface (green). The dash-dotted lines indicate the bursting intervals.

dependent standard deviation of the variable considered. The perturbation is added to ensure that turbulent fields will not be identical whilst keeping the averaged state unchanged. This is done for all three velocity components and the temperature. The simulation is restarted on the bigger domain with new domain sizes $L_x = 96$ m, $L_y = 38.4$ m and $L_z = 19.2$ m, and is allowed to freely evolve for 2 simulation hours. Only the second simulation hour is used for the analysis as the first simulation hour may be influenced by initial correlation between the individual field copies. As multiple wave cycles have passed during the first hour, it is assumed that these ‘memory effects’ of the artificial initialization have disappeared after the first hour (cf. Fig. 4.2). The grid spacing is kept at 0.08 m. The extended simulation results in a wavenumber bin resolution of $\Delta k_x = 0.065 \text{ m}^{-1}$ in the x -direction (isobaric direction) after application of the Fourier transform.

Figure 4.3 shows the perturbation of the x -component of the velocity u' at different times during a full cycle. Here, the velocity perturbation is defined as the

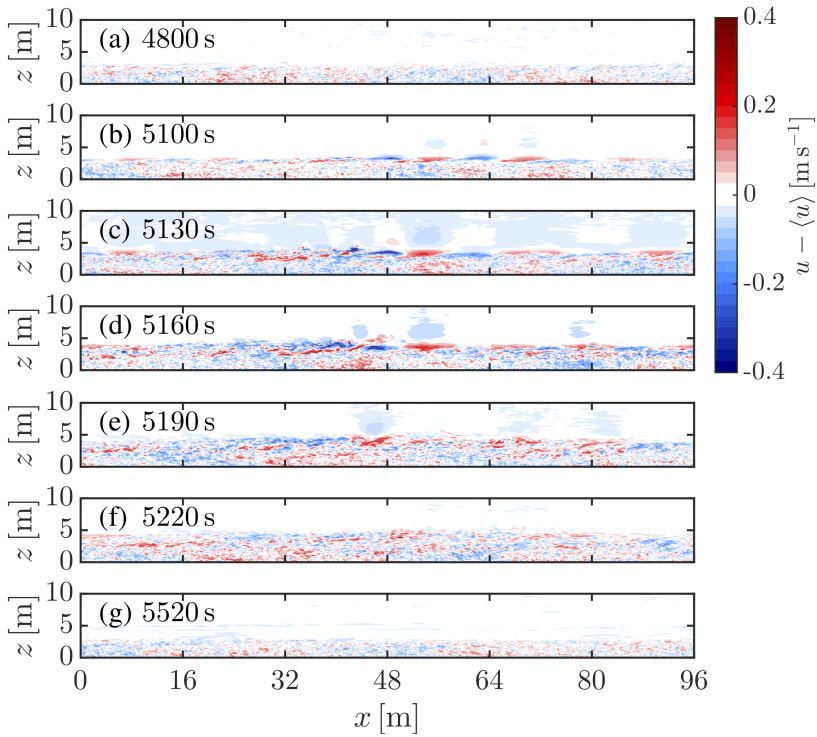


Figure 4.3: Vertical cross sections of the perturbation of the isobaric velocity u' in the xz -plane at multiple times during a wave bursting event: (a) $t = 4800$ s; (b) $t = 5100$ s; (c) $t = 5130$ s; (d) $t = 5160$ s; (e) $t = 5190$ s; (f) $t = 5220$ s; and (g) $t = 5520$ s. Note that only the lower half of the domain is shown.

difference between the local, instantaneous velocity and the horizontally-averaged value. It is observed that at the top of the boundary layer with height of approximately 2.7 m, a wave pattern of alternating positive and negative velocity perturbations forms (cf. Fig 4.3b). Subsequently, the wave amplitude grows in time and eventually breaks. Faster, non-turbulent air is entrained, which leads to an increase of the turbulent boundary layer (cf. Fig 4.3c,d). During the later stages of the event, the wave patterns have disappeared and the boundary layer has grown to approximately 5.5 m with overall increased values of the velocity perturbation indicating an increase in turbulent activity (see Fig 4.3e,f). Finally, the turbulent activity at the top of the boundary layer dissipates, and the boundary-layer returns to its pre-burst state (Fig 4.3g). Similar evolutions are observed for the perturbations of the cross-isobaric velocity component v' , the vertical velocity component w' and the potential temperature θ' (not shown).

To determine the dominant wavelength, the stages similar to Fig. 4.3b are selected from the final three events (out of a total of 4) and analyzed. The first bursting event in the second simulation hour is discarded since it may be influenced by a secondary event (cf. Fig. 4.2a). Using a similar approach as Newsom and Banta

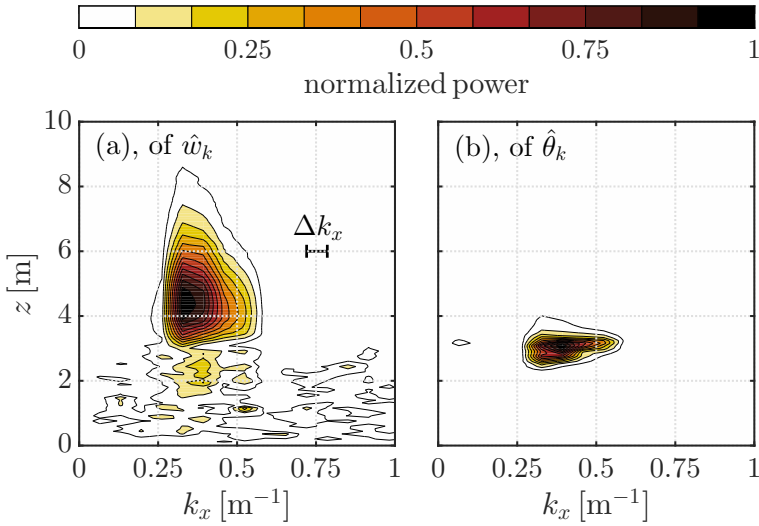


Figure 4.4: Normalized power spectrum of (a) the vertical velocity perturbation and (b) the potential temperature. Only part of the wavenumber range is shown.

(2003), the normalized power spectra at each height z are computed by taking the one-dimensional Fourier transform in the x -direction of each cross section. Individual spectra are added and normalized by its maximum value. The Fourier components of the perturbation of a variable are indicated by the hat-symbol. For example, $\hat{\theta}_k$ refers to the Fourier component at wavenumber $k_x \equiv 2\pi/\lambda_x$ (with λ_x the wavelength in the x -direction; k th mode) of the perturbation in the potential temperature θ' .

Figure 4.4 presents the normalized power spectra of both the vertical velocity component \hat{w}_k and potential temperature $\hat{\theta}_k$ as a function of both height z and wavenumber k_x . For clarity, only wavenumbers up to $k_x = 1 \text{ m}^{-1}$ are shown (out of a maximum of $k_x = 39.22 \text{ m}^{-1}$) as the power at higher wavenumbers is negligible. The spectra of \hat{w}_k and $\hat{\theta}_k$ have their maxima at $k_x = 0.3274 \text{ m}^{-1}$ and $z = 4.36 \text{ m}$, and at $k_x = 0.3929 \text{ m}^{-1}$ and $z = 3.08 \text{ m}$, respectively. The location of the maximum of \hat{w}_k corresponds to a wavelength of $\lambda_x = 19.2 \text{ m}$, while the location of the maximum of $\hat{\theta}_k$ corresponds to $\lambda_x = 16.00 \text{ m}$. Hence, this analysis confirms the aforementioned visual inspection.

Both power spectra have an approximately equal horizontal extent. This indicates that the wave phenomenon is composed of multiple wavelengths in a narrow range. The vertical extent of the power spectrum of \hat{w}_k appears to be larger than that of $\hat{\theta}_k$. No explanation is found for this difference in height of the distribution. The vertical profiles of the power spectra at the dominant wavenumber are shown in Fig. 4.5a,b.

Visual inspection of the simulation field at $t = 5100 \text{ s}$ shows that propagation direction of the primary wave events is $\phi \approx 0^\circ$ with respect to the isobars; that is,

aligned with the x -axis (not shown). For convenience, it is therefore taken as 0° . Unfortunately, no value of the complex phase speed can be calculated due to the limited frequency at which cross sections and simulation fields were saved, namely, 30s and 300s, respectively.

4.3.2 Linear stability analysis

Linear stability analysis provides information about the hydrodynamic stability of small perturbations (indicated by the prime) subject to a given background flow. Arbitrarily-shaped perturbations of small amplitude are typically present in ‘quiescent’, non-turbulent background flows, and can be seen as a superposition of sinusoidal waves (Fourier decomposition). By LSA, one investigates if these wave components (modes) decay or grow in time (i.e., have a negative or positive growth rate). If all modes contained in the Fourier decomposition decay, the flow is said to be stable. However, if a number of modes grow (exponentially in time), it is assumed that the fastest growing mode of these will rapidly dominate over the others and continue to grow until secondary instability mechanisms cause that wave to break and overturn. An extensive overview on LSA can be found in Drazin and Reid (2004) and Kundu et al. (2012). Although LSA is traditionally used to investigate the stability of strictly laminar flows and predict their transition to turbulence (Kundu et al. 2012), the LSA approach has been stretched in its assumptions by applying it to flows that are not completely laminar, but are ‘smooth’ with respect to their very weak turbulent activity. In those cases, LSA is used to analyze whether the mean flow (in a Reynolds-averaged sense) supports unstable wave modes that will lead to turbulence of more significant magnitude. Indeed, LSA has been employed with success to predict shear-generated instabilities in the ‘smooth’, but weakly-turbulent SBL using the observed mean states (see, e.g., Finnigan et al. 1984; de Baas and Driedonks 1985; Newsom and Banta 2003).

Method

Here, we briefly explain the implementation of the LSA. A detailed description can be found in appendix 4.B. First, it is assumed that, at a given time, the wave perturbations propagate along one direction in the horizontal plane. This reduces the 3D problem to a 2D approximation. Note that, this assumption excludes the Coriolis force from the analysis. This simplification is motivated by the magnitude of the perturbation Coriolis term after linearization, which is negligible compared to the other terms. Second, we assume the flow to be inviscid. The velocity vector is then rotated over angle ϕ , which corresponds to an alignment of the flow with the propagation direction (here, $\phi \approx 0^\circ$, section 4.3.1). The mean 2D background states of wind speed and temperature are given by $\mathbf{U} = \{U(z), 0\}$ and $\Theta(z)$, respectively. Travelling-wave solutions are assumed for the wave disturbances. For example, for

the vertical velocity component

$$w' = \sum_k w'_k = \operatorname{Re} \left(\sum_k \hat{w}_k(z) e^{ik(x-c_k t)} \right) = \operatorname{Re} \left(\sum_k \hat{w}_k(z) e^{ikx} e^{\sigma_k t} \right), \quad (4.1)$$

where k is the wavenumber, $\hat{w}_k(z)$ is the complex amplitude (profile) of the k th mode, $c_k = c_{k,R} + ic_{k,I}$ is the complex phase speed. Additionally, $\sigma_k = -ikc_k$ is introduced for convenience. For a mode to be unstable, the real part of σ_k has to be $> 0 \text{ s}^{-1}$. Our LSA model investigates the stability of a single mode solving for the unknown σ_k , and the corresponding profiles of the vertical velocity and temperature perturbations for a given k and ϕ of that mode. Apart from these, boundary conditions for the vertical velocity component have to be specified. Here, we require that the vertical velocity component is zero at the bottom ($\hat{w}_k = 0$; no-penetration) and that the solution remains bounded for infinite height (viz., \hat{w}_k tends to a constant value). The latter boundary condition is approximated by $\frac{d\hat{w}_k}{dz} = -k\hat{w}_k$ at the top of the computational domain. Note that, both $\frac{d^2 U}{dz^2}$ and $\frac{d\Theta}{dz}$ tend to zero here (cf. de Baas and Driedonks 1985; Newsom and Banta 2003). The equation for the temperature perturbation can be eliminated by further substitution and would yield the classical Taylor–Goldstein equation (see, e.g., Newsom and Banta 2003), which is a second-order equation in \hat{w}_k requiring two boundary conditions. Here, this elimination is not done for convenience.

The system of equations is discretized in the vertical direction using N_z levels (the same as in the simulation), and transformed into a generalized eigenvalue problem with eigenvalue σ_k and eigenvector $[\hat{\mathbf{w}}_k, \hat{\theta}_k]^T$. Solving the generalized eigenvalue problems gives $2N_z$ pairs of eigenvalues and eigenvectors of which N_z are independent. For each pair, its complex conjugate is also a valid solution with opposite growth rate (Kundu et al. 2012). The most unstable eigenvalue-eigenvector pair (largest $\operatorname{Re}(\sigma_k)$) is selected as it is expected to dominate the flow evolution.

Result

We investigate the stability of waves with wavenumber and propagation direction set equal to $k = 0.3929 \text{ m}^{-1}$ and $\phi = 0^\circ$, respectively (see section 4.3.1). The background profiles of wind speed and temperature are obtained by averaging the simulated profiles between $t = 5400$ and $t = 5700 \text{ s}$ from the extended domain simulation. This interval is approximately halfway between two successive bursts (based on the 2.72-m temperature flux) and is representative of the base state. The background wind speed profile is then projected onto the plane of propagation, which corresponds to setting $U(z) = u(z)$ in our case. Using these parameters, this investigated mode is found to have as fastest growing eigenvalue $\sigma_k = (0.0195 - 0.7899i) \text{ s}^{-1}$. This corresponds to complex phase speed components of $c_{k,R} = 2.01 \text{ m s}^{-1}$ and $c_{k,I} = 0.05 \text{ m s}^{-1}$, where the subscripts ‘R’ and ‘I’ represent the real and imaginary parts, respectively. The wave speed $c_{k,R}$ equals the speed of the background flow at $z \approx 2.92 \text{ m}$, so that the midplane of the wave does not move in a coordinate system moving with that flow speed. The e -folding timescale for exponential growth is $\approx 51 \text{ s}$

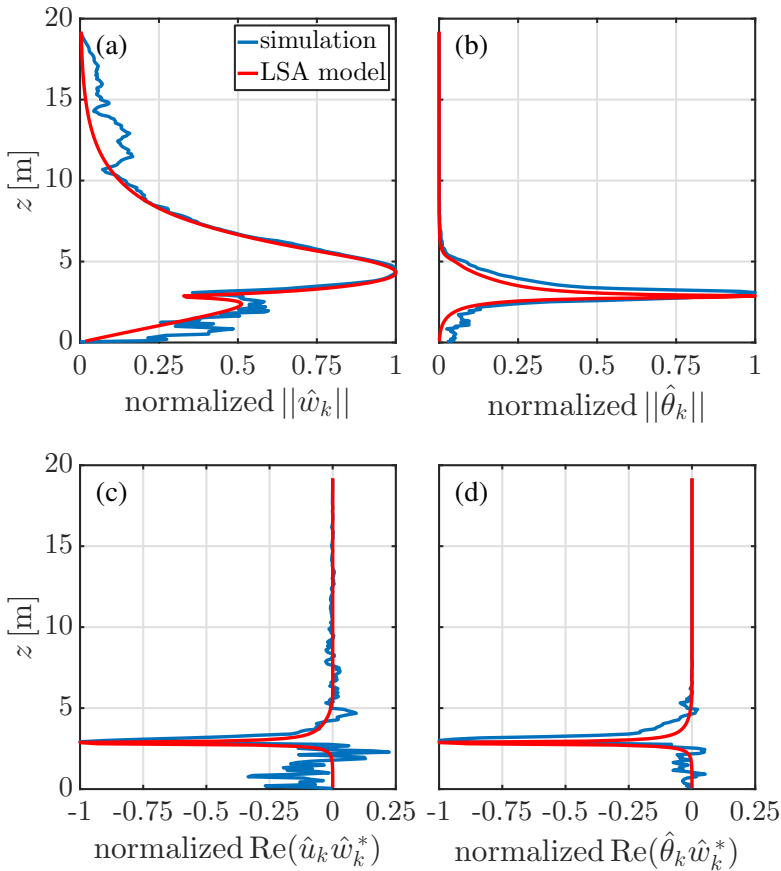


Figure 4.5: Normalized vertical profiles at the dominant wavenumber obtained from the simulation (blue) and calculated by the linear stability analysis (red) of (a) the vertical velocity component, (b) the potential temperature, (c) wave momentum flux, and (d) wave temperature flux.

(i.e., $k^{-1}c_{k,l}^{-1}$). Although this timescale cannot be accurately determined from the simulations due to the limited output frequency of the cross sections, it appears to be reasonable compared to the timescale of the bursting event (cf. Fig. 4.2b). A strict comparison is not possible as the linear growth regime is violated relatively soon due to fast growth of the wave.

Figure 4.5 shows the normalized wave mode profiles of the vertical velocity component, temperature, vertical wave momentum flux and vertical wave temperature flux at the dominant wavenumber $k = 0.3929 \text{ m}^{-1}$ as inferred from the simulation (blue) and calculated by the LSA (red). Here, the vertical ‘fluxes’, resulting from the temporal growth of the wave amplitude, are calculated as the real part of the product of the variable considered and the complex conjugate of the vertical velocity component \hat{w}_k^* (cf. Newsom and Banta (2003)). This product is the generalization of the dot product for complex numbers. For temperature, this product represents that part

of the temperature perturbation that is in phase with the perturbation of the vertical velocity component. Note that, for non-growing (linear) waves ($\text{Re}(\sigma_k) = 0 \text{ s}^{-1}$) this product is zero (viz., $\hat{\theta}_k$ lags 90° with respect to \hat{w}_k), and, as such, no scalar or momentum is transported. However, for growing waves this product is non-zero. Physically, the vertical velocity does not change sign at the moment the densest (lightest) fluid is displaced through the midplane in a wave of which the amplitude grows in time. The presence of an in-phase component (non-zero product) follows from the LSA model equations (see Eq. 4.9b, appendix 4.B)

$$\hat{\theta}_k = \frac{i}{k} \left(\frac{\frac{d\Theta}{dz}}{U(z) - c_k} \right) \hat{w}_k, \quad (4.2)$$

which shows that $\text{Re}(\hat{\theta}_k \hat{w}_k^*) \neq 0$ if and only if $\text{Im}(c_k) \neq 0$.

The calculated LSA-profiles resemble those estimated from the simulation for all four variables to a high degree. Minor differences are mainly found near the surface, which are likely caused by some irregular motion (weak turbulence) of minor amplitude. The LSA-calculated profile for $|\hat{w}_k|$ smoothly tends toward zero near the top of the domain, whereas the profile estimated from the simulations does not. Because turbulent activity is virtually absent in the upper half of the domain (cf. Fig. 4.1), this might indicate some wave activity there (possibly caused by minor reflections). As such, the domain is not large enough to fully exclude boundary effects, although these effects are minor.

A local minimum of $|\hat{w}_k|$, and the maxima of $|\hat{\theta}_k|$ and the wave fluxes are present at $z = 2.88 \text{ m}$ coinciding with the inflection point of the velocity profile $U(z)$. This height is a critical level of the flow: the real part of the phase speed $c_{k,R}$ is equal to the local horizontal velocity at this height. The large, narrow peaks of the wave momentum and temperature fluxes indicate that large parts of \hat{u}_k and $\hat{\theta}_k$ are in phase with \hat{w}_k at this height, whereas they are out of phase near the surface and above the SBL (see Fig. 4.5c,d).

The profiles correspond to those found by de Baas and Driedonks (1985) (vertical velocity and temperature) and Newsom and Banta (2003) in a non-dimensional form. The shape and structure of these profiles are consistent with a Kelvin–Helmholtz-type instability (Newsom and Banta 2003). This confirms that the wave formation and wave breaking (cf. Fig. 4.3) are indeed the result of a shear instability at the top of the SBL.

4.4 Mechanism behind the full cycle

In spite of the close correspondence between the LSA and the simulation results, the previous section merely confirms that the background flow is unstable for perturbations at the dominant wavenumber. It does, however, not reveal how the boundary layer responds during the burst and relaxes back to its base state. In this section, this process is analyzed by conditional averaging over the bursting and the non-bursting periods. First, the effect of the intermittent burst on the mean flow is shown. Second,

the evolution of the boundary layer after a burst is presented and, in particular, it is revealed why the process of shear-generated intermittent bursts is periodic.

4.4.1 Flow evolution during the burst

Figure 4.6 shows the flux profiles of momentum $F(u_i)$ and temperature $F(\theta)$, and the contributions to the tendencies of the isobaric velocity component u and temperature θ . These values are conditionally averaged on the bursting states taken from the final simulation hour of the original VSBL simulation (see van der Linden et al. 2019). These contributions for u are the divergence of the total isobaric momentum flux and the x -component of the Coriolis force, whereas the contributions for θ are the divergence of the kinematic temperature flux and heating by subsidence. The x -component of the Coriolis force is given by $f_C v$. This term does not ‘add’ momentum (or energy) to the flow as the Coriolis force is always perpendicular to the wind vector. However, it can rotate the wind vector thereby transferring momentum (and energy) from the y -direction to the x -direction (and vice versa) in the case of a force imbalance. At the same time, the imposed pressure gradient force steadily adds momentum to the cross-isobaric direction (y -direction). The bursting (non-bursting) state is defined as those time intervals in which the absolute value of the 2.72-m temperature flux is larger (smaller) than the absolute value of the surface temperature flux (cf. Fig. 4.2b). The total fraction of the time the SBL resides in the bursting (non-bursting) state is 26% (74%).

Both the isobaric momentum flux (x -direction) and temperature flux exhibit large negative peaks centred around 2.72 m (cf. Fig. 4.5) exceeding the surface values. The averaged vertical extent of the peaks is approximately equal to 4 m and is dependent on the time during the burst: after the initial wave breaks, momentum and heat are both injected into the turbulent layer and ejected into the air aloft. As a result of the burst, turbulent kinetic energy is generated and the boundary-layer height increases up to ≈ 5.5 m. Additionally, the base state becomes temporarily ‘coupled’ to the layer above.

The x -component of the Coriolis force $f_C v$ and the heating by subsidence both have a positive contribution to the tendencies of u and θ , respectively, and tend to zero for $z > 6$ m (see Fig. 4.6c,d). The contributions as a result of the flux divergences show a more complicated pattern: they are mainly positive in the lower layer and negative higher up. In total, a net acceleration and warming of the SBL occur below ≈ 2.9 m, whereas in the region 3–5 m (relatively) strong deceleration and cooling occur. The vertical transport by bursting, hence, reduces the difference in the velocity magnitude and the temperature between the upper and lower layer, and, as such, counteracts the cause of the instability.

In addition to the isobaric velocity component, also changes in the cross-isobaric component occur. Although the profile of the total rate-of-change of the cross-isobaric velocity component exhibits a more complicated structure, its values are typically $< 50\%$ of the total rate-of-change of u and have a relative small contribution to the change of the total shear squared S^2 (not shown).

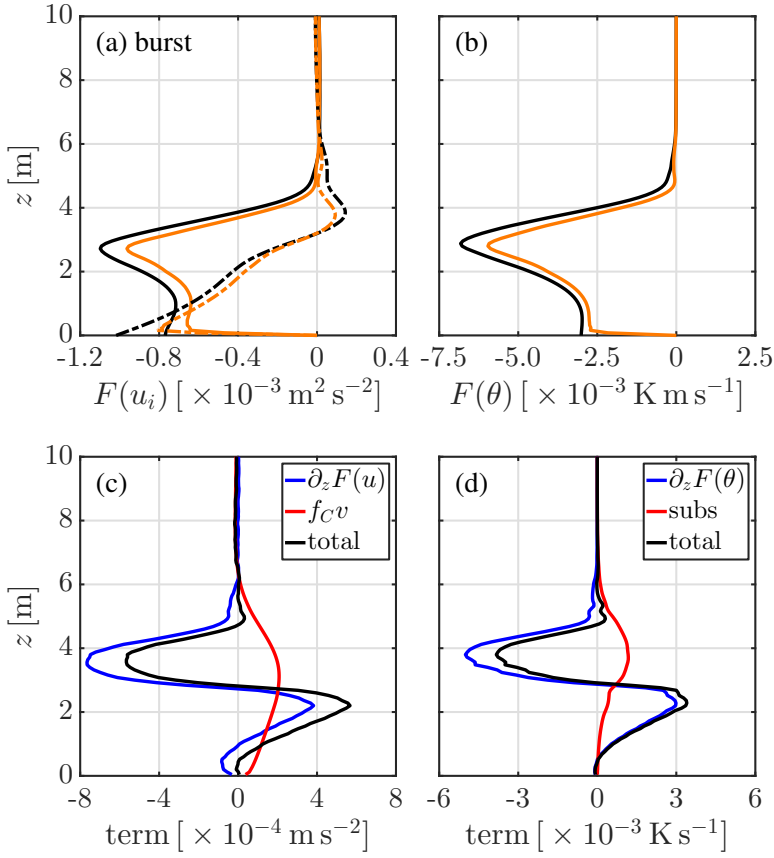


Figure 4.6: Conditionally-averaged profiles during the bursting state of (a) the isobaric momentum flux (solid lines) and the cross-isobaric momentum flux (dash-dotted lines), (b) the kinematic temperature flux, (c) the contributions to the rate-of-change of the isobaric momentum, and (d) the contributions to the rate-of-change of the temperature. Total fluxes are given in black and resolved fluxes in orange.

4.4.2 Flow evolution after the burst

In the non-bursting state, the flux and total rate-of-change profiles are markedly different than in the bursting state (see Fig. 4.7). The profiles of the momentum and temperature fluxes indicate that the main turbulent layer is now approximately 3 m in depth.

It is found that the profiles of the x -component of the Coriolis force $f_C v$ and the heating by subsidence do not significantly differ in the non-bursting state as compared to the bursting state. The figures, however, do differ with respect to the turbulent flux contributions (see Fig. 4.7c,d). In absence of momentum and heat transport from above, the lower layer ($z < 3$ m) decelerates due to the surface friction (momentum flux divergence) and cools by the surface temperature flux (temperature

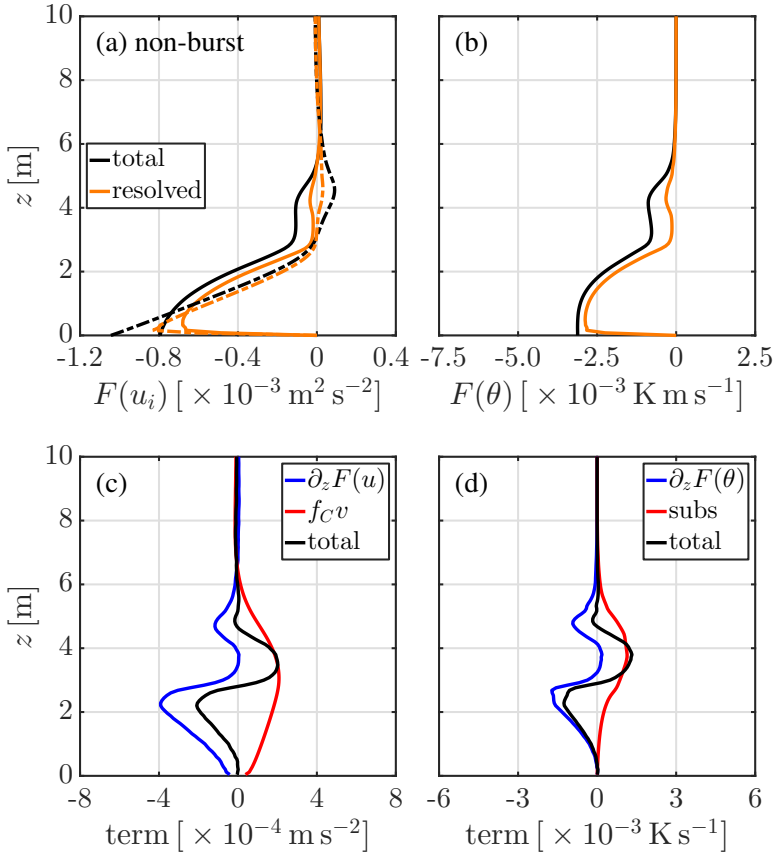


Figure 4.7: As in Fig. 4.6, but during the non-bursting state.

flux divergence). This lower layer corresponds to the active turbulent layer in the non-bursting state, whereas the layer above can be regarded as ‘quasi-laminar’. At the same time, this quasi-laminar layer experiences a net acceleration and warming by the Coriolis force and subsidence heating. The overall result is that the contrast between the lower and the upper layer increases with respect to the wind speed and temperature (i.e., an increase of the local shear and temperature gradient around $z \approx 3 \text{ m}$). The momentum transferred from the cross-isobaric to the isobaric direction by the Coriolis force is steadily replenished by the pressure force in the y -direction (not shown).

Weighted by their respective fractions of occurrence, the deceleration and cooling, and the acceleration and warming balance in time. As such, both a steady state in the amount of momentum and a thermal steady state result, when averaged over, for example, times $> 1 \text{ h}$ (see van der Linden et al. 2019; their Fig. 8). The intermittent bursts of the SBL, therefore, contribute to this thermal steady state in the presence of heating by subsidence. Periodically, they ‘entrain’ relatively warm air heated by subsidence into the turbulent layer. Mirocha et al. (2005) already provided compelling

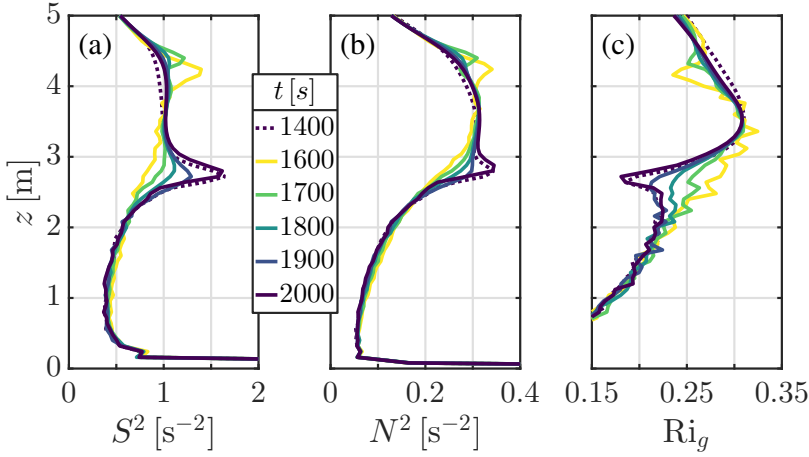


Figure 4.8: Vertical profiles of (a) the total shear squared, (b) the Brunt-Väisälä frequency, and (c) the gradient Richardson number representative for the times $t = 1400$ (pre-burst), 1600 (after burst I), 1700 (after burst II), 1800 (after burst III), 1900 (after burst IV) and 2000s (pre-burst). These are averaged over 20s.

evidence that warm air entrained into the boundary layer by subsiding motions balances a significant part of the turbulent heat flux near the surface in the observed Arctic clear-sky SBL. Similarly, a LES case based on this Arctic SBL (Mirocha and Kosović 2010) shows that the inclusion of subsidence resulted in a nearly thermal steady state. However, they did not report any (periodic) bursts within the SBL.

The impact of the bursting and the non-bursting phases on the mean quantities are summarized in Fig. 4.8. This figure shows the profiles of the total shear squared S^2 , Brunt-Väisälä frequency N^2 and the gradient Richardson number $Ri_g = N^2 S^{-2}$ representative of different times during one cycle (just before a burst and after the burst). The temporal variation in S^2 and N^2 result in clear changes of Ri_g over the shear layer during a cycle. Finally, a conceptual picture of the mechanism and its main actors are given in Fig. 4.9.

4.5 Discussion

4.5.1 Comparison with suggested mechanisms

The current results suggest a systematic mechanism by which cyclic intermittent bursts are triggered by a Kelvin-Helmholtz instability at the interface of a shallow SBL and the quasi-laminar layer above. Similar mechanisms (or parts thereof) have been reported in literature. Yet, a comprehensive, observationally-based explanation by which multiple intermittent bursts may occur successively or even periodically within an uninterrupted timespan has not been given (Mahrt 2014). Indeed, systematic observations of such successive bursts may be difficult due to both observational

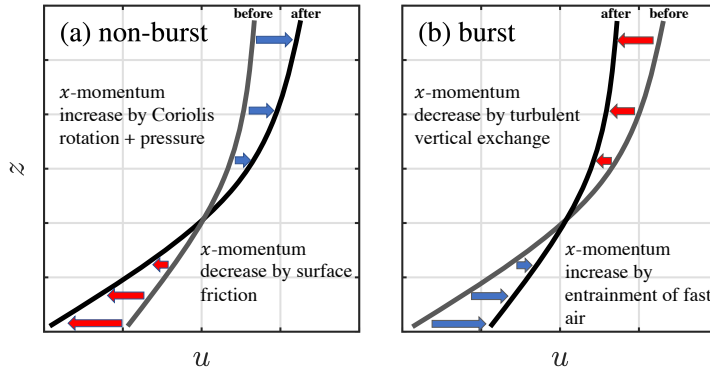


Figure 4.9: Sketch of changes in the profile of u centred at the top of the SBL during (a) the non-bursting state, and (b) the bursting state.

limitations and non-stationarity of the SBL itself in the mid-latitudes.

The mechanism identified in this study resembles the mechanism reported by Newsom and Banta (2003). They show that, just prior to the burst, the shear dominates the reduction of the Richardson number causing the flow to become locally unstable. In particular, the build-up of shear over a relatively small vertical extent triggers a Kelvin–Helmholtz instability. Furthermore, they find a net increase of Ri during the wave event as both shear and temperature gradient are mixed, and a small decrease of Ri after the wave event for which no cause is identified. This observation appears to correspond with our simulations, although a direct comparison is difficult due to observational limitations (e.g., determining gradients from discrete levels) and the number of events (1 in their case).

Also, similarities and dissimilarities between the mechanism of van de Wiel et al. (2002b) and the current mechanism are present. Van de Wiel et al. (2002b) acknowledge the potential role of the ageostrophic pressure gradient (i.e., the effective pressure gradient in the direction of the mean wind) as a main external parameter governing intermittency in their bulk model. The main difference, however, is that their bulk model cannot capture the instability and the dynamics at the interface of the SBL and the quasi-laminar layer above, but considers a suppression of the turbulent activity of the SBL as a whole (governed by the bulk Richardson number). The present results, on the contrary, provide compelling evidence for a two-layer structure with separate dynamics: whereas no turbulence is present above the interface and the flow accelerates there, the SBL itself decelerates as a result of the surface friction in the non-bursting state. As such, it appears that the mechanism of van de Wiel et al. (2002b) is less realistic. At the same time, our simulation imposes a fixed surface temperature via the boundary condition, whereas, in van de Wiel et al. (2002b) the thermal balance of the surface is an active (dynamic) part of the system, which may allow for additional surface feedbacks not considered here.

Finally, the mechanism found in this study is remarkably close to the conjecture of Businger (1973). Here, we cite parts of his conjecture:

“The point is that if $R_{f_{cr}}$ is reached sometime . . . , it will be reached first where the maximum value occurs at some height above, but relatively close, to the surface. As soon as this happens the turbulence will be dampened and a laminar layer will tend to form. This layer is an effective barrier for all the fluxes. . . . Under the laminar layer the transfer of momentum will continue down to the surface until the available momentum is depleted or R_f has become larger than critical. The result is that the wind diminishes and a period of calm sets in. . . . In the meantime, above the laminar layer momentum is still transferred downward whereas little heat is transferred. Consequently, the momentum increases in the upper part of the laminar layer because it cannot pass through this layer. A strong wind shear builds up and since there is no similar effect for the heat flux, Ri must decrease, eventually reaching a value below Ri_{cr} . This means that the laminar layer will gradually be eaten away by turbulence from above. Eventually the turbulence reaches the ground associated with a burst of momentum and heat. After this, the entire sequence of events may repeat itself.”

However, the key difference is the actor that increases the momentum above the boundary layer during the non-bursting times. Whereas Businger suggested that momentum is transferred downwards from higher up in the flow by stress convergence, the current results indicate momentum is increased by acceleration as a result of the pressure gradient and subsequent rotation by the Coriolis force, which are a rather constant factor in time. Apart from this difference, his conjecture is correct with regard to the origin of the burst, the deceleration in the bulk of the SBL and the possibility of periodicity.

4.5.2 A systematic climatology of bursts?

The present study would largely benefit from a systematic climatology of bursts. Such climatology may clarify under which conditions successive or even periodic bursting events can occur. In our simulations, the external forcings (e.g., the geostrophic wind speed and subsidence profile) are kept constant, and the surface is homogeneous. As a result, the simulation reaches a steady state in which the bursts only marginally affect the background flow allowing a fast recovery and subsequent burst. A strict steady state is not expected to occur in the outdoor environment in which synoptic disturbances occur, but may be approached for several days in the polar regions.

Petenko et al. (2019) show that periods lasting several hours in which the SBL is perturbed by successive wave events, are frequent at the Dome C station (see their Fig. 9). They note that the large-scale weather conditions were stationary during these periods. However, the lack of accurate turbulent flux measurements (e.g., using eddy-covariance techniques) and the limited amount of measurement levels on the meteorological tower prevent the determination of the interactions between the mean flow and the wave events.

Another open question relates to the climatology of the event in relation to external forcings. In contrast to the present study, Petenko et al. (2019) seem to suggest

that intermittency is more likely to occur within SBLs of depth 20–70 m than in very shallow SBLs of depth $z \approx 5$ m. This implies a larger geostrophic forcing (i.e., near-surface large-scale pressure gradient), and/or a weaker subsidence warming as to allow a larger turbulent activity and a deeper SBL. At the same time, however, the timescales of successive event in their study corresponds to the timescale identified in the present study: 8–15 min in theirs as compared to 10 min in the current. Therefore a one-to-one comparison of intermittency climatology with respect to forcings between observations and modelling is essential in order to generalize the present conclusions.

4.6 Conclusions

In this study, a mechanism for periodic shear-generated intermittent bursts is identified using high-resolution LES. This mechanism closely resembles the mechanism proposed by Businger (1973) differing only in the cause of acceleration above the SBL.

Van der Linden et al. (2019) simulate the VSBL based on observations of the Antarctic winter of 2015 from the Dome C station in related work. They show that the temperature flux divergence and heating by subsidence balance over timescales > 1 h such that a steady-state SBL with depth ≈ 5.5 m is reached. Here, we find that the SBL is not in steady state over timescales < 10 min, but is rather modulated by turbulent bursts, which enable the steady state over longer timescales.

Using an extended simulation domain, it is found that periodically wave perturbations form at the interface of a shallow SBL (2.5–2.9 m) and a quasi-laminar layer above (i.e., flow with negligible turbulent activity). The dominant wave is found to grow in time until it breaks resulting in increased turbulent activity and a temporary growth of the active turbulent layer. Spectral analysis shows that the wavelength of this dominant wave is 16–19 m.

A linear stability analysis confirms that small-amplitude waves of this wavelength are indeed unstable with respect to the mean wind and temperature profiles. Furthermore, the predicted perturbation profiles of the velocity components, temperature and fluxes correspond with those obtained by the spectral analysis. The shape of these perturbation profiles are indicative of the Kelvin–Helmholtz instability, which has been found to occur before in stable conditions (see, e.g., de Baas and Driedonks 1985; Newsom and Banta 2003).

The instability is created by an increase of the local shear at the interface that dominates over the increase in temperature gradient resulting in a decrease of Ri_g to a value < 0.25 , which is a prerequisite for instability to occur (see, e.g., Kundu et al. 2012). The interfacial shear is increased as a result of deceleration of the flow in the SBL by turbulent friction, and acceleration above by the combined action of the pressure forcing and the rotation by the Coriolis force. During the burst, these two layers become temporarily coupled and the momentum is exchanged; that is, the lower part accelerates and the higher part decelerates. The instability is mixed away

by its own result and Ri_g becomes > 0.25 at the interface. It is found, however, that the mean wind is only altered slightly by the burst and returns to its pre-burst state. As such, the flow is found to reside around its critical state, and a cyclic process of instability formation and bursting ensues. This is a (modified) Businger mechanism. Businger (1973) correctly proposed such intermittency could be periodic by the process described above with one exception. He stated that the momentum above the SBL is increased due to downward turbulent transfer. However, such transfer is not possible as a result of negligible turbulent activity above the SBL.

The temperature dynamics follow a similar pattern. Prior to the burst, the SBL is cooled by the turbulent flux toward the surface and the quasi-laminar layer is heated by the subsidence heating. During the burst, the cooler air is mixed upward and the warmer air is mixed downward. It is this periodic mixing that explains the thermal steady state over timescales > 1 h reported by van der Linden et al. (2019).

Although intermittent bursts are commonly observed in the SBL at both the mid- and high-latitudes, the exact conditions leading to such bursts, and, in particular, successive (periodic) bursts remain elusive. At the same time, while the steady forcing conditions of the simulation allow periodic bursts to occur and the mechanism to be revealed, these conditions are just one realization of the SBL based on observations from the Antarctic winter. A detailed climatology of shear-generated bursts in relation to the conditions in which they are found (e.g., mean wind or surface characteristics) would therefore be beneficial, and help to predict the timescales and vertical extent of such bursts among other things. Furthermore, realistic high-resolution simulations based on such climatological cases can clarify the contribution of bursts to vertical transfer of momentum and scalars.

4.A Description of the LES case

In the current study, the LES case for the VSBL of van der Linden et al. (2019) is used. Here, we briefly summarize the set-up of their VSBL simulation. A detailed description of the observations, set-up and results can be found in van der Linden et al. (2019). Furthermore, the used, open-source code MicroHH (<http://microhh.org>) is described in van Heerwaarden et al. (2017).

The subfilter-scale flux tensors are modelled by a Smagorinsky–Lilly-type eddy-viscosity model (Lilly 1962; Smagorinsky 1963) in which stratification effects are included (Lilly 1962; Mason 1989). Furthermore, the wall-correction of Mason and Thomson (1992) is used for the length scale of the eddy-viscosity. Surface fluxes are calculated using Monin–Obukhov Similarity Theory with the similarity functions of Högström (1988). Velocity boundary conditions for the horizontal components are no-slip at the surface and stress-free at the top, and no-slip at both surface and top for the vertical velocity. For temperature, Dirichlet conditions are used. Heating of the air by subsidence is calculated as the product of a constant linear subsidence profile (zero at the surface) and the domain averaged temperature gradient. Subsidence of momentum is not included.

Table 4.1: Overview of the simulation set-up as used for the VSBL case in van der Linden et al. (2019).

Parameter description	Symbol	Value
Grid size	Δ [m]	0.08
Grid points	$N_x \times N_y \times N_z$	$240 \times 240 \times 240$
Total run time	t_r [h]	23
Cooling time	t_c [h]	6.25
Geostrophic wind speed (VSBL)	G [m s^{-1}]	3.5
Maximum inversion strength	$\Delta\theta$ [K]	25
Subsidence velocity at 100 m	w_s [m s^{-1}]	-4×10^{-3}
Roughness length for momentum	$z_{0,m}$ [m]	1×10^{-3}
Roughness length for heat	$z_{0,h}$ [m]	1×10^{-4}
Reference temperature	θ_0 [K]	235
Coriolis parameter	f_C [s^{-1}]	1.39×10^{-4}
Acceleration due to gravity	g [m s^{-2}]	9.81
von Kármán constant	κ	0.4
Smagorinsky constant	c_s	0.12
Turbulent Prandtl number	Pr_t	1

Simulations are initialised with constant temperature θ_0 and constant velocity $(G, 0, 0)$ in the x -, y - and z -directions, respectively. At the start of the simulation, the surface is cooled by 25 K after which cooling is stopped, and the simulation is continued to reach steady state. An overview of the parameters used in the VSBL case is given in Table 4.1.

4.B Derivation of the LSA

We consider the conservation equation of mass, the inviscid Navier–Stokes equation and the conservation equation of energy (written in temperature form) under the Boussinesq approximation in 2D

$$\partial_i u_i = 0, \quad (4.3a)$$

$$\partial_i u_i = -u_j \partial_j u_i + \frac{g}{\theta_0} (\theta - \theta_0) \delta_{i3} - \partial_i p, \quad (4.3b)$$

$$\partial_t \theta = -u_j \partial_j \theta, \quad (4.3c)$$

where u_i are the velocity components in the x - and z -direction, θ is the potential temperature, θ_0 is the reference temperature, g is the acceleration due to gravity and p is the modified pressure.

We assume that our variables can be decomposed into their mean background states and a contribution due to perturbations indicated by a capital letter and a

prime, respectively,

$$u(x, z, t) = U(z) + u', \quad (4.4a)$$

$$w(x, z, t) = w', \quad (4.4b)$$

$$\theta(x, z, t) = \Theta(z) + \theta', \quad (4.4c)$$

$$p(x, z, t) = p'. \quad (4.4d)$$

These expressions are inserted into Eq. 4.3 and subsequently the mean state balance is subtracted. Additionally, products of perturbed quantities are assumed to be negligibly small and therefore removed. This results in a new set of *linearized* equations for the perturbed variables

$$\partial_x u' + \partial_z w' = 0, \quad (4.5a)$$

$$\partial_t u' = -U(z)\partial_x u' - w' \frac{dU}{dz} - \partial_x p, \quad (4.5b)$$

$$\partial_t w' = -U(z)\partial_x w' + \frac{g}{\theta_0} \theta' - \partial_z p, \quad (4.5c)$$

$$\partial_t \theta' = -U(z)\partial_x \theta' - w' \frac{d\Theta}{dz}. \quad (4.5d)$$

By taking the derivatives of Eq. 4.5b and 4.5c with respect to x and z , respectively, adding them and applying Eq. 4.5a, a Poisson equation for the pressure is obtained

$$\nabla^2 p' = -2\partial_x w' \frac{dU}{dz} + \frac{g}{\theta_0} \partial_z \theta'. \quad (4.6)$$

Subsequently, by taking the Laplacian (∇^2) of Eq. 4.5c and the z -derivative of Eq. 4.6, the pressure is eliminated. This results in a reduced set of equations for the vertical velocity perturbation and the temperature

$$\partial_t \nabla^2 w' = -U(z)\partial_x \nabla^2 w' + \frac{d^2 U}{dz^2} \partial_x w' + \frac{g}{\theta_0} \partial_{xx} \theta', \quad (4.7a)$$

$$\partial_t \theta' = -U(z)\partial_x \theta' - w' \frac{d\Theta}{dz}. \quad (4.7b)$$

Next, travelling-wave solutions (complex Fourier components) are taken as Ansatz, for example, for the vertical velocity (perturbation)

$$w' = \sum_k w'_k = \text{Re} \left(\sum_k \hat{w}_k(z) e^{ik(x-c_k t)} \right) = \text{Re} \left(\sum_k \hat{w}_k(z) e^{ikx} e^{\sigma_k t} \right), \quad (4.8)$$

where k is the real wavenumber, $\hat{w}_k(z)$ is the complex amplitude (profile) of the k th mode, $c_k = c_{k,R} + ic_{k,I}$ is the phase speed, and $\sigma_k = -ikc_k$ is the growth rate. A positive value of $\text{Re}(\sigma_k)$ (or $c_{k,I}$) results in a growing wave mode in time indicating instability. Substitution of this Ansatz and cancellation of the exponentials leads to

(for each wave mode separately)

$$\sigma_k \left(\frac{d^2}{dz^2} - k^2 \right) \hat{w}_k = -ikU(z) \left(\frac{d^2}{dz^2} - k^2 \right) \hat{w}_k + ik \frac{d^2 U}{dz^2} \hat{w}_k - \frac{g}{\theta_0} k^2 \hat{\theta}_k, \quad (4.9a)$$

$$\sigma_k \hat{\theta}_k = -ikU(z) \hat{\theta}_k - \frac{d\Theta}{dz} \hat{w}_k. \quad (4.9b)$$

This set of equations is to be numerically solved for the unknown growth rate σ_k , and the corresponding profiles of the vertical velocity and temperature perturbations. To do this, a finite-difference approximation is used in which the amplitude profiles are discretized in N_z vertical levels (i.e., $\hat{w}_k(z)$ is discretized as the vector $\hat{\mathbf{w}}_k$ of finite length N_z). This transforms Eq. 4.7 into a generalized eigenvalue problem with eigenvalue σ_k and eigenvector $[\hat{\mathbf{w}}_k, \hat{\theta}_k]^T$

$$\sigma_k \begin{bmatrix} \mathbf{A} & \mathbf{0} \\ \mathbf{0} & \mathbf{I} \end{bmatrix} \begin{bmatrix} \hat{\mathbf{w}}_k \\ \hat{\theta}_k \end{bmatrix} = \begin{bmatrix} \mathbf{B}_{11} & \mathbf{B}_{12} \\ \mathbf{B}_{21} & \mathbf{B}_{22} \end{bmatrix} \begin{bmatrix} \hat{\mathbf{w}}_k \\ \hat{\theta}_k \end{bmatrix} \quad (4.10)$$

in which the \mathbf{A} , \mathbf{B}_{11} , \mathbf{B}_{12} , \mathbf{B}_{21} and \mathbf{B}_{22} are block matrices of size $N_z \times N_z$ with N_z being the amount of vertical levels. These block matrices are given by

$$\mathbf{A} = \mathbf{D}^2 - k^2 \mathbf{I}, \quad (4.11a)$$

$$\mathbf{B}_{11} = -ik\mathbf{U}^T \mathbf{A} + ik(\mathbf{U}_{zz})^T \mathbf{I}, \quad (4.11b)$$

$$\mathbf{B}_{12} = -\frac{g}{\theta_0} k^2 \mathbf{I}, \quad (4.11c)$$

$$\mathbf{B}_{21} = -\mathbf{T}_{zz}^T \mathbf{I}, \quad (4.11d)$$

$$\mathbf{B}_{22} = -ik\mathbf{U}^T \mathbf{I}, \quad (4.11e)$$

where \mathbf{D}^2 is the matrix for the finite-difference second derivatives, \mathbf{I} is the identity matrix, and \mathbf{U} , \mathbf{U}_{zz} and \mathbf{T}_{zz} are column vectors (size $N_z \times 1$) of the discretized background velocity magnitude, second derivative of the velocity magnitude and the second derivative of the temperature, respectively. Note that, \mathbf{B}_{12} , \mathbf{B}_{21} and \mathbf{B}_{22} are diagonal matrices. The second derivatives are calculated by using a second-order central difference scheme.

For the configuration in this study, the boundary conditions are $\hat{w}_k = 0$ at $z = 0$ and $\frac{d\hat{w}_k}{dz} = -k\hat{w}_k$ at $z = L_z$ (top of the computational domain). The latter is an approximation for $\hat{w}_k \rightarrow 0$ as $z \rightarrow \infty$ (see, e.g., Newsom and Banta 2003). These boundary conditions for \hat{w}_k and its first derivative are imposed through modification of \mathbf{D}^2 . The first boundary condition does not require a change of \mathbf{D}^2 . The second is implemented by alteration of the trace element and sub-trace element: $D^2(N_z, N_z) = (-2 - 2\Delta_z k)/\Delta_z^2$ and $D^2(N_z - 1, N_z) = 2/\Delta_z^2$.

5

Conclusions and perspectives

In this chapter, a number of concluding remarks and answers to the research objectives and questions, as outlined in chapter 1, are presented. These are followed by some perspectives on current challenges and future research possibilities.

5.1 Conclusions

The behavior of both the (Dutch) short-lived and the (Antarctic) long-lived stable boundary layer has been investigated in response to the large-scale horizontal pressure gradient. This pressure gradient, which is often expressed as the geostrophic wind speed, is found to be a dominant external parameter that determines the overall structure of the short-lived and the long-lived SBL (under clear skies). In this dissertation, observational analysis of the short-lived SBL (Cabauw, the Netherlands) and the long-lived SBL (Concordia station, Dome C, Antarctica), and large-eddy simulations of the long-lived SBL have been combined. An approach of progressively ‘zooming in’ on well-defined SBLs has been followed. To this end, three sets of research questions have been formulated, which form the basis of chapters 2–4. Here, the key points and main answers to those research questions are briefly summarized.

In chapter 2, an analysis of eleven years of observations from the meteorological tower at Cabauw, the Netherlands, in combination with near-surface pressure-gradient data shows that **the mean dynamical response of the stable boundary layer as a function of the large-scale horizontal pressure gradient is gradual**. Diagnosed variables, such as, the turbulent surface fluxes, are systematically ordered in which high geostrophic wind speeds result in large fluxes and low geostrophic wind speeds in small fluxes. As a result, the transition from the weakly stable regime to the very stable regime is also gradual for decreasing geostrophic wind speed, which is in contrast to the abrupt transition found in classifications using local, in-situ wind speeds or predictions by conceptual models. At the same time, the ‘classical’ weakly

and very stable regimes are obtained for high and low geostrophic wind speeds. Evidence is found that in the transition region with moderate geostrophic wind speeds, turbulent properties show bimodal probability distributions. This means that a mix of the WSBL and VSBL is found in this transition region in which the outcome depends on subtleties within a specific night. **Therefore, taking the geostrophic wind speed as a sole marker for the to separate the WSBL and the VSBL appears to be insufficient.** In part, this is caused by additional external parameters, which are not taken into account. Such additional parameters may include, for example, soil and atmospheric moisture, advection, and variable cloud cover. Additionally, a clear separation may be prevented by global intermittency which would cause the turbulent activity within the SBL to vary within a night.

Moving from the mid-latitudes to the polar regions, long-lived stable boundary layers are found that remain stably stratified for months. The SBL may truly reach a (thermal) steady state under steady external forcing conditions (see chapter 3). This is contrast to the quasi-steady state often encounter at the mid-latitudes. In this sense, polar SBL cases are well-defined and encourage the use of high-resolution turbulence modelling such as LES. At the same time, the observations show that the SBL can transition from the weakly stable to the very stable regime and back again, when those external conditions change.

Two actually observed cases, representative for the WSBL and VSBL conditions at Dome C, have been used to set up two reality-inspired LES cases, which only differ in the imposed geostrophic wind speed. A good correspondence is found between the simulated wind-speed profiles and the observed wind speeds for both cases. Likewise, the simulated and observed wind-direction and temperature profiles are in reasonable agreement. Minor differences in the shape of the observed and simulated temperature profile are found, which may be attributed to the lack of radiative transfer in the LES, although the subsidence parametrization could also be of influence. **Therefore, it is shown that the LES approach can accurately represent the observed polar SBL to a large extent, when using sub-metre scale resolutions (~ 0.1 m).** In particular under very stable conditions, when the SBL can be as shallow as ≈ 5.5 m, high resolutions are required near the surface. **The LES cases confirm that the difference in those two states is dominantly caused by the difference in its imposed geostrophic wind speed.**

Although the LES shows that the VSBL is in steady state over timescales > 1 h (e.g., turbulent cooling and heating by subsidence are balanced), systematic intermittent turbulence is found over timescales < 15 min. To explore this interesting phenomenon, the LES results of the VSBL case have been further analyzed in detail in the last part of this dissertation (chapter 4).

A combination of analysis of the simulation cross sections and a linear stability analysis shows that **the intermittent turbulence is triggered by the Kelvin-Helmholtz instability at the top of a shallow SBL (2.5–2.9 m), where the local shear is large.** Small wave-like perturbations are amplified by this instability and grow in time until they break by overturning. During the resulting burst, the turbulent layer temporarily increases in height and the shallow SBL temporarily becomes

coupled to the quasi-laminar layer above. The associated vertical exchange removes the underlying cause of the instability itself as the shear is mixed away. The mean wind and temperature profiles, however, are only slightly changed by the burst. After the burst, the enhanced turbulent activity has been dissipated and the shallow SBL again becomes decoupled from the layer above. Now, the shear is allowed to be restored and becomes large enough for the Kelvin–Helmholtz instability to occur again. In contrast to the conjecture of Businger (1973), the restoration of the shear is not achieved by momentum convergence in the upper layer, but by the combination of the rotation due to the Coriolis force and the pressure forcing. **Therefore, the full mechanism for periodic bursting of the shallow SBL is referred to as a (modified) Businger mechanism** (chapter 4).

5.2 Perspectives

Both the analyses of the Dutch short-lived SBL and the Antarctic long-lived SBL at Antarctica, show that, apart from the pressure gradient (mechanical forcing), other processes, such as, radiative transfer and heat transfer through the underlying surface (e.g., grass, ice or snow) play a role. The climatology of the short-lived SBL in chapter 2 has been restricted to clear-sky SBLs (based on a net radiation threshold) as to extract the influence of the pressure gradient. However, it is known that (variable) cloud cover may crucially effect the energy budget at the surface by modification of the incoming longwave radiation, which in turn alters the cooling and buildup of the stratification. Monahan et al. (2015) included the observed cloud cover at Cabauw (as a proxy of the incoming radiation) in their analysis and showed that, for example, the SBL becomes weakly stable when the cloud cover is high, even under low geostrophic wind speeds. Radiative transfer also directly impacts the shape of the temperature profiles. This aspect emerges from the comparison of the observations and simulations of the long-lived SBL in which the observed profile in the VSBL is exponentially-shaped, whereas the simulated profile is more linear with height (chapter 3).

Similarly, the dynamical interaction with the underlying surface deserves in-depth attention in follow-up studies. The relative importance of the heat transfer with the underlying surface becomes increasingly relevant with decreasing turbulence (Bosveld et al. 2014; van de Wiel et al. 2017). In fact, under (very) low geostrophic wind speeds, the supply of heat from below may prevent excessive surface cooling (see chapter 2). Nevertheless, for simplicity, often a prescribed (evolution of the) temperature or temperature flux is used as a bottom boundary condition in high-resolution turbulence models. Therefore, a logical extension of the current work would be the extension of the observational climatology with these processes and the inclusion of these within the LES model.

In relation to this, one of the large challenges of the SBL is surface heterogeneity (at a local scale) in otherwise relatively flat topography. The local surface surrounding a typical measurement site is often (implicitly) assumed to be homogeneous or taken as such for convenience. However, this assumption is an oversimplification



Figure 5.1: Landscape surrounding the main meteorological tower at the Cabauw site in the Netherlands. The small village to the North of the main site and the ditches are clearly visible.

even on the scale of merely a few hectares. Figure 5.1 shows (part of) the surface surrounding the meteorological tower at the Cabauw site in the Netherlands as an example. Although the local terrain is characterized by open pastures for at least 400 m around the tower and the overall topography is relatively flat (van Ulden and Wieringa 1996), ditches of different lengths and widths are interspersed throughout the field. These ditches do not only result in changes of surface cover, but also in slight changes in topography. The higher heat capacity of the water also effects the local surface temperature compared to that of the grass. Such variability at the microscale (< 1 km) in elevation or surface characteristics is not uncommon. As a result, microscale circulations and the lateral transfer of mass and heat as a result of small-scale convective motion and ‘sinking’ of colder air (i.e., drainage flows and the formation of cold pools) may occur, and significantly alter the near-surface structure of the SBL. These may become relatively important—in particular—for (very) low geostrophic wind speeds in which the SBL is expected to be very stable (Mahrt and Vickers 2006). However, open questions are how the turbulent fluxes vary in the horizontal over such surfaces, and how these aggregate on a larger scale as to obtain a representative flux. These are relevant for both numerical weather prediction models and high-resolution turbulence resolving models. Additionally, such variability can have effects at a seasonal scale by, for example, inducing horizontal gradients in the soil humidity.

Much insight is to be gained into the effects of surface heterogeneity in the near future by the combination of novel, high-resolution observational techniques and advances in LES modeling with realistic land-surface coupling. For example, the distributed temperature sensing (DTS) technique enables the measurement of the temperature at high temporal and spatial frequencies (≈ 0.5 Hz, 0.25 m) down to the surface (Thomas et al. 2012; Zeeman et al. 2015; Izett et al. 2019). The setup of DTS in a 3D grid makes the variation in the near-surface temperature structure visible, and the identification of small-scale motion possible (Zeeman et al. 2015). Additionally, infrared thermal cameras can measure the effects of the heterogeneity on the radia-

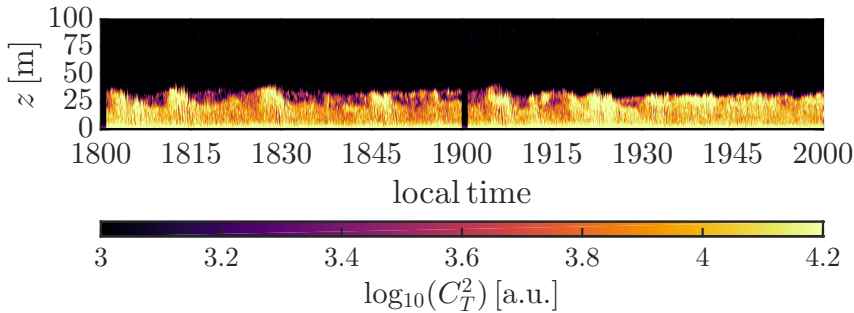


Figure 5.2: Sodar echogram during 25 August 2012 starting at 1800 LT. Adapted from Petenko et al. (2019).

tive surface temperature itself, whereas LIDAR can be used to gain information on the spatial velocity field using the Doppler effect (see, e.g., Newsom and Banta 2003) or to map the small-scale topography. Although still challenging, high-resolution LES models can be used to gain full 3D information on the flow and temperature fields provided they are coupled to an interactive surface, radiative transfer and/or moisture model, and are validated against the observations (viz., they correspond to each other in a statistical sense). Such validated models may even benefit from acceleration on graphical processing units and become faster-than-real-time (Schalkwijk et al. 2015), or from adaptive mesh refinement techniques in which the numerical grid is refined (statically or dynamically) in the region of interest (van Hooft et al. 2018).

A second challenge remains the study of intermittent turbulence within the SBL. Although a mechanism for periodic top-down intermittent bursting has been identified in this dissertation (chapter 4), a number of remaining open questions are still present. First, it is unknown which conditions are favorable for this periodic bursting to occur. Petenko et al. (2019) show that such periodic bursting occurred frequently during the polar winter of 2012 at the Dome C station, and that it seems to correlate with stationary large-scale weather conditions for several days. However, a more systematic climatology covering either different observational locations or periods is needed to answer this question. Second, Petenko et al. (2019) observe that periodic bursting appears to mainly occur in SBLs of depth 20–70 m (see Fig. 5.2), whereas in the simulations the bursts also occur in a very shallow SBL (≈ 5 m). A deeper SBL implies a larger geostrophic forcing, a weaker thermal inversion and/or weaker heating by subsidence. The timescale (period) between successive bursts is, however, approximately equal.

In addition, intermittency itself is commonly observed and documented in literature, and multiple triggers for it have been identified, which can be divided in

external (e.g., by submeso motions) and internal (viz., caused by an interplay of the turbulence and mean flow) (Mahrt 2014). However, a systematic and comprehensive overview of intermittency in both observations and simulations; its prevalence; its effects and interaction with the mean flow; and the necessary or preferable conditions in which it occurs, remains elusive. It is speculated that intermittent bursts are responsible for “significant portions” of the vertical exchange of momentum, heat and other scalars (Nappo 1991). A comprehensive overview or climatology of intermittency will be beneficial in quantifying this contribution to vertical mixing and its interaction with the mean flow. Such in-depth process studies as, for example, described in this dissertation (chapter 2), will help to improve predictions of the near-surface structure of the SBL in the polar climate.

Bibliography

- Abkar, M., and P. Moin, 2017: Large-Eddy Simulation of Thermally Stratified Atmospheric Boundary-Layer Flow Using a Minimum Dissipation Model. *Bound.-Layer Meteor.*, **165** (3), 405–419, doi:10.1007/s10546-017-0288-4.
- Acevedo, O. C., and D. R. Fitzjarrald, 2003: In the Core of the Night-Effects of Intermittent Mixing on a Horizontally Heterogeneous Surface. *Bound.-Layer Meteor.*, **106** (1), 1–33, doi:10.1023/A:1020824109575.
- Acevedo, O. C., L. Mahrt, F. S. Puhales, F. D. Costa, L. E. Medeiros, and G. A. Degrazia, 2016: Contrasting structures between the decoupled and coupled states of the stable boundary layer. *Quart. J. Roy. Meteor. Soc.*, **142** (695), 693–702, doi:10.1002/qj.2693.
- André, J. C., and L. Mahrt, 1982: The Nocturnal Surface Inversion and Influence of Clear-Air Radiative Cooling. *J. Atmos. Sci.*, **39** (4), 864–878, doi:10.1175/1520-0469(1982)039<0864:TNSIAI>2.0.CO;2.
- Andreas, E. L., 2012: Two Experiments on Using a Scintillometer to Infer the Surface Fluxes of Momentum and Sensible Heat. *J. Appl. Meteor. Climatol.*, **51** (9), 1685–1701, doi:10.1175/JAMC-D-11-0248.1.
- Ansorge, C., and J. P. Mellado, 2014: Global Intermittency and Collapsing Turbulence in the Stratified Planetary Boundary Layer. *Bound.-Layer Meteor.*, **153** (1), 89–116, doi:10.1007/s10546-014-9941-3.
- Argentini, S., I. V. Petenko, G. Mastrantonio, V. A. Bezverkhni, and A. P. Viola, 2001: Spectral characteristics of East Antarctica meteorological parameters during 1994. *J. Geophys. Res. Atmos.*, **106** (D12), 12 463–12 476, doi:10.1029/2001JD900112.
- Aristidi, E., and Coauthors, 2005: An analysis of temperatures and wind speeds above Dome C, Antarctica. *Astronomy & Astrophysics*, **430** (2), 739–746, doi:10.1051/0004-6361:20041876.
- Baas, P., F. C. Bosveld, H. Klein Baltink, and A. A. M. Holtslag, 2009: A Climatology of Nocturnal Low-Level Jets at Cabauw. *J. Appl. Meteor. Climatol.*, **48** (8), 1627–1642, doi:10.1175/2009JAMC1965.1.
- Baas, P., B. J. H. van de Wiel, L. van den Brink, and A. Holtslag, 2012: Composite hodographs and inertial oscillations in the nocturnal boundary layer. *Quart. J. Roy. Meteor. Soc.*, **138** (663), 528–535, doi:10.1002/qj.941.
- Baas, P., B. J. H. van de Wiel, E. van Meijgaard, E. Vignon, C. Genthon, S. J. A. van der Linden, and S. R. de Roode, 2019: Transitions in the wintertime near-surface temperature inversion at Dome C, Antarctica. *Quart. J. Roy. Meteor. Soc.*, **145** (720), 930–946, doi:10.1002/qj.3450.
- Babić, K., Z. Bencetić, and Željko Večenaj, 2012: Determining a turbulence averaging time scale by Fourier analysis for the nocturnal boundary layer. *Geofizika*, **29**, 35–51.
- Balsley, B. B., R. G. Frehlich, M. L. Jensen, Y. Meillier, and A. Muschinski, 2003: Extreme Gradients in the Nocturnal Boundary Layer: Structure, Evolution, and Potential Causes. *J. Atmos. Sci.*, **60** (20), 2496–2508, doi:10.1175/1520-0469(2003)060<2496:EGITNB>2.0.CO;2.
- Banta, R. M., Y. L. Pichugina, and W. A. Brewer, 2006: Turbulent Velocity-Variance Profiles in the Stable Boundary Layer Generated by a Nocturnal Low-Level Jet. *J. Atmos. Sci.*, **63** (11), 2700–2719, doi:10.1175/JAS3776.1.
- Basu, S., and F. Porté-Agel, 2006: Large-Eddy Simulation of Stably Stratified Atmospheric Boundary Layer Turbulence: A Scale-Dependent Dynamic Modeling Approach. *J. Atmos. Sci.*, **63** (8), 2074–2091, doi:10.1175/JAS3734.1.
- Bazile, E., F. Couvreux, P. L. Moigne, C. Genthon, A. A. M. Holtslag, and G. Svensson, 2014: GABLS4: An intercomparison case to study the stable boundary layer over the Antarctic plateau. *Global Energy and Water Cycle Exchange News*, **24** (4), 4.

- Beare, R. J., and Coauthors, 2006: An Intercomparison of Large-Eddy Simulations of the Stable Boundary Layer. *Bound.-Layer Meteor.*, **118** (2), 247–272, doi:10.1007/s10546-004-2820-6.
- Blumen, W., R. Banta, S. P. Burns, D. C. Fritts, R. Newsom, G. S. Poulos, and J. Sun, 2001: Turbulent statistics of a Kelvin–Helmholtz billow event observed in the night-time boundary layer during the Cooperative Atmosphere–Surface Exchange Study field program. *Dyn. Atmos. Oceans*, **34**, 189–204, doi:10.1016/S0377-0265(01)00067-7.
- Bosveld, F. C., 2016: Cabauw In-situ Observational Program 2000 - Now: Instruments, Calibrations and Set-up. [Available online at http://projects.knmi.nl/cabauw/insitu/observations/documentation/Cabauw_TR/Cabauw_TR.pdf].
- Bosveld, F. C., P. Baas, E. van Meijgaard, E. I. F. de Bruijn, G.-J. Steeneveld, and A. A. M. Holtslag, 2014: The Third GABLS Intercomparison Case for Evaluation Studies of Boundary-Layer Models. Part A: Case Selection and Set-Up. *Bound.-Layer Meteor.*, **152** (2), 133–156, doi:10.1007/s10546-014-9917-3.
- Bosveld, F. C., and F. Beyrich, 2004: Classifying observations of stable boundary layers for model validation. *Proc. 16th Symposium on Boundary Layers and Turbulence*, American Meteorological Society, P4.13, [Available online at <https://ams.confex.com/ams/pdfpapers/78641.pdf>].
- Botev, Z. I., J. F. Grotowski, and D. P. Kroese, 2010: Kernel density estimation via diffusion. *Ann. Statist.*, **38** (5), 2916–2957, doi:10.1214/10-AOS799.
- Bou-Zeid, E., C. Higgins, H. Huwald, C. Meneveau, and M. B. Parlange, 2010: Field study of the dynamics and modelling of subgrid-scale turbulence in a stable atmospheric surface layer over a glacier. *J. Fluid Mech.*, **665**, 480–515, doi:10.1017/S0022112010004015.
- Bou-Zeid, E., C. Meneveau, and M. Parlange, 2005: A scale-dependent lagrangian dynamic model for large eddy simulation of complex turbulent flows. *Phys. Fluids*, **17** (2), 025 105, doi:10.1063/1.1839152.
- Brunt, D., 1934: *Physical and Dynamic Meteorology*. Cambridge University Press, 454 pp.
- Businger, J. C., 1973: Turbulent Transfer in the Atmospheric Surface Layer. *Workshop on Micrometeorology*, D. A. Haugen, Ed., Amer. Meteor. Soc., 67–100.
- Cerni, T. A., and T. R. Parish, 1984: A Radiative Model of the Stable Nocturnal Boundary Layer with Application to the Polar Night. *J. Climate Appl. Meteor.*, **23** (11), 1563–1572, doi:10.1175/1520-0450(1984)023<1563:ARMOTS>2.0.CO;2.
- Chimonas, G., and C. J. Nappo, 1989: Wave drag in the planetary boundary layer over complex terrain. *Bound.-Layer Meteor.*, **47** (1), 217–232, doi:10.1007/BF00122330.
- Chung, D., and G. Matheou, 2014: Large-Eddy Simulation of Stratified Turbulence. Part I: A Vortex-Based Subgrid-Scale Model. *J. Atmos. Sci.*, **71** (5), 1863–1879, doi:10.1175/JAS-D-13-0126.1.
- Connolley, W. M., 1996: The Antarctic Temperature Inversion. *Int. J. Climatol.*, **16** (12), 1333–1342, doi:10.1002/(SICI)1097-0088(199612)16:12<1333::AID-JOC96>3.0.CO;2-6.
- Costa, F. D., O. C. Acevedo, J. C. M. Mombach, and G. A. Degrazia, 2011: A Simplified Model for Intermittent Turbulence in the Nocturnal Boundary Layer. *J. Atmos. Sci.*, **68** (8), 1714–1729, doi:10.1175/2011JAS3655.1.
- Coulter, R. L., 1990: A case study of turbulence in the stable nocturnal boundary layer. *Bound.-Layer Meteor.*, **52** (1), 75–91, doi:10.1007/BF00123179.
- Cuxart, J., and Coauthors, 2006: Single-Column Model Intercomparison for a Stably Stratified Atmospheric Boundary Layer. *Bound.-Layer Meteor.*, **118** (2), 273–303, doi:10.1007/s10546-005-3780-1.
- de Baas, A. F., and A. G. M. Driedonks, 1985: Internal gravity waves in a stably stratified boundary layer. *Bound.-Layer Meteor.*, **31** (3), 303–323, doi:10.1007/BF00120898.
- de Bruin, H. A. R., W. M. L. Meijninger, A.-S. Smedman, and M. Magnusson, 2002: Displaced-Beam Small Aperture Scintillometer Test. Part I: The Wintex Data-Set. *Bound.-Layer Meteor.*, **105** (1), 129–148, doi:10.1023/A:1019639631711.
- de Roode, S. R., F. C. Bosveld, and P. S. Kroon, 2010: Dew Formation, Eddy-Correlation Latent Heat Fluxes, and the Surface Energy Imbalance at Cabauw During Stable Conditions. *Bound.-Layer Meteor.*, **135** (3), 369–383, doi:10.1007/s10546-010-9476-1.
- de Roode, S. R., H. J. J. Jonker, B. J. H. van de Wiel, V. Vertregt, and V. Perrin, 2017: A Diagnosis of Excessive Mixing in Smagorinsky Subfilter-Scale Turbulent Kinetic Energy Models. *J. Atmos. Sci.*, **74** (5), 1495–1511, doi:10.1175/JAS-D-16-0212.1.

- Deardorff, J. W., 1980: Stratocumulus-capped mixed layers derived from a three-dimensional model. *Bound.-Layer Meteor.*, **18** (4), 495–527, doi:10.1007/BF00119502.
- Derbyshire, S. H., 1990: Nieuwstadt's stable boundary layer revisited. *Quart. J. Roy. Meteor. Soc.*, **116** (491), 127–158, doi:10.1002/qj.49711649106.
- Derbyshire, S. H., 1999: Stable Boundary-Layer Modelling: Established Approaches and Beyond. *Bound.-Layer Meteor.*, **90** (3), 423–446, doi:10.1023/A:1001749007836.
- Dias-Júnior, C. Q., L. D. Sá, E. P. Marques Filho, R. A. Santana, M. Mauder, and A. O. Manzi, 2017: Turbulence regimes in the stable boundary layer above and within the amazon forest. *Agric. For. Meteor.*, **233**, 122–132, doi:10.1016/j.agrformet.2016.11.001.
- Donda, J. M. M., B. J. H. van de Wiel, F. C. Bosveld, F. Beyrich, G. J. F. van Heijst, and H. J. H. Clercx, 2013: Predicting Nocturnal Wind and Temperature Profiles Based on External Forcing Parameters. *Bound.-Layer Meteor.*, **146** (1), 103–117, doi:10.1007/s10546-012-9755-0.
- Donda, J. M. M., I. G. S. van Hooijdonk, A. F. Moene, H. J. J. Jonker, G. J. F. van Heijst, H. J. H. Clercx, and B. J. H. van de Wiel, 2015: Collapse of turbulence in stably stratified channel flow: a transient phenomenon. *Quart. J. Roy. Meteor. Soc.*, **141** (691), 2137–2147, doi:10.1002/qj.2511.
- Drazin, P. G., and W. H. Reid, 2004: *Hydrodynamic Stability*. 2nd ed., Cambridge Mathematical Library, Cambridge University Press, 628 pp., doi:10.1017/CBO9780511616938.
- Duynkerke, P. G., 1999: Turbulence, Radiation and Fog in Dutch Stable Boundary Layers. *Bound.-Layer Meteor.*, **90** (3), 447–477, doi:10.1023/A:1026441904734.
- Edwards, J. M., 2009: Radiative Processes in the Stable Boundary Layer: Part II. The Development of the Nocturnal Boundary Layer. *Bound.-Layer Meteor.*, **131** (2), 127–146, doi:10.1007/s10546-009-9363-9.
- Edwards, J. M., S. Basu, F. C. Bosveld, and A. A. M. Holtslag, 2014: The Impact of Radiation on the GABLS3 Large-Eddy Simulation through the Night and during the Morning Transition. *Bound.-Layer Meteor.*, **152** (2), 189–211, doi:10.1007/s10546-013-9895-x.
- Estournel, C., and D. Guedalia, 1985: Influence of Geostrophic Wind on Atmospheric Nocturnal Cooling. *J. Atmos. Sci.*, **42** (23), 2695–2698, doi:10.1175/1520-0469(1985)042<2695:IOGWOA>2.0.CO;2.
- Fabbian, D., R. de Dear, and S. Lelley, 2007: Application of Artificial Neural Network Forecasts to Predict Fog at Canberra International Airport. *Wea. Forecasting*, **22** (2), 372–381, doi:10.1175/WAF980.1.
- Fernando, H. J. S., and J. C. Weil, 2010: Whither the Stable Boundary Layer? *Bull. Amer. Meteor. Soc.*, **91** (11), 1475–1484, doi:10.1175/2010BAMS2770.1.
- Finnigan, J. J., F. Einaudi, and D. Fua, 1984: The Interaction between an Internal Gravity Wave and Turbulence in the Stably-Stratified Nocturnal Boundary Layer. *J. Atmos. Sci.*, **41** (16), 2409–2436, doi:10.1175/1520-0469(1984)041<2409:TIBAIG>2.0.CO;2.
- Gallée, H., H. Barral, E. Vignon, and C. Genthon, 2015: A case study of a low-level jet during OPALE. *Atmos. Chem. Phys.*, **15** (11), 6237–6246, doi:10.5194/acp-15-6237-2015.
- Gallée, H., and I. V. Gorodetskaya, 2010: Validation of a limited area model over Dome C, Antarctic Plateau, during winter. *Climate Dyn.*, **34** (1), 61–72, doi:10.1007/s00382-008-0499-y.
- Galmarini, S., C. Beets, P. G. Duynkerke, and J. Vilà-Guerau de Arellano, 1998: Stable Nocturnal Boundary Layers: A Comparison of One-Dimensional and Large-Eddy Simulation Models. *Bound.-Layer Meteor.*, **88** (2), 181–210, doi:10.1023/A:1001158702252.
- Garratt, J. R., and R. A. Brost, 1981: Radiative Cooling Effects within and above the Nocturnal Boundary Layer. *J. Atmos. Sci.*, **38** (12), 2730–2746, doi:10.1175/1520-0469(1981)038<2730:RCEWAA>2.0.CO;2.
- Genthon, C., D. Six, H. Gallée, P. Grigioni, and A. Pellegrini, 2013: Two years of atmospheric boundary layer observations on a 45-m tower at Dome C on the Antarctic plateau. *J. Geophys. Res. Atmos.*, **118** (8), 3218–3232, doi:10.1002/jgrd.50128.
- Genthon, C., D. Six, C. Scarchilli, V. Ciardini, and M. Frezzotti, 2016: Meteorological and snow accumulation gradients across Dome C, East Antarctic plateau. *Int. J. Climatol.*, **36** (1), 455–466, doi:10.1002/joc.4362.
- Genthon, C., M. S. Town, D. Six, V. Favier, S. Argentini, and A. Pellegrini, 2010: Meteorological atmospheric boundary layer measurements and ECMWF analyses during summer at Dome C, Antarctica. *J. Geophys. Res. Atmos.*, **115** (D5), doi:10.1029/2009JD012741.

- Gentine, P., G.-J. Steeneveld, B. G. Heusinkveld, and A. A. M. Holtslag, 2018: Coupling between radiative flux divergence and turbulence near the surface. *Quart. J. Roy. Meteor. Soc.*, **144** (717), 2491–2507, doi:10.1002/qj.3333.
- Germano, M., U. Piomelli, P. Moin, and W. H. Cabot, 1991: A dynamic subgrid-scale eddy viscosity model. *Phys. Fluids A: Fluid Dyn.*, **3** (7), 1760–1765, doi:10.1063/1.857955.
- Gossard, E. E., J. H. Richter, and D. Atlas, 1970: Internal waves in the atmosphere from high-resolution radar measurements. *J. Geophys. Res.*, **75** (18), 3523–3536, doi:10.1029/JC075i018p03523.
- Grachev, A. A., C. W. Fairall, P. O. G. Persson, E. L. Andreas, and P. S. Guest, 2005: Stable Boundary-Layer Scaling Regimes: The SHEBA Data. *Bound.-Layer Meteor.*, **116** (2), 201–235, doi:10.1007/s10546-004-2729-0.
- Hartogensis, O. K., H. A. R. de Bruin, and B. J. H. van de Wiel, 2002: Displaced-Beam Small Aperture Scintillometer Test. Part II: CASES-99 Stable Boundary-Layer Experiment. *Bound.-Layer Meteor.*, **105** (1), 149–176, doi:10.1023/A:1019620515781.
- He, P., and S. Basu, 2015: Direct numerical simulation of intermittent turbulence under stably stratified conditions. *Nonlinear Proc. Geophys.*, **22** (4), 447–471, doi:10.5194/npg-22-447-2015.
- He, Y., A. H. Monahan, and N. A. McFarlane, 2013: Diurnal variations of land surface wind speed probability distributions under clear-sky and low-cloud conditions. *Geophys. Res. Lett.*, **40** (12), 3308–3314, doi:10.1002/grl.50575.
- Högström, U., 1988: Non-dimensional wind and temperature profiles in the atmospheric surface layer: A re-evaluation. *Bound.-Layer Meteor.*, **42** (1), 55–78, doi:10.1007/BF00119875.
- Holtslag, A. A. M., and Coauthors, 2013: Stable Atmospheric Boundary Layers and Diurnal Cycles: Challenges for Weather and Climate Models. *Bull. Amer. Meteor. Soc.*, **94** (11), 1691–1706, doi:10.1175/BAMS-D-11-00187.1.
- Huang, H., and C. Chen, 2016: Climatological aspects of dense fog at Urumqi Diwopu International Airport and its impacts on flight on-time performance. *Nat. Hazards*, **81** (2), 1091–1106, doi:10.1007/s11069-015-2121-z.
- Huang, J., and E. Bou-Zeid, 2013: Turbulence and Vertical Fluxes in the Stable Atmospheric Boundary Layer. part I: A Large-Eddy Simulation Study. *J. Atmos. Sci.*, **70** (6), 1513–1527, doi:10.1175/JAS-D-12-0167.1.
- Hudson, S. R., and R. E. Brandt, 2005: A Look at the Surface-Based Temperature Inversion on the Antarctic Plateau. *J. Climate*, **18** (11), 1673–1696, doi:10.1175/JCLI3360.1.
- Izett, J. G., B. Schilperoord, M. Coenders-Gerrits, P. Baas, F. C. Bosveld, and B. J. H. van de Wiel, 2019: Missed Fog? *Bound.-Layer Meteor.*, **173** (2), 289–309, doi:10.1007/s10546-019-00462-3.
- James, I. N., 1989: The Antarctic drainage flow: implications for hemispheric flow on the Southern Hemisphere. *Antarctic Science*, **1** (3), 279–290, doi:10.1017/S0954102089000404.
- Jiménez, M. A., and J. Cuxart, 2005: Large-Eddy Simulations of the Stable Boundary Layer Using the Standard Kolmogorov Theory: Range of Applicability. *Bound.-Layer Meteor.*, **115** (2), 241–261, doi:10.1007/s10546-004-3470-4.
- King, J. C., and P. S. Anderson, 1994: Heat and water vapour fluxes and scalar roughness lengths over an Antarctic ice shelf. *Bound.-Layer Meteor.*, **69** (1), 101–121, doi:10.1007/BF00713297.
- King, J. C., S. A. Argentini, and P. S. Anderson, 2006: Contrasts between the summertime surface energy balance and boundary layer structure at Dome C and Halley stations, Antarctica. *J. Geophys. Res. Atmos.*, **111** (D2), doi:10.1029/2005JD006130.
- King, J. C., and W. M. Connolley, 1997: Validation of the Surface Energy Balance over the Antarctic Ice Sheets in the U.K. Meteorological Office Unified Climate Model. *J. Climate*, **10** (6), 1273–1287, doi:10.1175/1520-0442(1997)010<1273:VOTSEB>2.0.CO;2.
- King, J. C., W. M. Connolley, and S. H. Derbyshire, 2001: Sensitivity of modelled Antarctic climate to surface and boundary-layer flux parametrizations. *Quart. J. Roy. Meteor. Soc.*, **127** (573), 779–794, doi:10.1002/qj.49712757304.
- Kistner, E., O. Kellner, J. Andresen, D. Todey, and L. W. Morton, 2018: Vulnerability of specialty crops to short-term climatic variability and adaptation strategies in the Midwestern USA. *Climate Change*, **146** (1), 145–158, doi:10.1007/s10584-017-2066-1.

- Kleissl, J., C. Meneveau, and M. B. Parlange, 2003: On the Magnitude and Variability of Subgrid-Scale Eddy-Diffusion Coefficients in the Atmospheric Surface Layer. *J. Atmos. Sci.*, **60** (19), 2372–2388, doi:10.1175/1520-0469(2003)060<2372:OTMAVO>2.0.CO;2.
- Kosović, B., and J. A. Curry, 2000: A Large Eddy Simulation Study of a Quasi-Steady, Stably Stratified Atmospheric Boundary Layer. *J. Atmos. Sci.*, **57** (8), 1052–1068, doi:10.1175/1520-0469(2000)057<1052:ALESSO>2.0.CO;2.
- Kundu, P. K., I. M. Cohen, and D. R. Dowling, 2012: *Fluid Mechanics*. Academic Press, 928 pp.
- Lilly, D. K., 1962: On the numerical simulation of buoyant convection. *Tellus*, **14** (2), 148–172, doi:10.1111/j.2153-3490.1962.tb00128.x.
- Mahrt, L., 1998: Nocturnal Boundary-Layer Regimes. *Bound.-Layer Meteor.*, **88** (2), 255–278, doi:10.1023/A:1001171313493.
- Mahrt, L., 1999: Stratified Atmospheric Boundary Layers. *Bound.-Layer Meteor.*, **90** (3), 375–396, doi:10.1023/A:1001765727956.
- Mahrt, L., 2011: The Near-Calm Stable Boundary Layer. *Bound.-Layer Meteor.*, **140** (3), 343–360, doi:10.1007/s10546-011-9616-2.
- Mahrt, L., 2014: Stably Stratified Atmospheric Boundary Layers. *Annu. Rev. Fluid Mech.*, **46** (1), 23–45, doi:10.1146/annurev-fluid-010313-141354.
- Mahrt, L., and D. Vickers, 2002: Contrasting vertical structures of nocturnal boundary layers. *Bound.-Layer Meteor.*, **105** (2), 351–363, doi:10.1023/A:1019964720989.
- Mahrt, L., and D. Vickers, 2006: Extremely Weak Mixing in Stable Conditions. *Bound.-Layer Meteor.*, **119** (1), 19–39, doi:10.1007/s10546-005-9017-5.
- Mason, P. J., 1989: Large-Eddy Simulation of the Convective Atmospheric Boundary Layer. *J. Atmos. Sci.*, **46** (11), 1492–1516, doi:10.1175/1520-0469(1989)046<1492:LESOTC>2.0.CO;2.
- Mason, P. J., and D. J. Thomson, 1992: Stochastic backscatter in large-eddy simulations of boundary layers. *J. Fluid Mech.*, **242**, 51–78, doi:10.1017/S0022112092002271.
- Matheou, G., 2016: Numerical discretization and subgrid-scale model effects on large-eddy simulations of a stable boundary layer. *Quart. J. Roy. Meteor. Soc.*, **142** (701), 3050–3062, doi:10.1002/qj.2888.
- Matheou, G., and D. Chung, 2014: Large-Eddy Simulation of Stratified Turbulence. Part II: Application of the Stretched-Vortex Model to the Atmospheric Boundary Layer. *J. Atmos. Sci.*, **71** (12), 4439–4460, doi:10.1175/JAS-D-13-0306.1.
- Mauritsen, T., and G. Svensson, 2007: Observations of Stably Stratified Shear-Driven Atmospheric Turbulence at Low and High Richardson Numbers. *J. Atmos. Sci.*, **64** (2), 645–655, doi:10.1175/JAS3856.1.
- McCabe, A., and A. R. Brown, 2007: The role of surface heterogeneity in modelling the stable boundary layer. *Bound.-Layer Meteor.*, **122** (3), 517–534, doi:10.1007/s10546-006-9119-8.
- McNider, R. T., D. E. England, M. J. Friedman, and X. Shi, 1995: Predictability of the Stable Atmospheric Boundary Layer. *J. Atmos. Sci.*, **52** (10), 1602–1614, doi:10.1175/1520-0469(1995)052<1602:POTSAB>2.0.CO;2.
- McNider, R. T., and Coauthors, 2012: Response and sensitivity of the nocturnal boundary layer over land to added longwave radiative forcing. *J. Geophys. Res.*, **117** (D14), doi:10.1029/2012JD017578, d14106.
- Mirocha, J. D., and B. Kosović, 2010: A Large-Eddy Simulation Study of the Influence of Subsidence on the Stably Stratified Atmospheric Boundary Layer. *Bound.-Layer Meteor.*, **134** (1), 1–21, doi:10.1007/s10546-009-9449-4.
- Mirocha, J. D., B. Kosović, and J. A. Curry, 2005: Vertical Heat Transfer in the Lower Atmosphere over the Arctic Ocean During Clear-sky Periods. *Bound.-Layer Meteor.*, **117** (1), 37–71, doi:10.1007/s10546-004-1130-3.
- Moene, A. F., and J. van Dam, 2014: *Transport in the Atmosphere-Vegetation-Soil Continuum*. Cambridge University Press, 446 pp.
- Monahan, A. H., T. Rees, Y. He, and N. McFarlane, 2015: Multiple Regimes of Wind, Stratification, and Turbulence in the Stable Boundary Layer. *J. Atmos. Sci.*, **72** (8), 3178–3198, doi:10.1175/JAS-D-14-0311.1.
- Monin, A. S., 1970: The Atmospheric Boundary Layer. *Annu. Rev. Fluid Mech.*, **2** (1), 225–250, doi:10.1146/annurev.fl.02.010170.001301.

- Na, J. S., E. K. Jin, and J. S. Lee, 2014: Investigation of Kelvin–Helmholtz instability in the stable boundary layer using large eddy simulation. *J. Geophys. Res. Atmos.*, **119**, 7876–7888, doi:10.1002/2013JD021414.
- Nappo, C. J., 1991: Sporadic breakdowns of stability in the PBL over simple and complex terrain. *Bound.-Layer Meteor.*, **54** (1), 69–87, doi:10.1007/BF00119413.
- Newsom, R. K., and R. M. Banta, 2003: Shear-Flow Instability in the Stable Nocturnal Boundary Layer as Observed by Doppler Lidar during CASES-99. *J. Atmos. Sci.*, **60** (1), 16–33, doi:10.1175/1520-0469(2003)060<0016:SFITS>2.0.CO;2.
- Nieuwstadt, F. T. M., 1984: The Turbulent Structure of the Stable, Nocturnal Boundary Layer. *J. Atmos. Sci.*, **41** (14), 2202–2216, doi:10.1175/1520-0469(1984)041<2202:TTSOTS>2.0.CO;2.
- Nieuwstadt, F. T. M., 2005: Direct Numerical Simulation of Stable Channel Flow at Large Stability. *Bound.-Layer Meteor.*, **116** (2), 277–299, doi:10.1007/s10546-004-2818-0.
- Ohya, Y., 2001: Wind-Tunnel Study Of Atmospheric Stable Boundary Layers Over A Rough Surface. *Bound.-Layer Meteor.*, **98** (1), 57–82, doi:10.1023/A:1018767829067.
- Onley, S. P., C. A. Friehe, J. C. Larue, J. A. Businger, E. C. Itsweire, and S. S. Chang, 1996: Surface-Layer Fluxes, Profiles, and Turbulence Measurements over Uniform Terrain under Near-Neutral Conditions. *J. Atmos. Sci.*, **53** (7), 1029–1044, doi:10.1175/1520-0469(1996)053<1029:SLFPAT>2.0.CO;2.
- Petenko, I., S. Argentini, G. Casasanta, C. Genthon, and M. Kallistratova, 2019: Stable Surface-based Turbulent Layer during the Polar Winter at Dome C, Antarctica: Sodar and In-situ Observations. *Bound.-Layer Meteor.*, **171** (1), 101–128, doi:10.1007/s10546-018-0419-6.
- Pietroni, I., S. Argentini, and I. Petenko, 2014: One Year of Surface-Based Temperature Inversions at Dome C, Antarctica. *Bound.-Layer Meteor.*, **150** (1), 131–151, doi:10.1007/s10546-013-9861-7.
- Poulos, G. S., and Coauthors, 2002: CASES-99: A Comprehensive Investigation of the Stable Nocturnal Boundary Layer. *Bull. Amer. Meteor. Soc.*, **83** (4), 555–581, doi:10.1175/1520-0477(2002)083<0555:CACIOT>2.3.CO;2.
- Ricaud, P., and Coauthors, 2015: Review of tropospheric temperature, absolute humidity and integrated water vapour from the HAMSTRAD radiometer installed at Dome C, Antarctica, 2009–14. *Antarctic Sc.*, **27** (6), 598–616, doi:10.1017/S0954102015000334.
- Sandu, I., A. Beljaars, P. Bechtold, T. Mauritsen, and G. Balsamo, 2013: Why is it so difficult to represent stably stratified conditions in numerical weather prediction (NWP) models? *J. Adv. Model. Earth Syst.*, **5** (2), 117–133, doi:10.1002/jame.20013, URL <http://dx.doi.org/10.1002/jame.20013>.
- Schalkwijk, J., H. J. J. Jonker, A. P. Siebesma, and E. van Meijgaard, 2015: Weather Forecasting Using GPU-Based Large-Eddy Simulations. *Bull. Amer. Meteor. Soc.*, **96** (5), 715–723, doi:10.1175/BAMS-D-14-00114.1.
- Shi, X., R. T. McNider, M. P. Singh, D. E. England, M. J. Friedman, W. M. Lapenta, and W. B. Norris, 2005: On the Behavior of the Stable Boundary Layer and the Role of Initial Conditions. *Pure Appl. Geophys.*, **162** (10), 1811–1829, doi:10.1007/s00024-005-2694-7.
- Smagorinsky, J., 1963: General Circulation Experiments with the Primitive Equations. *Mon. Wea. Rev.*, **91** (3), 99–164, doi:10.1175/1520-0493(1963)091<0099:GCEWTP>2.3.CO;2.
- Smedman, A.-S., H. Bergström, and B. Grisogono, 1997: Evolution of stable internal boundary layers over a cold sea. *J. Geophys. Res. Oceans*, **102** (C1), 1091–1099, doi:10.1029/96JC02782.
- Smith, K. L., and L. M. Polvani, 2017: Spatial patterns of recent Antarctic surface temperature trends and the importance of natural variability: lessons from multiple reconstructions and the CMIP5 models. *Climate Dyn.*, **48** (7), 2653–2670, doi:10.1007/s00382-016-3230-4.
- Snyder, R. L., and J. Paulo de Melo-Abreu, 2005: *Frost Protection: fundamentals, practice and economics*, FAO Environment and Natural Resources Service Series, No. 10, Vol. 1. Food and Agriculture Organization of the United Nations, 240 pp.
- Sorbjan, Z., 2010: Gradient-based scales and similarity laws in the stable boundary layer. *Quart. J. Roy. Meteor. Soc.*, **136** (650), 1243–1254, doi:10.1002/qj.638, URL <http://dx.doi.org/10.1002/qj.638>.
- Steenefeld, G. J., B. J. H. van de Wiel, and A. A. M. Holtslag, 2006: Modelling the Arctic Stable Boundary Layer and its Coupling to the Surface. *Bound.-Layer Meteor.*, **118** (2), 357–378, doi:10.1007/s10546-005-7771-z.

- Steenefeld, G. J., M. J. J. Wokke, C. D. Groot Zwaaftink, S. Pijlman, B. G. Heusinkveld, A. F. G. Jacobs, and A. A. M. Holtslag, 2010: Observations of the radiation divergence in the surface layer and its implication for its parameterization in numerical weather prediction models. *J. Geophys. Res. Atmos.*, **115** (D6), doi:10.1029/2009JD013074.
- Stolaki, S., I. Pytharoulis, and T. Karacostas, 2012: A Study of Fog Characteristics Using a Coupled WRF-COBELE Model Over Thessaloniki Airport, Greece. *Pure Appl. Geophys.*, **169** (5), 961–981, doi:10.1007/s00024-011-0393-0.
- Stull, R. B., 1988: *An Introduction to Boundary Layer Meteorology*. Springer Netherlands, 670 pp.
- Sullivan, P. P., J. C. McWilliams, and C.-H. Moeng, 1994: A subgrid-scale model for large-eddy simulation of planetary boundary-layer flows. *Bound.-Layer Meteor.*, **71** (3), 247–276, doi:10.1007/BF00713741.
- Sullivan, P. P., J. C. Weil, E. G. Patton, H. J. J. Jonker, and D. V. Mironov, 2016: Turbulent Winds and Temperature Fronts in Large-Eddy Simulations of the Stable Atmospheric Boundary Layer. *J. Atmos. Sci.*, **73** (4), 1815–1840, doi:10.1175/JAS-D-15-0339.1.
- Sun, J., D. H. Lenschow, M. A. LeMone, and L. Mahrt, 2016: The Role of Large-Coherent-Eddy Transport in the Atmospheric Surface Layer Based on CASES-99 Observations. *Bound.-Layer Meteor.*, **160** (1), 83–111, doi:10.1007/s10546-016-0134-0.
- Sun, J., L. Mahrt, R. M. Banta, and Y. L. Pichugina, 2012: Turbulence Regimes and Turbulence Intermittency in the Stable Boundary Layer during CASES-99. *J. Atmos. Sci.*, **69** (1), 338–351, doi:10.1175/JAS-D-11-082.1.
- Sun, J., and Coauthors, 2004: Atmospheric Disturbances that Generate Intermittent Turbulence in Nocturnal Boundary Layers. *Bound.-Layer Meteor.*, **110** (2), 255–279, doi:10.1023/A:1026097926169.
- Svensson, G., and Coauthors, 2011: Evaluation of the Diurnal Cycle in the Atmospheric Boundary Layer Over Land as Represented by a Variety of Single-Column Models: The Second GABLS Experiment. *Bound.-Layer Meteor.*, **140** (2), 177–206, doi:10.1007/s10546-011-9611-7.
- Thomas, C. K., A. M. Kennedy, J. S. Selker, A. Moretti, M. H. Schroth, A. R. Smoot, N. B. Tuffillaro, and M. J. Zeeman, 2012: High-Resolution Fibre-Optic Temperature Sensing: A New Tool to Study the Two-Dimensional Structure of Atmospheric Surface-Layer Flow. *Bound.-Layer Meteor.*, **142** (2), 177–192, doi:10.1007/s10546-011-9672-7.
- Tijm, A. B. C., A. J. van Delden, and A. A. M. Holtslag, 1999: The Inland Penetration of Sea Breezes. *Contrib. Atmos. Phys.*, **72** (4), 317–328.
- van de Berg, W. J., M. R. van den Broeke, and E. van Meijgaard, 2007: Heat budget of the East Antarctic lower atmosphere derived from a regional atmospheric climate model. *J. Geophys. Res.*, **112** (D23101), doi:10.1029/2007JD008613.
- van de Wiel, B. J. H., A. F. Moene, O. K. Hartogensis, H. A. R. de Bruin, and A. A. M. Holtslag, 2003: Intermittent Turbulence in the Stable Boundary Layer over Land. Part III: A Classification for Observations during CASES-99. *J. Atmos. Sci.*, **60** (20), 2509–2522, doi:10.1175/1520-0469(2003)060<2509:ITITSB>2.0.CO;2.
- van de Wiel, B. J. H., A. F. Moene, and H. J. J. Jonker, 2012a: The Cessation of Continuous Turbulence as Precursor of the Very Stable Nocturnal Boundary Layer. *J. Atmos. Sci.*, **69** (11), 3097–3115, doi:10.1175/JAS-D-12-064.1.
- van de Wiel, B. J. H., A. F. Moene, H. J. J. Jonker, P. Baas, S. Basu, J. M. M. Donda, J. Sun, and A. A. M. Holtslag, 2012b: The Minimum Wind Speed for Sustainable Turbulence in the Nocturnal Boundary Layer. *Bound.-Layer Meteor.*, **69** (11), 3116–3127, doi:10.1175/JAS-D-12-0107.1.
- van de Wiel, B. J. H., A. F. Moene, R. J. Ronda, H. A. R. de Bruin, and A. A. M. Holtslag, 2002a: Intermittent Turbulence and Oscillations in the Stable Boundary Layer over Land. Part II: A System Dynamics Approach. *J. Atmos. Sci.*, **59** (17), 2567–2581, doi:10.1175/1520-0469(2002)059<2567:ITAOIT>2.0.CO;2.
- van de Wiel, B. J. H., R. J. Ronda, A. F. Moene, H. A. R. de Bruin, and A. A. M. Holtslag, 2002b: Intermittent Turbulence and Oscillations in the Stable Boundary Layer over Land. Part I: A Bulk Model. *J. Atmos. Sci.*, **59** (5), 942–958, doi:10.1175/1520-0469(2002)059<0942:ITAOIT>2.0.CO;2.
- van de Wiel, B. J. H., and Coauthors, 2017: Regime transitions in near-surface temperature inversions: a conceptual model. *J. Atmos. Sci.*, **74** (4), 1057–1073, doi:10.1175/JAS-D-16-0180.1.
- van der Linden, S. J. A., P. Baas, J. A. van Hooft, I. G. S. van Hooijdonk, F. C. Bosveld, and B. J. H. van de

- Wiel, 2017: Local Characteristics of the Nocturnal Boundary Layer in Response to External Pressure Forcing. *J. Appl. Meteor. Climatol.*, **56** (11), 3035–3047, doi:10.1175/JAMC-D-17-0011.1.
- van der Linden, S. J. A., and Coauthors, 2019: Large-Eddy Simulations of the Steady Wintertime Antarctic Boundary Layer. *Bound.-Layer Meteor.*, **173** (2), 165–192, doi:10.1007/s10546-019-00461-4.
- van Heerwaarden, C. C., B. J. van Stratum, T. Heus, J. A. Gibbs, E. Fedorovich, and J. P. Mellado, 2017: MicroHH 1.0: a computational fluid dynamics code for direct numerical simulation and large-eddy simulation of atmospheric boundary layer flows. *Geosc. Mod. Dev.*, **10** (8), 3145–3165, doi:10.5194/gmd-10-3145-2017.
- van Hooft, J. A., S. Popinet, C. C. van Heerwaarden, S. J. A. van der Linden, S. R. de Roode, and B. J. H. van de Wiel, 2018: Towards Adaptive Grids for Atmospheric Boundary-Layer Simulations. *Bound.-Layer Meteor.*, **167** (3), 421–443, doi:10.1007/s10546-018-0335-9.
- van Hooijdonk, I. G. S., J. M. M. Donda, H. J. H. Clercx, F. C. Bosveld, and B. J. H. van de Wiel, 2015: Shear Capacity as Prognostic for Nocturnal Boundary Layer Regimes. *J. Atmos. Sci.*, **72** (4), 1518–1532, doi:10.1175/JAS-D-14-0140.1.
- van Ulden, A. P., and A. A. M. Holtslag, 1985: Estimation of Atmospheric Boundary Layer Parameters for Diffusion Applications. *J. Appl. Meteor. Climatol.*, **24** (11), 1196–1207, doi:10.1175/1520-0450(1985)024<1196:EOABLP>2.0.CO;2.
- van Ulden, A. P., and J. Wieringa, 1996: Atmospheric boundary layer research at Cabauw. *Bound.-Layer Meteor.*, **78** (1), 39–69, doi:10.1007/BF00122486.
- Vignon, E., C. Genthon, H. Barral, C. Amory, G. Picard, H. Gallée, G. Casasanta, and S. Argentini, 2017a: Momentum- and Heat-Flux Parametrization at Dome C, Antarctica: A Sensitivity Study. *Bound.-Layer Meteor.*, **162** (2), 341–367, doi:10.1007/s10546-016-0192-3.
- Vignon, E., F. Hourdin, C. Genthon, B. J. H. van de Wiel, H. Gallée, J.-B. Madeleine, and J. Beaumet, 2018: Modeling the Dynamics of the Atmospheric Boundary Layer Over the Antarctic Plateau With a General Circulation Model. *J. Adv. Model Earth Sys.*, **10** (1), 98–125, doi:10.1002/2017MS001184.
- Vignon, E., and Coauthors, 2017b: Stable boundary-layer regimes at Dome C, Antarctica: observation and analysis. *Quart. J. Roy. Meteor. Soc.*, **143** (704), 1241–1253, doi:10.1002/qj.2998.
- Vitasse, Y., and M. Rebetez, 2018: Unprecedented risk of spring frost damage in Switzerland and Germany in 2017. *Climate Change*, **149** (2), 233–246, doi:10.1007/s10584-018-2234-y.
- Viterbo, P., A. Beljaars, J.-F. Mahfouf, and J. Teixeira, 1999: The representation of soil moisture freezing and its impact on the stable boundary layer. *Quart. J. Roy. Meteor. Soc.*, **125** (559), 2401–2426, doi:10.1002/qj.49712555904.
- Whiteman, C. D., T. Haiden, B. Pospichal, S. Eisenbach, and R. Steinacker, 2004: Minimum Temperatures, Diurnal Temperature Ranges, and Temperature Inversions in Limestone Sinkholes of Different Sizes and Shapes. *J. Appl. Meteor. Climatol.*, **43** (8), 1224–1236, doi:10.1175/1520-0450(2004)043<1224:MTDTRA>2.0.CO;2.
- Wyngaard, J. C., 1973: On surface-layer turbulence. *Workshop on Micrometeorology*, D. A. Haugen, Ed., Amer. Meteor. Soc., 101–149.
- Zeeman, M. J., J. S. Selker, and C. K. Thomas, 2015: Near-Surface Motion in the Nocturnal, Stable Boundary Layer Observed with Fibre-Optic Distributed Temperature Sensing. *Bound.-Layer Meteor.*, **154** (2), 189–205, doi:10.1007/s10546-014-9972-9.
- Zhou, B., and F. K. Chow, 2011: Large-Eddy Simulation of the Stable Boundary Layer with Explicit Filtering and Reconstruction Turbulence Modeling. *J. Atmos. Sci.*, **68** (9), 2142–2155, doi:10.1175/2011JAS3693.1.
- Zhou, B., and F. K. Chow, 2014: Nested Large-Eddy Simulations of the Intermittently Turbulent Stable Atmospheric Boundary Layer over Real Terrain. *J. Atmos. Sci.*, **71** (3), 1021–1039, doi:10.1175/JAS-D-13-0168.1.
- Zilitinkevich, S. S., T. Elperin, N. Kleeorin, and I. Rogachevskii, 2007: Energy- and flux-budget (EFB) turbulence closure model for stably stratified flows. Part i: steady-state, homogeneous regimes. *Bound.-Layer Meteor.*, **125** (2), 167–191, doi:10.1007/s10546-007-9189-2.
- Zilitinkevich, S. S., T. Elperin, N. Kleeorin, I. Rogachevskii, I. Esau, T. Mauritsen, and M. W. Miles, 2008: Turbulence energetics in stably stratified geophysical flows: Strong and weak mixing regimes. *Quart. J. Roy. Meteor. Soc.*, **134** (633), 793–799, doi:10.1002/qj.264.

Dankwoord

Hier is het tijd om even stil te staan en terug te kijken op de voorbije vier jaren. Graag wil ik deze pagina daarom gebruiken om iedereen te bedanken die direct of indirect hebben bijgedragen aan de totstandkoming van dit proefschrift.

Allereerst wil ik hier mijn promotoren Bas van de Wiel en Herman Russchenberg en mijn copromoter Peter Baas bedanken voor hun begeleiding. Bas, bedankt voor je tomeloze inzet en haast oneindig enthousiasme de afgelopen vier jaren. Je hebt mij wegwijs gemaakt binnen de grenslaagmeteorologie en mij ook de mogelijkheid gegeven om mijn promotie zelf vorm te geven. Herman, bedankt voor het vertrouwen dat je mij gegeven hebt. Over welk onderwerp de discussie ook ging, je hebt me het belang geleerd van het helder formuleren van korte, bondige argumenten. Peter, gekscherend wordt jij binnen onze groep weleens ‘ons meteorologisch geweten’ genoemd, maar met slechts die term zouden we jou tekort doen. Ik waardeer jouw frisse blik en inzichten. Bedankt daarvoor.

I would also like to express my gratitude to my committee members: Pier Siebesma, Bert Holtslag, Christoph Thomas and Marie-Claire ten Veldhuis, who took the time and effort to read my dissertation and be part of the committee. Also, thank you for the interactions throughout these years. Mijn speciale dank aan Harm Jonker, wiens brede kennis, waardevolle suggesties en enthousiasme hebben bijgedragen aan de laatste twee publicaties. Ook mijn speciale dank aan Chiel van Heerwaarden voor de vele discussies en de hulp bij het gebruiken van de simulatiecode MicroHH. Furthermore, I would like to thank Etienne Vignon, Christophe Genthon, John Edwards, Fred Bosveld and Igor Petenko for the fruitful collaboration that contributed to my publications.

Wetenschap floreert bij het uitwisselen en bediscussiëren van ideeën. Daarom wil ik graag Antoon van Hooft, Jonathan Izett en Ivo van Hooijdonk bedanken voor alle groepsdiscussies. Ook dank voor alle leuke momenten gedurende conferenties en andere uitjes. *I would like to thank all my present and former colleagues in the department of Geoscience and Remote Sensing for providing a nice and inspiring working environment. I am especially grateful for all the coffee breaks, ‘borrels’, and fun trips and activities that provided some much needed relaxation.*

Verder wil ik mijn familie en vrienden bedanken voor alle steun en leuke momenten door al die jaren heen. Als laatste wil ik hier mijn ouders bedanken. Pap en mam, jullie hebben altijd voor mij klaargestaan en mij altijd gesteund. Bedankt!

Curriculum Vitae

- September 26, 1991 Born in Waalwijk, The Netherlands
- 2003–2009 **Gymnasium**
Willem van Oranje College Waalwijk
- 2009–2012 **Bachelor of Science in Applied Physics,**
Eindhoven University of Technology
- 2012–2014 **Master of Science in Applied Physics,**
Eindhoven University of Technology
Specialization: Fluid Dynamics
- Master thesis: “Particle dynamics in boundary layers
below a swirl flow”
- Internship at the Royal Institute of Technology (KTH),
Stockholm, Sweden
- 2015–2019 **Doctoral candidate**
Geoscience and Remote Sensing,
Civil Engineering and Geosciences,
Delft University of Technology

List of Publications

First authored:

- **van der Linden, S.J.A.**, B.J.H. van de Wiel, C.C. van Heerwaarden, I. Petenko, P. Baas, and H.J.J. Jonker, 2019: A Businger Mechanism for Intermittent Bursting in the Stable Boundary Layer. *Submitted to Journal of the Atmospheric Sciences* (Nov 2019)
- **van der Linden, S.J.A.**, J.M. Edwards, C.C. van Heerwaarden, E. Vignon, C. Genthon, I. Petenko, P. Baas, H.J.J. Jonker, and B.J.H. van de Wiel, 2019: Large-Eddy Simulations of the Steady Wintertime Antarctic Boundary Layer. *Boundary-Layer Meteorology*, **173** (2), 165–192, doi:10.1007/s10546-019-00461-4
- **van der Linden, S.J.A.**, P. Baas, J.A. van Hooft, I.G.S. van Hooijdonk, F.C. Bosveld, and B.J.H. van de Wiel, 2017: Local Characteristics of the Nocturnal Boundary Layer in Response to External Pressure Forcing. *Journal of Applied Meteorology and Climatology*, **56** (11), 3035–3047, doi:10.1175/JAMC-D-17-0011.1

Coauthored:

- Baas, P., B.J.H. van de Wiel, E. van Meijgaard, E. Vignon, C. Genthon, **S.J.A. van der Linden**, and S.R. de Roode, 2018: Transitions in the wintertime near-surface temperature inversion at Dome C, Antarctica. *Quarterly Journal of the Royal Meteorological Society*, **145** (720), 930–946, doi:10.1002/qj.3450
- van Hooft, J.A., S. Popinet, C.C. van Heerwaarden, **S.J.A. van der Linden**, S.R. de Roode, and B.J.H. van de Wiel, 2018: Towards Adaptive Grids for Atmospheric Boundary-Layer Simulations. *Boundary-Layer Meteorology*, **167** (3), 421–443, doi:10.1007/s10546-018-0335-9
- Baas, P., B.J.H. van de Wiel, **S.J.A. van der Linden**, and F.C. Bosveld, 2017: From Near-Neutral to Strongly Stratified: Adequately Modelling the Clear-Sky Nocturnal Boundary Layer at Cabauw. *Boundary-Layer Meteorology*, **166** (2), 217–238, doi:10.1007/s10546-017-0304-8
- Vignon, E., B.J.H. van de Wiel, I.G.S. van Hooijdonk, C. Genthon, **S.J.A. van der Linden**, J.A. van Hooft, P. Baas, W. Maurel, O. Traullé, and G. Casasanta, 2017: Stable boundary-layer regimes at Dome C, Antarctica: observation and analysis. *Quarterly Journal of the Royal Meteorological Society*, **143** (704), 1241–1253, doi:10.1002/qj.2998

- van de Wiel, B.J.H., E. Vignon, P. Baas, I.G.S. van Hooijdonk, **S.J.A. van der Linden**, J.A. van Hooft, F.C. Bosveld, S.R. de Roode, A.F. Moene, and C. Genthon, 2017: Regime Transitions in Near-Surface Temperature Inversions: A Conceptual Model. *Journal of the Atmospheric Sciences*, **74** (4), 1057–1073, doi:10.1175/JAS-D-16-0180.1

List of Presentations

Oral presentations

- BBOS Autumn Symposium, October 2019, 's-Hertogenbosch, The Netherlands
- European Meteorological Society Annual Meeting, September 2019, Kongens Lyngby, Denmark
- European Geosciences Union, April 2019, Vienna, Austria
- GABLS4 Workshop, September 2018, Toulouse, France
- 23rd Boundary Layer and Turbulence Symposium, American Meteorological Society, June 2018, Oklahoma City, OK, USA
(Awarded: *Best Oral Presentation Prize*)
- European Meteorological Society Annual Meeting, September 2017, Dublin, Ireland
- BBOS Autumn Symposium, October 2016, Heerenveen, The Netherlands

Poster presentations

- European Geosciences Union, April 2017, Vienna, Austria
- 3rd Decennial Workshop on Turbulence in Stably Stratified Planetary Boundary Layers, March 2017, Delft, The Netherlands
- 22nd Boundary Layer and Turbulence Symposium, American Meteorological Society, June 2016, Salt Lake City, UT, USA

